Lawrence Berkeley National Laboratory
LBL Publications

Title
DECOVALEX-2023 Task A Final Report

Permalink
https://escholarship.org/uc/item/03m200gt

Authors
Faybishenko, Boris
Plua, Carlos

Publication Date
2024-11-29

Copyright Information
This work is made available under the terms of a Creative Commons Attribution License, available at https://creativecommons.org/licenses/by/4.0/

Peer reviewed

eScholarship.org Powered by the California Digital Library
University of California

DECOVALEX-2023
Task A Final Report

C. Plúa

With contributions from:

M.N. Vu, R. de La Vaissière, G. Armand, S. Olivella, A. Rodriguez-Dono, Z. Ouraga, Z. Yu, J.F. Shao, Q. Wang, E. Radeisen, H. Shao, T. Sasaki, S. Yoon, J. Rutqvist, F. Song, S. Collico, A. Gens, L. Bruffell, K. Thatcher, A.E. Bond

December 2023

Disclaimer

This document was prepared as an account of the international research project DECOVALEX-2023 comprising participants from industry, government and academia, with funding organizations--Andra, BASE, BGE, BGR, CAS, CNSC, COVRA, U.S. DOE, Enresa, ENSI, JAEA, KAERI, NWMO, NWS, SÚRAO, SSM and Taipower. The statements made in the report are, however, solely those of the authors and do not necessarily reflect those of the Funding Organizations. While this document is believed to contain correct information, neither the United States Government nor any agency thereof, nor the Regents of the University of California, nor any of their employees, makes any warranty, express or implied, or assumes any legal responsibility for the accuracy, completeness, or usefulness of any information, apparatus, product, or process disclosed, or represents that its use would not infringe privately owned rights. Reference herein to any specific commercial product, process, or service by its trade name, trademark, manufacturer, or otherwise does not necessarily constitute or imply its endorsement, recommendation, or favoring by the United States Government or any agency thereof or the Regents of the University of California. The views and opinions of the authors expressed herein do not necessarily state or reflect those of the United States Government, any agency thereof, or the Regents of the University of California.

This technical document does not consider contractual limitations or obligations under the Standard Contract for Disposal of Spent Nuclear Fuel and/or High-Level Radioactive Waste (Standard Contract) (10 CFR Part 961).

To the extent discussions or recommendations in this document conflict with the provisions of the Standard Contract, the Standard Contract governs the obligations of the parties, and this presentation in no manner supersedes, overrides, or amends the Standard Contract.

No inferences should be drawn from this document regarding future actions by DOE, which are limited by the terms of the Standard Contract and Congressional appropriations for the Department to fulfill its obligations under the Nuclear Waste Policy Act, including licensing and constructing a spent nuclear fuel repository.

Copyright

This publication has been composed under the direction of editors at Lawrence Berkeley National Laboratory under Contract No. DE-AC02-05CH11231 with the U.S. Department of Energy, Quintessa Limited, Birchwood Park, Warrington WA3 6GA, UK. The U.S. Government retains a non-exclusive, irrevocable, worldwide license to publish or reproduce this published report or allow others to do so for U.S. Government purposes.

Writers for each chapter are responsible for copyright permissions (if applicable) for graphics within their chapter.

DECOVALEX-2023

Task A Final Report

Main Authors :

Carlos Plúa
Andra

Contributing Authors (alphabetical by organisation) :

Minh-Ngoc Vu, Rémi de La Vaissière, G. Armand
Andra

Sebastià Olivella, Alfonso Rodriguez Dono
Andra/CIMNE-UPC

Zady Ouraga
Andra/Ineris

Zhan Yu, Jian-Fu Shao
Andra/Lamcube

Qianyun Wang, Eike Radeisen, Hua Shao
BGR/UFZ

Tsubasa, Sasaki, Sangcheol Yoon, Jonny Rutqvist
DOE/LBNL

Fei Song, Stefano Collico, Antonio Gens
Enresa/CIMNE-UPC

Kate Thatcher, Louise Bruffell, Alexander E. Bond
NWS/Quintessa

Reviewed by AE Bond

Published 29/11/2024

LBNL-2001621

Preface

The DECOVALEX Project is an ongoing international research collaboration established in 1992 to advance the understanding and modeling of coupled Thermal (T), Hydrological (H), Mechanical (M), and Chemical (C) processes in geological systems. DECOVALEX was initially motivated by recognising that predicting these coupled effects is essential to the performance and safety assessment of geologic disposal systems for radioactive waste and spent nuclear fuel. Later, it was realized that these processes also play a critical role in other subsurface engineering activities, such as subsurface CO_2 storage, enhanced geothermal systems, and unconventional oil and gas production through hydraulic fracturing. Research teams from many countries (e.g., Canada, China, Czech Republic, Finland, France, Germany, Japan, Netherlands, Republic of Korea, Spain, Sweden, Switzerland, Taiwan, United Kingdom, and the United States) various institutions have participated in the DECOVALEX Project over the years, providing a wide range of perspectives and solutions to these complex problems. These institutions represent radioactive waste management organizations, national research institutes, regulatory agencies, universities, and industry and consulting groups.

At the core of the collaborative work within DECOVALEX is the collaborative analysis and comparative modeling of state-of-the-art field and laboratory experiments. DECOVALEX engages model comparison in a broad and comprehensive sense, including the modelers' interpretation of experimental data, selection of boundary conditions, rock and fluid properties, etc., and their choice of coupling schemes and simulators. This recent phase of DECOVALEX has expanded the work scope to include the modelers being challenged to gain an understanding of the representation coupled processes in generic 'whole system' or 'performance assessment' models. In-depth and detailed discussions among the teams yield insight into the coupled THMC processes and stimulate the development of modeling capabilities and measurement methods. This would have been impossible if only one or two groups had studied the data.

Since the project initiation, DECOVALEX has been organized in several four-year phases, each featuring several modeling tasks of importance to radioactive waste disposal and other geoscience applications. Seven project phases were successfully concluded between 1992 and 2019, the results of which have been summarized in several overview publications (e.g., Tsang et al., 2009; Birkholzer et al., 2018; Birkholzer et al., 2019, Birkholzer et al., 2024). The most recent phase, DECOVALEX-2023, started in 2020 and ended in 2023. Seven tasks were conducted in DECOVALEX-2023, as follows:

- **Task A: HGFrac** – Thermal- and gas- induced fracturing of the Callovo-Oxfordian Clay, France
- **Task B: MAGIC** – Migration of gas in compacted clay

- **Task C: FE Experiment** – Thermal-hydro-mechanical (THM) modelling of the FE experiment at Mont Terri, Switzerland
- **Task D: Horonobe EBS Experiment** - THM modelling of the Horonobe EBS experiment at the Horonobe URL, Japan
- **Task E: BATS** – THM modeling for the Brine Availability Test in Salt (BATS) at the WIPP, New Mexico, USA
- **Task F: Performance Assessment** – Comparative generic performance assessment models in crystalline and salt formations
- **Task G: SAFENET** – Laboratory-scale TH and THM analyses of single fractures

The DECOVALEX Project would not have been possible without the support and engagement of the participating organizations who jointly support the coordination of the project within a given project phase, propose and coordinate modeling tasks, including the necessary experimental data, and deploy their research team (or teams) working on a selection of the tasks conducted in the project. The partner organizations in DECOVALEX-2023 were:

- Andra, National Radioactive Waste Management Agency, *France*
- BASE, Federal Office for the Safety of Nuclear Waste Management*, Germany*
- BGE, Federal Company for Radioactive Waste Disposal, *Germany*
- BGR, Federal Institute for Geosciences and Natural Resources, *Germany*
- CAS, Chinese Academy of Sciences, *China*
- CNSC, Canadian Nuclear Safety Commission, *Canada*
- COVRA, Central Organisation for Radioactive Waste, *Netherlands*
- DOE, Department of Energy, *USA*
- Enresa, National Radioactive Waste Management Agency, *Spain*
- ENSI, Swiss Federal Nuclear Safety Inspectorate, *Switzerland*
- JAEA, Japan Atomic Energy Agency, *Japan*
- KAERI, Korea Atomic Energy Research Institute, Republic of Korea
- NWMO, Nuclear Waste Management Organization, *Canada*
- NWS, Nuclear Waste Services, *United Kingdom*
- SSM, Swedish Radiation Safety Authority, *Sweden*
- SÚRAO, Radioactive Waste Repository Authority, *Czech Republic*
- Taipower, Taiwan Power Company, *Taiwan*

We are extremely grateful to these organizations for their financial and technical support of DECOVALEX-2019.

Jens Birkholzer (Chairman of the DECOVALEX project) and Alex Bond (Technical Coordinator of the DECOVALEX Project).

Berkeley, California, USA, October 2024

References:

Birkholzer, J.T., Bond, A.E., Hudson, J.A., Jing, L., Tsang, C.-F., Shao, H., Kolditz, O. (2018): DECOVALEX-2015 - An International Collaboration for Advancing the Understanding and Modeling of Coupled Thermo-Hydro-Mechanical-Chemical (THMC) Processes in Geological Systems, Environmental Earth Sciences, 77(14). https://doi.org/10.1016/j.ijrmms.2022.105097

Birkholzer, J.T., Tsang, C.-F., Bond, A.E., Hudson, J.A., Jing, L., and Stephansson, O. (2019): 25 Years of DECOVALEX - Scientific Advances and Lessons Learned from an International Research Collaboration in Coupled Subsurface Processes, Invited Review, International Journal and Rock Mechanics and Mining Sciences, 122. https://doi.org/10.1016/j.ijrmms.2019.03.015

Birkholzer, J.T., Bond, A.E. and Tsang, C.-F. (2024). The DECOVALEX international collaboration on modeling of coupled subsurface processes and its contribution to confidence building in radioactive waste disposal. Hydrogeology Journal, https://doi.org/10.1007/s10040-024-02799-7

Tsang, C.-F., Stephansson, O., Jing, L., and Kautsky, F. (2009): DECOVALEX Project: from 1992 to 2007. Environmental Geology, 57(6). https://doi.org/10.1007/s00254-008-1625-1

Summary

Task A, also known as HGFrac, examines the fracturing processes that may occur in the Callovo-Oxfordian claystone (COx) in the context of the high-level (HLW) and intermediate-level long-lived (ILW-LL) radioactive waste repository in France. Understanding these processes and improving numerical models to reproduce them will aid in the design, optimization, and safety of the repository.

Heat and gas fracturing are studied in two independent subtasks following a stepwise approach: laboratory tests/benchmark exercises, in-situ experiment, and finally, an application case. The in-situ heater experiment aimed to thermally induce a hydraulic fracture; temperature and pore pressure were monitored to detect any evidence of fracturing. The in-situ gas injection experiment aimed to study the effect of the stress orientation and gas injection kinetics on the gas fracturing process. The occurrence of fracturing was monitored by gas pressure measured in the injection interval. In both experiments, the excavation-induced fracture network around the heater/injection boreholes played an important role in the reduction of the compressive stress state, leading to both a tensile and shear failure response of the COx.

During the first two years of the project, the research teams working on each task developed and/or proposed numerical approaches for reproducing the occurrence of fracturing in the in-situ experiments. The failure criteria were defined by reproducing the measurements from laboratory extension tests for the heat fracturing subtask. In the gas fracturing subtask, their approaches were used for simulating several benchmark exercises, and an inter-comparison between models was carried out. In both tasks, the developed approaches were compared with a simplified approach considering poro-elasticity for the mechanical behaviour of the COx.

Most of the developed approaches are based on a continuous medium that takes into account variations in hydraulic properties due to mechanical degradation, such as plastic deformation or damage. Other approaches implicitly modelled weak planes or embedded discontinuities to reproduce fracture propagation. The potential for fracture initiation was also studied through of a discrete approach.

In the second half of the project, the research teams mainly focused on interpretative modelling of two in-situ experiments and a blind prediction exercise to test their respective approaches. The models developed by the research teams were also applied at the repository scale to evaluate fracture initiation in a case study under

unfavourable conditions, particularly in terms of spacing between High-Level Waste cells.

The results showed that the poro-elasticity approach could be an efficient tool for understanding the main processes occurring in the COx. One example is the explicit representation of the excavation-induced fracture network around the boreholes, which yielded acceptable results compared to the measurement data. However, advanced approaches were needed to evaluate the potential increase of the excavation-induced fracture network extend and better understand fracture initiation.

The stress analyses carried out by the teams revealed that hydraulic boundary conditions had a strong impact on fracture initiation in the heater experiment. Furthermore, in most cases, the results required higher pore pressure increments to reach fracturing than those measured in the experiment. This implies that the measurements may have been biased by the packer's capacity to fully isolate the piezometric chambers, leading to lower pressures. On the contrary, there was no agreement on the fracturing mode, as some reported either shear or tensile fracturing, while others reported a combination of the two modes.

In the case of gas fracturing, the research teams were limited to the comparison of a single point, which complicated their task. Nonetheless, the numerical results were able to reproduce the measurements and capture processes such as longitudinal gas flow through the excavation-induced fracture network, as suggested by some evidence in the observation piezometric chambers. The numerical models also agreed with the measurements in the sense of higher probability of developing along the injection borehole than radially towards the sound rock.

The approaches developed by the research teams showed that they are capable of analysing and reproducing fracture initiation in the COx. However, areas of future work should focus on the fracture propagation and fracture aperture, which were out of the scope of this task. To this end, additional data must be gathered for the parameter characterisation and validation of the numerical models. Nonetheless, various approaches showed promising results as they were able to reproduce fracture development under certain conditions.

Contents

1 Introduction

The current concept for a deep geological repository for intermediate-level long-lived waste (ILW-LL) and high-level radioactive waste (HLW) in France, known as Cigéo, is based on the emplacement of exothermic waste packages in two main zones: drifts approximately 10 m in diameter for ILW-LL and micro-tunnels about 0.8 m for HLW. Cigéo is planned to be constructed in a deep Callovo-Oxfordian claystone (COx) formation, which exhibits favorable confining conditions for a repository of radioactive waste (Delay et al., 2007).

The French National Radioactive Waste Management Agency (Andra), as the responsible organization for the development of Cigéo, has carried out a research program consisting of laboratory experiments, in-situ tests at the Meuse/Haute-Marne Underground Research Laboratory (MHM URL), and model development and numerical modelling. This research program aims to demonstrate the feasibility of constructing and operating a repository in the COx formation (Armand et al., 2017; Bumbieler et al., 2021).

The heat released from the HLW packages results in a temperature increment within the host formation and its surrounding layers. In a water-saturated porous medium with low permeability, such as the COx, this temperature increment causes a pore pressure build-up primarily due to the difference between the thermal expansion coefficient of the pore water and the solid skeleton (water expanding proportionally more than the COx solids), resulting in less compressive effective stresses. The design of the HLW repository zone for Cigéo aims to ensure that there is no additional diffuse fracture or damage in the far field (i.e., at some diameters from the disposal micro-tunnels) due to transient thermo-hydromechanical (THM) loading.

Understanding the migration of gas produced by corrosion of metals, microbial degradation, and radiolysis of water within the host rock is also crucial for assessing the long-term safety performance of the repository. If the rate of gas production exceeds the rate of diffusion of dissolved gas in the pore water of the host rock and the engineered barriers, the pressure build-up related to the gas phase may overcome the entry gas pressure and the capillary resistance of the surrounding rock. This could lead to damage in the rock mass and potentially impact the safety performance of the COx formation. The evacuation capacity of the gas through the processes described above and the kinetics of the gas pressure rise control both the creation of tensile fractures and their extension.

DECOVALEX-2023 Task A addresses both areas related to fluid pressurization within the COx and its resulting fracturing. Based on in-situ experiments at the MHM URL, the understanding of fundamental processes and the improvement of capabilities of numerical models will be enhanced, contributing to the design and optimization of the repository. It will also contribute to a robustness demonstration that these processes are not expected to occur at the repository scale.

The task is divided into two subtasks using appropriate formulations for each subject: (Step A1 – Heat fracturing) THM behaviour and (Step A2 - Gas fracturing) isothermal two-phase flow behaviour in the COx. Both subtasks have a similar structure and are undertaken in parallel: (Ax.1) definition of conceptual models, (Ax.2) numerical reproduction of an in-situ experiment and (Ax.3) application at the repository scale. The Step Ax.2 consists of a blind prediction and an interpretative analysis of different phases of the in-situ experiments. Subtask A1 can be considered a continuation of DECOVALEX-2019 TASK E, in which the THM response of the COx due to thermal loading was investigated at different scales (Plúa et al., 2021; Seyedi et al., 2021).

This report introduces the in-situ experiments used in steps Ax.2 and summarizes the work performed by the research teams in Task A. Six and three teams are respectively involved in subtasks A1 and A2. Table 1 lists the research teams with their respective numerical codes, and the symbol ☒ is assigned to the subject on which they are working.

Table 1. Research teams participating in Task A.

Acronym of the team	Team	Funding organization	Numerical code	A1	A2
CIMNE-UPC	Polytechnic University of Catalonia	French National Radioactive Waste Management Agency (Andra)	CODE_BRIGHT		☒
Ineris	French National Institute for Industrial Environment and Risks		UDEC/3DEC	☒	
Lamcube	Laboratory of Mechanics, Multiphysics, Multiscale		In-house Matlab code	☒	☒
BGR/UFZ	Federal Institute for Geosciences and Natural	Federal Institute for Geosciences and Natural Resources	OpenGeoSys (OGS) V5.8	☒	

Acronym of the team	Team	Funding organization	Numerical code	A1	A2
	Resources/Helmholtz-Centre for Environmental Research	(BGR)	OpenGeoSys (OGS) V6.4		☒
LBNL	Lawrence Berkeley National Laboratory	Department Of Energy (DOE)	TOUGH-FLAC	☒	
CIMNE-UPC	International Centre for Numerical Methods in Engineering / Polytechnic University of Catalonia	Spanish National Company for Radioactive Waste (Enresa)	CODE_BRIGHT	☒	
Quintessa	Quintessa Ltd / University of Edinburgh	Nuclear Waste Services (NWS)	COMSOL Multiphysics®	☒	

2 In-situ fracturing experiments conducted in the Callovo-Oxfordian Claystone

2.1 Excavation-induced fracture network

The main level of the MHM URL hosts two in-situ experiments utilized in Task A for the numerical reproduction of fracturing process in the COx (Figure 1): the PGZ and CRQ experiments. The main level of the MHM URL comprises of a drift network at a depth of 490 m. Most of the drifts, are oriented parallel to the horizontal principal stress directions, with the major principal stress approximately $\sigma_{\mathrm{H}} \approx 16$ MPa, and the minor and intermediate principal stresses are similar in magnitude, and about $\sigma_{\mathrm{h}} \approx \sigma_{\mathrm{v}} \approx 12$. MPa (Wileveau et al., 2007).

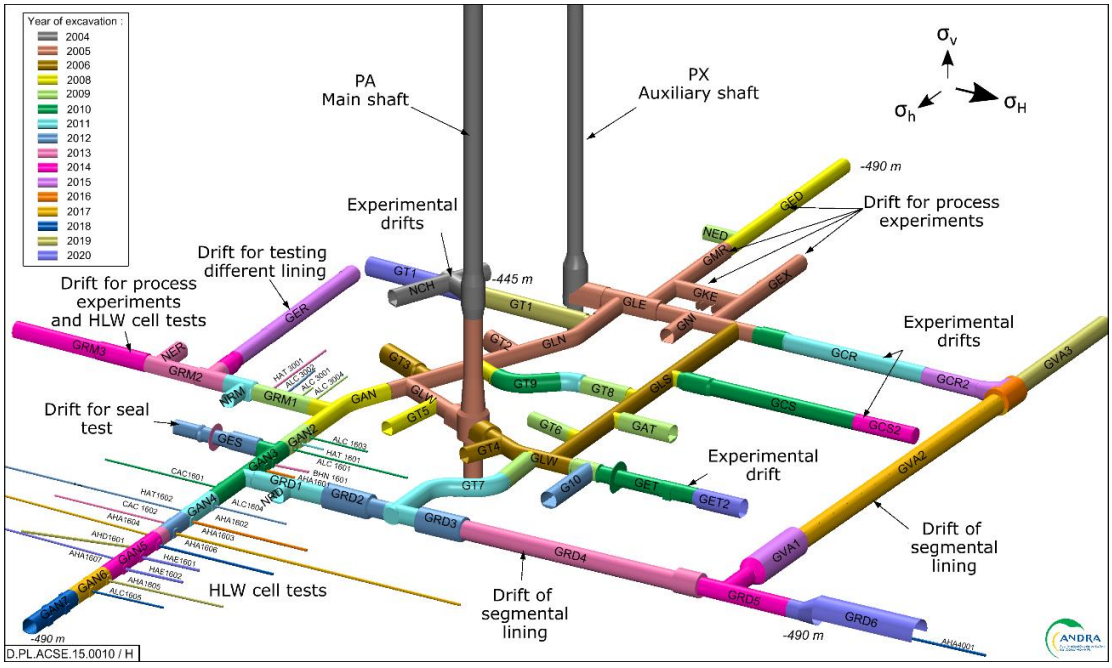

Figure 1. The Meuse/Haute-Marne Underground Research laboratory.

The structural analysis of the drifts' front face and walls, analysis of cores, and permeability measurements have allowed for the characterization of the pattern and extent of the induced fracture networks around drifts at the main level of the MHM URL. The analyses obtained from these data show that the fracture pattern and extension depend on the drift orientation with respect to the in-situ stress field (Figure 2). The fracture extension is as follows (Armand et al., 2014): (a) more developed in the vertical direction of the drift cross-section excavated in the direction of σ_{h} and (b)

larger in the horizontal direction of the drift cross-section excavated in the direction of σ_H.

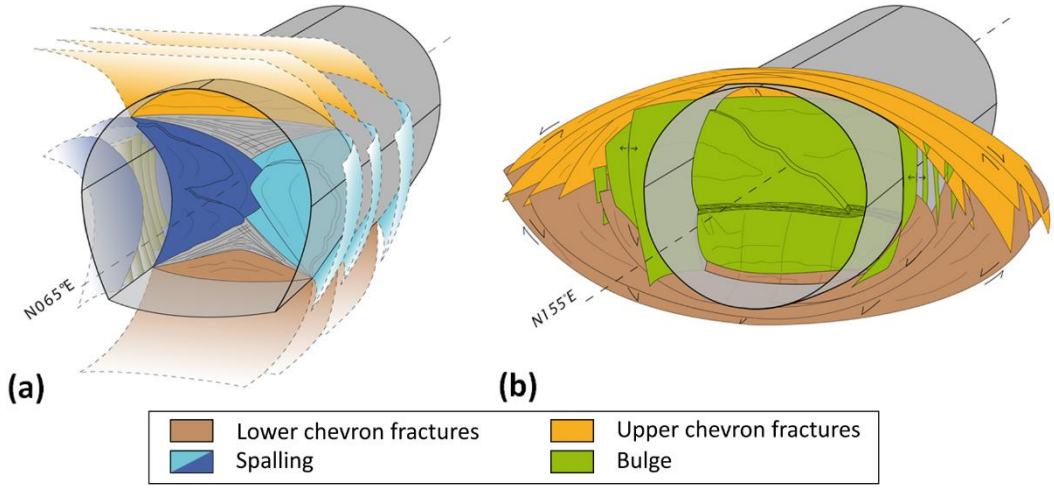

Figure 2. Conceptual model of the induced fracture networks around drifts parallel to: (a) the minor principal stress and (b) the major principal stress (from Armand et al., 2014).

Regardless of the drift orientation, two zones can be identified in the excavation-induced fracture network: a connected fracture zone (ZFC) with a distribution of extensional and shear fractures connected to some degree with the drift, and a discrete fracture zone (ZFD) with only shear fractures that are not physically connected with each other.

These observations also apply to smaller scales (i.e., boreholes and micro-tunnels), suggesting that scale effects, in terms of diameter, are negligible from a bolt borehole (~5 cm) to a drift approximately 9 m in diameter (Armand et al., 2014).

2.2 In-situ heater tests – CRQ

2.2.1 Objectives and description

The objective of the CRQ experiment is to analyze the conditions under which thermal hydrofracturing can occur in the COx, study the influence of fracture occurrence on pore pressure evolution, and characterize the variations in the THM properties in the fractured area (Plúa et al., 2023). To achieve this, the temperature increase in the COx must induce a sufficiently high pore pressure level to generate effective stresses larger than the effective tensile strength, assuming tensile failure is the dominant failure mode.

The CRQ experiment is not a scale model of an HLW repository as designed for Cigéo, although it aims at reproducing a similar stress path followed at the mid-distance between HLW cells and continue heating until the effective tensile strength of the COx is reached.

The experimental set-up consisted of ten 20 m long heater boreholes (CRQ1701-CRQ1710), drilled horizontally from the GCS drift wall. CRQ1709 and CRQ1710 were approximately 0.80 vertical meters apart from each other and surrounded by the other eight heater boreholes. Heater devices were installed in each borehole in the last 10 m. At the mid-plane of the heater devices (i.e., 15 m from the CGS drift wall), the peripheral boreholes were arranged in a square of 3 m. Given the heating design and the in-situ stress field at the MHM URL level, the fracture location was expected to be between the two central boreholes and nearly horizontal. The layout of the experiment is presented in Figure 3.

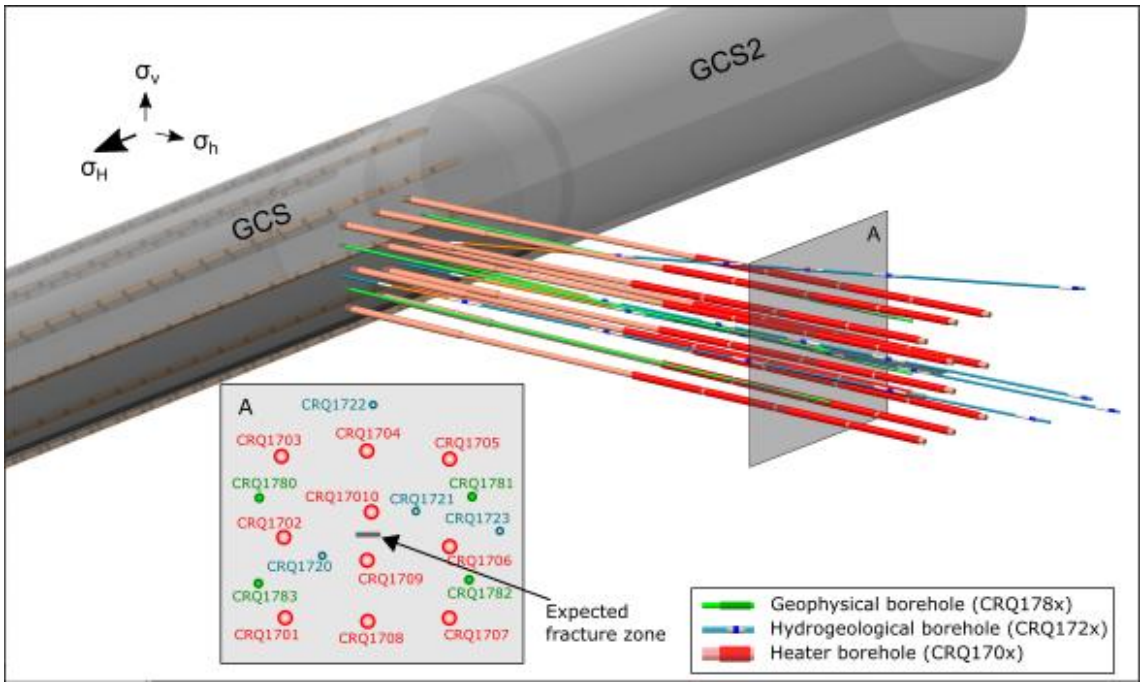

Figure 3. Layout of the CRQ experiment and cross-section at the mid-plane of the heaters (i.e., 15 m from the CGS drift wall).

The heater boreholes have a diameter of 172 mm, except for the first 4 m with an excavated diameter of 220 mm. These boreholes are equipped with a steel casing 140 mm in outer diameter and 10 mm thick; the type of steel is API 5CT grade N80. The temperature along each casing was monitored by 36 sensors installed in contact with the inner casing surface.

To limit drainage around the heater boreholes, the annular space between the casing and the borehole wall was backfilled with a low viscosity resin along the last 16 m. Two

packers separated with resin were placed in the head part to isolate the annular sealing.

Each heater is 10 m long, with a diameter of 101.6 mm, and can be regulated in terms of power or temperature.

The hydrogeological boreholes CRQ1720-CRQ1723, with a diameter of 76 mm, were equipped with five piezometer chambers, each associated with temperature sensors, and were only backfilled with resin in the first 8 meters.

The geophysical boreholes CRQ1780-CRQ1783, with a diameter of 86 mm, were equipped with 16 acoustic emissions (AEs) sensors and 32 seismic velocity sensors. These boreholes were backfilled with a cement–bentonite grout formulation. These sensors were not able to measure any AEs since they were relatively far from the heated zone, and the ambient noise level was too high.

2.2.2 Experimental results

The experiment consisted of two heating phases separated by a cooling phase of about 5 months, as shown by the heat power history in Figure 4. The first cycle started on June 3rd, 2019, and lasted for two months without evidence of fracturing. The second cycle started on January 13th, 2020, lasting just over one month. A fracture event was detected, recorded by a pore pressure breakdown in two chambers located in the heated zone. Three days later, the experiment was halted.

The heater in CRQ1704 was damaged during the cooling phase; consequently, the second heating phase was heated by the remaining 9 heater devices. The maximum temperature was measured at the mid-plane of the heated zone (i.e., 15 m deep): 81.9 °C in the first cycle and 97.4 °C in the second cycle.

Regarding pore pressures, the heating induced slight perturbations in the chambers of CRQ1720, increasing from 14.0 MPa to 16.3 MPa. However, these perturbations were not significant enough to have caused fracturing. During the cooling phase, the pore pressures dropped below the atmospheric pressure (the sensors cannot measure negative pressures), indicating an unsaturated zone estimated to be between 15 m and 18 m deep. This unsaturated zone is generated by different cooling-induced contraction rates of solid and water phases, potentially resulting in negative pore pressures. Due to this under-pressure, the pore pressure took some time to increase during the second cycle until a pore pressure breakdown was observed in CRQ1720. It is worth mentioning that the heating was not stopped until three days after the

occurrence of this event to verify that the multi-packer system was not damaged (Figure 5). The dismantling of the experiment revealed the presence of an isolated shear fracture in cores extracted at 16.5 m from the drift wall. This suggests that the failure mode was not tensile, as originally expected, but rather shearing. Furthermore, the geological structures of the cores extracted near CRQ1709 provided evidence of an enlargement of its excavation-induced fracture network due to the thermal loading.

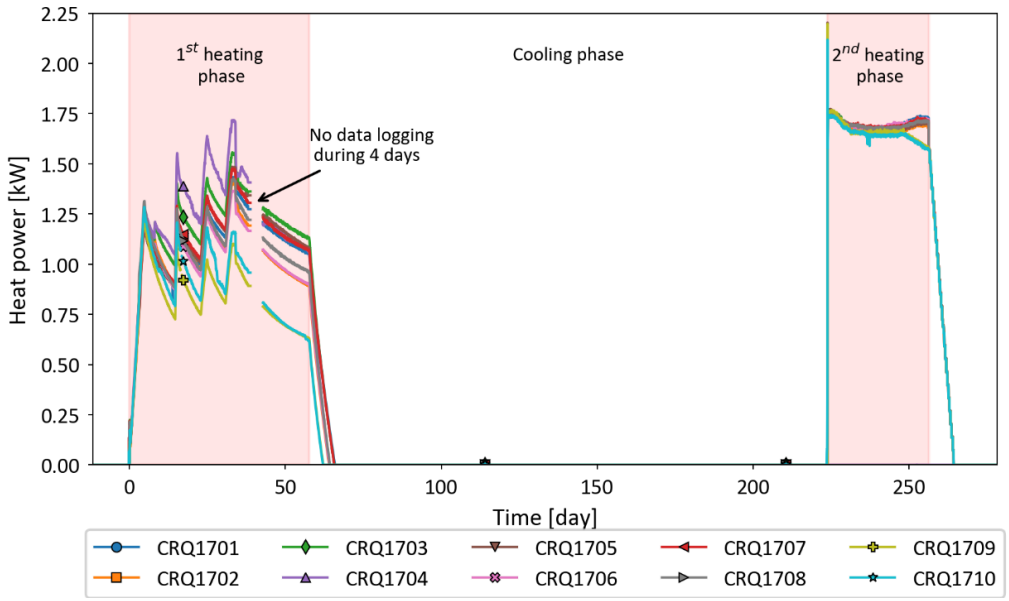

Figure 4. Heat power history of the CRQ experiment.

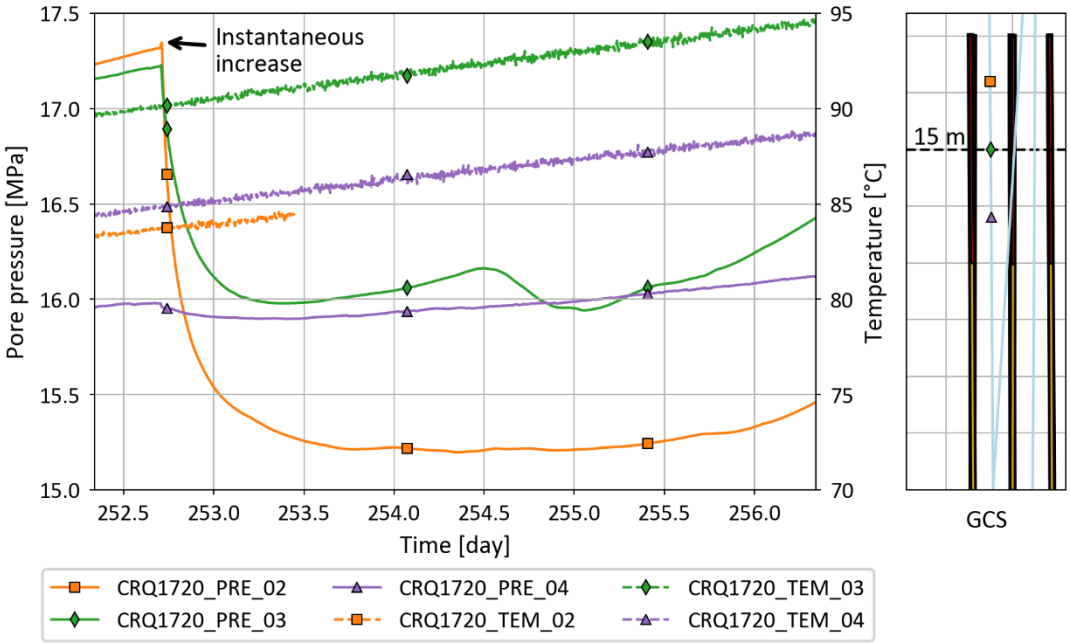

Figure 5. Detail on the evolution of the pore pressure and temperature during the breakdown pore pressure event during the second heating phase.

2.3 In-situ gas injection tests – PGZ3

2.3.1 Objectives and description

The PGZ experiment at the MHM URL is dedicated to studying gas percolation in both the rock and seals. The first phase was carried out between 2009 and 2017 (de La Vaissière et al., 2014). It was demonstrated that a gas pressure of approximately 9.1 MPa did not initiate fracture, and the classical two-phase flow model adequately described these observations. Furthermore, analyses of the measurements indicated that the pressures required to initiate gas fracturing depends on the gas injection rate (de La Vaissière et al., 2020, 2019). These tests highlighted the role of the borehole damaged zone (BDZ) around the interval (shape and size) and emphasized the importance of the pressure increase kinetics concerning gas penetration into the BDZ.

More recently, several boreholes have been drilled to conduct new gas injection tests, aiming to better characterize the gas fracturing process in the COx. The objectives of these new boreholes are to study the effect of the stress orientation and gas injection kinetics on the gas fracturing process.

The boreholes of this on-going phase are all identical in length and equipped with a multiple packer system to monitor water/gas pressure in five isolated intervals. Resin is used to fill the borehole annulus between intervals, ensuring long-term stability and a system with very low compressibility. The boreholes are approximately 35 m long and oriented sub-horizontally. The packers and the intervals have lengths of 1.5 m and 1.0 m, respectively; except for the interval 01, which has a length of 20 cm. Each interval consists of a borehole annulus, a porous cylindrical sinter (30% porosity), and a technological void connected to two hydraulic lines.

The injection tests on boreholes PGZ1002 and PGZ1003, both with a diameter of 76 mm, were used for the interpretative modelling and the blind prediction of Step A2. PGZ1002 was oriented parallel to the minor horizontal stress, while PGZ1003 was oriented parallel to the major horizontal stress (Figure 6).

For each borehole, two intervals were selected to perform a “fast” gas injection test (Interval 04). The fast gas injection protocol consisted of several phases of gas injection at a constant flow rate (~ 500 mLn/min[1]), separated by pressure recovery phases. The first injection phase aimed to create a fracture, while the subsequent phases aimed to

[1] Volume flow units in milliliter normal per minute with reference conditions: temperature of 0°C and pressure of 1 atm (1 mLn ≈ $2.2 \cdot 10^{-8}$ kg/s).

re-open the fracture and to identify the fracture closure pressure, and, if possible, to deduce its orientation.

The packer pressure for all the intervals was also recorded and adjusted according to the type of injection test.

After completing the gas injection sequences, the intervals were resaturated, and water permeability tests were conducted.

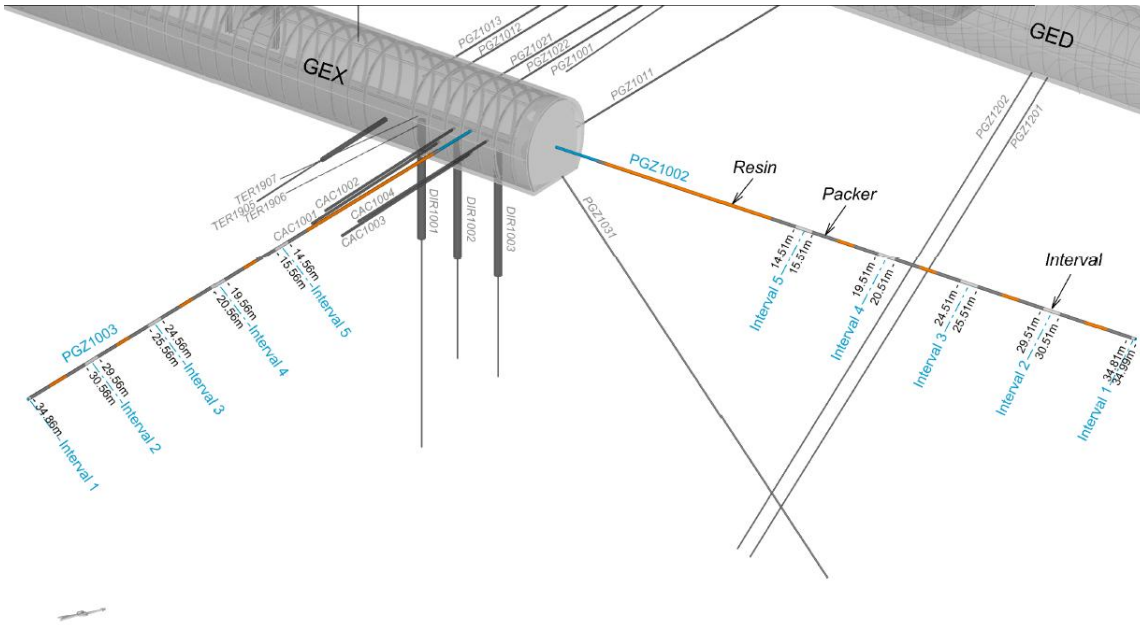

Figure 6. Layout of the PGZ3 experiment: boreholes PGZ1002 and PGZ1003.

2.3.2 Experimental results

In June 2020, a water permeability testing campaign was conducted in the 10 intervals of PGZ1002 and PGZ1003 boreholes. The average hydraulic conductivity value was approximately $4 \cdot 10^{-13}$ m/s.

The test intervals (04) were saturated with water at pore pressures of 5.16 MPa and 4.88 MPa for PGZ1002 and PGZ1003 boreholes, respectively. Prior to the gas injection tests, water was removed from each of these intervals. This was achieved by applying slight gas overpressure to on one of the two hydraulic lines, while the second was opened to recover the water. The extracted water masses were: 472 g for PGZ1002_04 and 334 g for PGZ1003_04.

To assess these extracted water masses, two hypotheses were considered: with and without considering borehole creep. The former assumes full contact (or full convergence) with the tubing, while the latter considers an annular space between the

borehole wall and the tubing. Then, the initial degree of gas saturation in the interval is calculated. Table 2 shows that in all cases, residual water remained in the test interval, likely pushed back into the rock during gas injection. The gas pressure was then kept constant in the interval at hydrostatic pressure until the fast injection tests started.

Table 2. Initial gas saturation of PGZ1002 and PGZ1003 interval #04.

Hypothesis	Degree of gas saturation (%)	
	PGZ1002_04	PGZ1003_04
Full convergence of borehole wall	91	63
Without any convergence of borehole wall	40	28

In December 2020, the first series of fast gas injection tests was performed in the interval 04 of PGZ1002 and PGZ1003 boreholes. Figure 7 shows the gas pressure evolution in the intervals of PGZ1003.

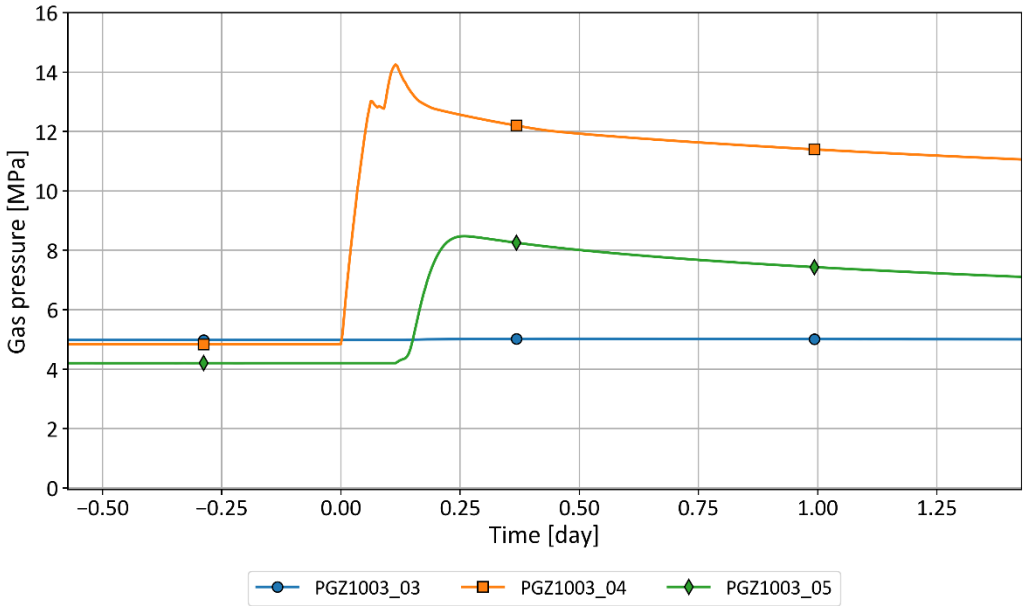

Figure 7. Gas pressure evolution during fast injection test performed in PGZ1003.

The injection flow rate was closed to 500 mLn/min for both tests. Before starting the gas injection tests, the packer pressure adjacent to intervals was increased to about 14 MPa. For the test in PGZ1003, the packer pressure included two steps since the pressure in the interval was closed to 14 MPa after 90 min of injection. Therefore, the injection was stopped, the packer pressure was increased to 15 MPa, and the injection continued for 35 min. In both cases, the injections were stopped once an inflection in the gas pressure was observed indicating fracturing initiation in the COx.

3 Modelling approaches

Most of the research teams participating in the subtask A1 assumed the hypothesis of continuum medium. Quintessa adopted a thermo-poroelastic approach. This simplified approach yielded satisfactory results in DECOVALEX-2019 Task E for the numerical reproduction of the thermo-hydromechanical response of the COx (Thatcher et al., 2020). BGR-UFZ and CIMNE-UPC used elasto-plasticity defined by a failure surface. Lamcube continued with the development of their phase field method for both subtasks, initially developed for 2D geometries for DECOVALEX-2019 (Yu et al., 2021). LBNL incorporated implicit joints in their model to reproduce weak bedding planes in the COx. Ineris used a discrete approach considering elastic blocks with discrete joints. Furthermore, Ineris, Lamcube, and CIMNE-UPC decided to couple the mechanical part to the permeability to account hydraulic variations.

Regarding the research teams participating in subtask A2, the three approaches assumed a continuous medium. Furthermore, the three of them used a mechanical dependent permeability model. UPC-CIMNE used an embedded fracture permeability model. Finally, BGR-UFZ uses elasto-plasticity defined by a failure surface.

Table 3 summarizes the different approaches and the steps where they were tested.

Table 3. Modelling approaches of the research teams participating in Task A.

Team	Approach	Mech. dependent permeability model	Steps
CIMNE-UPC	Hyperbolically-modified Mohr Coulomb failure criterion	☒	A1.1, A1.2, A1.3
	Embedded fracture permeability model	☒	A2.1, A2.2
Ineris	Distinct Element Method	☒	A1.1, A1.2
Lamcube	Phase Field Method	☒	A1.1, A1.2, A1.3, A2.1, A2.2
BGR/UFZ	Visco-elastic model (2D)		A1.1, A1.2
	Drucker-Prager failure criterion		A1.2, A1.3
	Drucker-Prager failure criterion	☒	A2.1, A2.2
LBNL	Ubiquitous joint model		A1.1, A1.2
Quintessa	Poro-elasticity		A1.1, A1.2

3.1 THM formulation of a fully saturated porous media

The THM formulation used in subtask A1 assumes a fully saturated porous media. The linear momentum balance equation is described as:

$$\nabla \cdot \boldsymbol{\sigma} + \rho_{\mathrm{eq}} \mathbf{g} = \mathbf{0} \tag{1}$$

where $\boldsymbol{\sigma}$ is the total Cauchy stress (positive in compression), $\rho_{\mathrm{eq}} = (1-n)\rho_{\mathrm{s}} + n\rho_{\mathrm{w}}$ the equivalent density of the porous medium with n being the porosity, ρ_{s} and ρ_{w} the solid particle density and water density, respectively, and $\mathbf{g}$ the gravity acceleration vector.

The total stress can be decomposed into the Biot effective stress, $\boldsymbol{\sigma}'^{\mathrm{B}}$, and the pore pressure, p_{w}:

$$\boldsymbol{\sigma} = \boldsymbol{\sigma}'^{\mathrm{B}} + b p_w \mathbf{I} \tag{2}$$

with b being the Biot coefficient and $\mathbf{I}$ the identity tensor.

The Biot effective stress is expressed by the generalized Hook's law as follows:

$$\boldsymbol{\sigma}'^{\mathrm{B}} = \mathbf{C} : (\boldsymbol{\varepsilon} - 3K_b \alpha_{\mathrm{s}} (T - T_0)\mathbf{I}) \tag{3}$$

where $\mathbf{C}$ is the 4th order elasticity tensor and $\boldsymbol{\varepsilon}$ is the total strain tensor, α_{s} is the linear thermal expansion coefficient of the solid particles, K_b is the drained bulk modulus, T is the temperature and T_0 is the reference temperature.

The Terzaghi effective stress, $\boldsymbol{\sigma}'$, which is used for comparison between the research teams' results and is defined as follows:

$$\boldsymbol{\sigma}' = \boldsymbol{\sigma}'^{\mathrm{B}} + (1-b) p_{\mathrm{w}} \mathbf{I} \tag{4}$$

As suggested by Dormieux (2008) and Garg and Nur (1973), the notion of Biot effective stress correctly describes better the mechanical behavior of the rock in terms of deformation than the Terzaghi effective stress, while the notion of Terzaghi effective stress is more adapted to describe the material failure in the tensile region.

The mass balance equation of water with respect to the solid phase is given by:

$$\frac{\mathrm{d_s} n}{\mathrm{d}t} + \frac{n}{\rho_{\mathrm{w}}} \frac{\mathrm{d_s} \rho_{\mathrm{w}}}{\mathrm{d}t} + n \frac{\partial \varepsilon_{\mathrm{v}}}{\partial t} + \frac{1}{\rho_{\mathrm{w}}} \nabla \cdot (\rho_{\mathrm{w}} \mathbf{v}) = 0 \tag{5}$$

where $\frac{\mathrm{d_s} n}{\mathrm{d}t}$ is the material derivative of the porosity, ε_{v} is the volumetric strain, and $\mathbf{v}$ is the seepage velocity defined by the generalized Darcy's law:

$$\mathbf{v} = -\frac{\mathbf{K}}{\mu_{\mathrm{w}}}(\nabla p_{\mathrm{w}} - \rho_{\mathrm{w}}\mathbf{g}) \tag{6}$$

where $\mathbf{K}$ is the intrinsic permeability tensor.

Finally, the energy balance equation is written in the following form:

$$(\rho C)_{\mathrm{eq}}\frac{\mathrm{d}T}{\mathrm{d}t} - \nabla\cdot\left(\boldsymbol{\lambda}_{\mathrm{eq}}\nabla T\right) + \rho_{\mathrm{w}}C_{\mathrm{pw}}\mathbf{v}\cdot\nabla T = Q \tag{7}$$

where $(\rho C)_{\mathrm{eq}} = (1-\phi)\rho_{\mathrm{s}}C_{\mathrm{ps}} + \phi\rho_{\mathrm{w}}C_{\mathrm{pw}}$ is the equivalent heat capacity with C_{pw} and C_{ps} the specific heat capacity of water and solid skeleton, respectively, $\boldsymbol{\lambda}_{\mathrm{eq}}$ is the thermal conductivity tensor of the porous medium, and Q is the heat source. Note that the 3rd term in the L.H.S. of eq. (7) can be neglected due to the low permeability of the COx.

3.2 Hydro-mechanical formulation of two-phase flow

The linear momentum balance equation is similar to eq. (1) with the difference of the equivalent density. In this case, $\rho_{\mathrm{eq}} = (1-n)\rho_{\mathrm{s}} + nS_{\mathrm{l}}\rho_{\mathrm{l}} + nS_{\mathrm{g}}\rho_{\mathrm{g}}$, with ρ_{l}, and ρ_{g} the densities respectively of liquid and gas. S_{l} and and S_{g} are the liquid and gas saturation.

The notion of a generalized effective stress $\boldsymbol{\sigma}''$ is defined as follows (Bishop, 1959):

$$\boldsymbol{\sigma}'' = \boldsymbol{\sigma} - b(S_{\mathrm{l}}p_{\mathrm{l}} + S_{\mathbf{g}}p_{\mathbf{g}})\mathbf{I} \tag{8}$$

with p_{l} and p_{g} being the pressures of liquid and gas phases, respectively.

The mass balance of water ($\beta = \mathrm{w}$) and nitrogen ($\beta = \mathrm{N_2}$) in liquid and gas phases with respect to the solid phase can be written as follows (Olivella et al., 1994):

$$\frac{\mathrm{d_s}}{\mathrm{d}t}\left(nS_{\mathrm{l}}\rho_{\mathrm{l}}^{\beta} + nS_{\mathrm{g}}\rho_{\mathrm{g}}^{\beta}\right) + \nabla\cdot\left(\mathbf{J}_{\mathrm{l}}^{\beta} + \mathbf{J}_{\mathrm{g}}^{\beta}\right) + \left(S_{\mathrm{l}}\rho_{\mathrm{l}}^{\beta} + S_{\mathrm{g}}\rho_{\mathrm{g}}^{\beta}\right)\frac{1}{\rho_{\mathrm{s}}}\frac{\mathrm{d_s}}{\mathrm{d}t}\left((1-n)\rho_{\mathrm{s}}\right) +$$
$$\left(S_{\mathrm{l}}\rho_{\mathrm{l}}^{\beta} + S_{\mathrm{g}}\rho_{\mathrm{g}}^{\beta}\right)\frac{\partial\varepsilon_{\mathrm{v}}}{\partial t} = 0 \tag{9}$$

The 1st and 2nd terms in the RHS correspond respectively to the storage and the flux of the specie β in the liquid and gas phases. The 3th term is the storage of the solid phase, and the 4th term is a hydromechanical coupling term related to the volumetric deformation.

The total flux of each specie in the liquid and gas phases are:

$$\mathbf{J}_{\mathrm{l}}^{\mathrm{w}} = \rho_{\mathrm{l}}^{\mathrm{w}}\mathbf{v}_{\mathrm{l}},\ \mathbf{J}_{\mathrm{g}}^{\mathrm{w}} = \rho_{\mathrm{g}}^{\mathrm{w}}\mathbf{v}_{\mathrm{g}} + \mathbf{i}_{\mathrm{g}}^{\mathrm{w}} \tag{10}$$

$$\mathbf{J}_{\mathrm{l}}^{\mathrm{N_2}} = \rho_{\mathrm{l}}^{\mathrm{N_2}}\mathbf{v}_{\mathrm{l}} + \mathbf{i}_{\mathrm{l}}^{\mathrm{N_2}},\ \mathbf{J}_{\mathrm{g}}^{\mathrm{N_2}} = \rho_{\mathrm{g}}^{\mathrm{N_2}}\mathbf{v}_{\mathrm{g}} + \mathbf{i}_{\mathrm{g}}^{\mathrm{N_2}} \tag{11}$$

with $\mathbf{v}_{\mathrm{l}}$, $\mathbf{v}_{\mathrm{g}}$ the advective fluxes respectively of liquid and gas phases; $\mathbf{i}_{\mathrm{g}}^{\mathrm{w}}$, $\mathbf{i}_{\mathrm{l}}^{\mathrm{N_2}}$, and $\mathbf{i}_{\mathrm{g}}^{\mathrm{N_2}}$ the diffusion fluxes respectively for water vapor, dissolved nitrogen, and dry nitrogen.

According to Darcy's law, the advective flux may be written as for any phase $\alpha =$ l, g:

$$\mathbf{v}_{\alpha} = -\frac{1}{\mu_{\alpha}}\mathbf{K}_{\alpha}(\nabla p_{\alpha} - \rho_{\alpha}\mathbf{g}) \tag{12}$$

with $\mathbf{K}_{\alpha}$ is the water and gas permeability tensors:

$$\mathbf{K}_{\mathrm{w}} = \mathbf{K}^{\mathrm{sat}}K_{\mathrm{r,w}} \tag{13}$$

$$\mathbf{K}_{\mathrm{g}} = \mathbf{K}^{\mathrm{dry}}K_{\mathrm{r,g}} \tag{14}$$

where $\mathbf{K}^{\mathrm{sat}}$ and $\mathbf{K}^{\mathrm{dry}}$ are the liquid and gas permeability tensors in saturated and dry conditions, respectively, and $K_{\mathrm{r,w}}$ and $K_{\mathrm{r,g}}$ are their respective relative permeability. The notion of intrinsic permeability is not valid for COx as it has been shown that the gas permeability in dry conditions and water permeability in saturated conditions can differ in several orders of magnitude (M'Jahad et al., 2017; Zhang and Rothfuchs, 2004).

The water relative permeability is given by Mualem-van Genuchten model, such that:

$$K_{\mathrm{r,w}} = \sqrt{S_e}\left[1 - \left(1 - S_e^{1/m_{\mathrm{VG}}}\right)^{m_{\mathrm{VG}}}\right]^2 \tag{15}$$

where S_{e} is the effective saturation:

$$S_{\mathrm{e}} = \left[1 + \left(\frac{p_{\mathrm{c}}}{p_{\mathrm{VG}}}\right)^{n_{\mathrm{VG}}}\right]^{-m_{\mathrm{VG}}} \text{ with } S_{\mathrm{e}} = \frac{S_{\mathrm{l}} - S_{\mathrm{res}}}{S_{\mathrm{max}} - S_{\mathrm{res}}} \tag{16}$$

with p_{c} is the capillary pressure, S_{res} is the residual saturation, p_{VG} is the Van Genuchten gas entry pressure, m_{VG} and n_{VG} are Van Genuchten parameters such as: $m_{\mathrm{VG}} = 1 - 1 \,/\, n_{\mathrm{VG}}$.

The gas relative permeability curve is a cubic function:

$$K_{\mathrm{r,g}} = (1 - S_{\mathrm{l}})^3 \tag{17}$$

3.3 CIMNE-UPC

3.3.1 Step A1 – Heat fracturing

CIMNE-UPC uses advanced non-associate elastoplastic constitutive model with damage and nonlocal formulation, which is an enhanced version of the model for argillaceous rocks proposed by Mánica et al. (2021) . The yield surface is defined by a hyperbolically-modified Mohr Coulomb failure criterion (Gens et al., 1990; Mánica et al., 2018):

$$F = \sqrt{\frac{J_2}{f_d(\Theta)} + (c' + p_t \tan\varphi)^2} - (c' + p' \tan\varphi) \tag{18}$$

with c', φ being asymptotic cohesion and friction angle, p_t isotropic tensile strength, p' the Biot's mean effective tress, J_2 second invariant of the deviatoric stress tensor and Θ Lode's angle. The term $f_d(\Theta)$ defines the shape of the yield surface in the deviatoric plane and it is expressed as:

$$f_d(\Theta) = \alpha_{\mathrm{MC}}(1 + B_{\mathrm{MC}} \sin\Theta)^{n_{\mathrm{MC}}} \tag{19}$$

with α_{MC}, B and n_{MC} parameters that provide a family of yield surfaces. A representation of the yield surface in the p -J_2 and in the octahedral plane are shown in Figure 8.

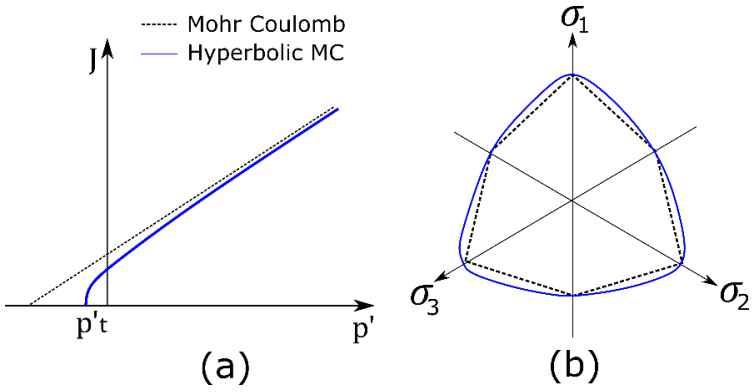

Figure 8. Representation of the yield surface in a) p-J plane and b) octahedral plane.

The non-associated flow rule is based on the yield criterion F. The hardening-softening model is adopted, and an isotropic non-linear hardening-softening law is used to reproduce the strength evolution.

3.3.2 Step A2 – Gas fracturing

CIMNE-UPC uses a viscoplastic model with a Mohr-Coulomb failure criterion with softening. Cohesion is a nonlinear function of porosity that decreases as dilatant deformation develops. Fracture occurs due to dilatancy induced by shear and/or extension.

The effective stress is given by the net mean stress tensor as follows:

$$\boldsymbol{\sigma}'' = \boldsymbol{\sigma} - b\,\max\left(p_{\mathrm{g}}, p_{\mathrm{l}}\right) \tag{20}$$

The intrinsic permeability is decomposed into matrix and discontinuity/fracture components. The former varies with porosity while the latter varies with fracture aperture.

$$\mathbf{K}_{\mathrm{l}} = K_{\mathrm{r,l}}(\mathbf{K}_{\mathrm{matrix}} + K_{\mathrm{fracture}}\,\mathbf{I}),\ \mathbf{K}_{\mathrm{g}} = K_{\mathrm{r,g}}(\mathbf{K}_{\mathrm{matrix}} + K_{\mathrm{fracture}}\,\mathbf{I}) \tag{21}$$

The matrix permeability component is computed as:

$$\mathbf{K}_{\mathrm{matrix}} = \mathbf{K}_0^{\mathrm{sat}}\frac{(1-n_0)^2}{n_0^3}\frac{n^3}{(1-n)^2} \tag{22}$$

where $\mathbf{K}_0^{\mathrm{sat}}$ is considered as the initial intrinsic permeability.

The intrinsic permeability of the fracture is controlled, assuming laminar flow, by aperture of the internal fractures b_{fracture} as

$$K_{\mathrm{fracture}} = \frac{b_{\mathrm{fracture}}^2}{12} \tag{23}$$

where b_{fracture} depends on the strain level according to

$$b_{\mathrm{fracture}} = b_0 + \langle \varepsilon - \varepsilon_0 \rangle a \leq b_{\max} \tag{24}$$

where ε and ε_0 refer to current and initial strains, respectively (with ε > 0 meaning extension), and the fractures width b_0 and $b_{\max}$ are material properties.

The parameter p_{VG} is calculated as

$$p_{\mathrm{VG}} = p_{0,\mathrm{VG}}\sqrt[3]{\frac{K_0^{\mathrm{sat}}}{K_{\mathrm{l}}}} \tag{25}$$

where $P_{0,\mathrm{VG}}$ is the initial gas entry pressure and K_0^{sat} is the initial permeability. It should be noted that the retention curve may change with the opening of fractures as pore size controls the gas entry value, and fractures may represent large pores leading to a reduction of gas entry value.

3.4 Ineris

Ineris' model is based on the Distinct Element Method (Cundall, 1971; Millard et al., 1995). The model domain is composed of a discrete block assembly whose interfaces are modeled as joints and discretized by contact points (Figure 9).

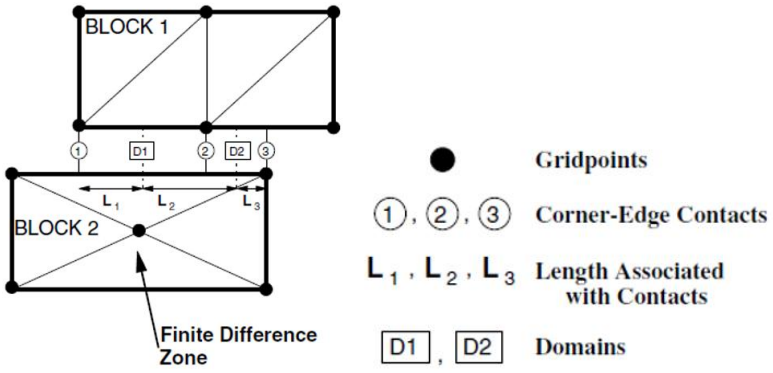

Figure 9. Contacts and domain between two deformable blocks.

The mechanical behaviour is described by linear elasticity for the blocks and a Mohr-Coulomb friction law with tensile failure for the joints. The stress-displacement relation for the joints is driven by normal and shear stiffnesses, K_{n} and K_s, respectively:

$$\Delta\sigma_{\mathrm{n}} = \begin{cases} -k_{\mathrm{n}}\Delta u_{\mathrm{n}}, & \sigma_{\mathrm{n}} \leq \sigma_{\mathrm{t}} \\ 0, & \sigma_{\mathrm{n}} > \sigma_{\mathrm{t}} \end{cases} \tag{26}$$

$$\Delta\tau_s = \begin{cases} -k_s\Delta u_s, & |\tau_s| \leq \tau_{\max} \\ \mathrm{sign}(\Delta u_s)\,\tau_{\max}, & |\tau_s| > \tau_{\max} \end{cases} \tag{27}$$

where σ_{n} and τ_s are the normal and shear stresses; Δ denotes increment. Δu_{n} and Δu_{s} are the increments of the normal and shear displacements, σ_{t} and $\tau_{\max}$ are the tensile and the shear strength, the latter is expressed as follows:

$$\tau_{\max} = c_{\mathrm{j}} + \sigma_n \tan(\varphi_{\mathrm{j}}) \tag{28}$$

being c_{j} and φ_{j} the cohesion and the friction angle, respectively.

The model considers that the fluid flow is only possible through the joints and is described as follows:

$$Q = -K_{\mathrm{j}} + a^3 \frac{\Delta p}{L_{\mathrm{j}}},\ a = a_0 + \Delta a \tag{29}$$

where K_{j} and a are respectively the permeability and aperture of the joint that are function of the normal displacement. L_{j} is the length of the joint domain.

3.5 Lamcube

Lamcube has developed a THM damage model based on the phase field method which approximates the crack topology by a smooth transition of a scalar variable called "crack phase field" $d(\mathbf{x})$ taking the unit value on the crack surface and decreasing to zero away from it. The crack phase field variable can be determined by solving the following boundary value problem in the domain Ω (Miehe et al., 2010):

$$\begin{cases} d - l_d^2 \Delta d & \text{in } \Omega \\ d(\mathbf{x}) = 1 & \text{on } \Omega \\ \nabla d(\mathbf{x}) \cdot \mathbf{n} & \text{on } \partial\Omega \end{cases} \tag{30}$$

with l_d being a length scale parameter controlling the width of smeared cracks.

In the framework of the variational approach (Francfort and Marigo, 1998), the total energy functional includes the energy required to create a crack:

$$E(\mathbf{u}, d) = \int_\Omega W_e(\mathbf{u}, d)\, \mathrm{d}\Omega + g_c \int_\Omega \gamma(d, \nabla d)\, \mathrm{d}\Omega \tag{31}$$

where g_c is the material toughness of damage, and $\gamma(d, \nabla d)$ the crack density function.

The 4th order elasticity tensor is derived from eq. (31):

$$\mathbf{C}^d(d) = h(d)\mathbb{P}_\sigma^+ : \mathbf{C} + \mathbb{P}_\sigma^- : \mathbf{C} \tag{32}$$

where $\mathbb{P}_\sigma^+$ and $\mathbb{P}_\sigma^-$ are the stress projection operators of the tensile and compressive stress, respectively. The variable $h(d) = (1-d)^2(1-k) + k$ is a degradation function with k being a small value that ensures positive definiteness after the material is fully damaged ($d = 1$). The induced damage is also coupled with the liquid and gas permeabilities:

$$\mathbf{K}^{\mathrm{sat}} = \mathbf{K}_0^{\mathrm{sat}} \exp(\beta_d d)\,, \ \mathbf{K}^{\mathrm{dry}} = \mathbf{K}_0^{\mathrm{dry}} \exp(\beta_d d) \tag{33}$$

where β_d is a dimensionless parameter that controls the evolution rate of permeability, $\mathbf{K}_0^{\mathrm{sat}}$ and $\mathbf{K}_0^{\mathrm{dry}}$ are the initial saturated and dry permeabilities.

Furthermore, Lamcube uses a multiscale homogenization approach (Murakami, 2014) at the microscopic scale and at the mesoscopic scale representing the pores and the mineral inclusions, respectively. The porosities and the volume fraction of mineral inclusions at these two scales are inhomogeneous and follow a standard Weibull probability function.

3.6 BGR/UFZ

3.6.1 Step A1 – Heat fracturing

BGR/UFZ combines the Lubby-2 model (Heusermann et al., 2003) combined with a Drucker-Prager failure criterion and tension cut-off. The yield condition and the plastic potential are expressed as follows:

$$\begin{aligned} \Phi_{pl}(\sigma,\kappa) &= \sqrt{\frac{2}{3}\sigma_d{:}\,\sigma_d} + \alpha\,\mathrm{tr}(\sigma) - y(\kappa) = 0 \\ \widehat{\Phi}_{pl}(\sigma,\kappa) &= \sqrt{\frac{2}{3}\sigma_d{:}\,\sigma_d} + \beta\,\mathrm{tr}(\sigma) - y(\kappa) = 0 \end{aligned} \tag{34}$$

with the following material functions:

$$\alpha = \frac{2\sin\phi}{\sqrt{3}(3-\sin\phi)}, \quad \beta = \frac{2\sin\psi}{\sqrt{3}(3-\sin\psi)} \quad y(\kappa) = \frac{6c\cos\phi}{\sqrt{3}(3-\sin\phi)} \tag{35}$$

where σ_d is the deviatoric stress, ϕ is the internal friction angle, ψ is the dilation angle, and $y(\kappa)$ is the yield stress depending on the hardening parameter, and c is the cohesion.

The Lubby-2 model considers the strain rate tensor as the sum of the elastic strain rate tensor $\dot{\boldsymbol{\varepsilon}}^{\mathrm{e}}$ and the visco-elastic strain rate tensor $\dot{\boldsymbol{\varepsilon}}^{\mathrm{ve}}$ (Kolditz, 2012) . The visco-elastic strain tensor is defined as:

$$\dot{\boldsymbol{\varepsilon}}^{\mathrm{ve}} = \dot{\boldsymbol{\varepsilon}}^{\mathrm{tr}} + \dot{\boldsymbol{\varepsilon}}^{\mathrm{ss}} \tag{36}$$

with

$$\dot{\boldsymbol{\varepsilon}}^{\mathrm{tr}} = \frac{3}{2}\frac{1}{\bar{\eta}_k}\left(1 - \frac{\bar{G}_k\varepsilon^{\mathrm{tr}}}{q}\right)\mathbf{S} \tag{37}$$

and

$$\dot{\boldsymbol{\varepsilon}}^{\mathrm{ss}} = \frac{3}{2}\frac{1}{\bar{\eta}_m}\mathbf{S} \tag{38}$$

where $\bar{\eta}_k$ is the Kelvin viscosity modulus, $\bar{\eta}_m$ is the Maxwell viscosity modulus, $\bar{G}_k$ denotes the Kelvin shear modulus, $\varepsilon^{\mathrm{tr}}$ is the equivalent transient creep strain, and $\mathbf{S}$ stands for the deviatoric stress tensor.

3.6.2 Step A2 – Gas fracturing

The mechanical constitutive model is based on a Drucker-Prager cap yield criterion with perfect plasticity and associated flow rule with constant dilation and friction angles. The model allows yielding under hydrostatic pressure and tension cut off:

$$F(\boldsymbol{\sigma}) = \sqrt{J_2} + \frac{1}{2}\alpha_{DP} I_1^2 + l_{DP} I_1 - \lambda_{DP} \tag{39}$$

with

$$l_{DP} = \frac{2\sin(\varphi)}{\sqrt{3}(3-\sin(\varphi))},\ \lambda_{DP} = \frac{6c\cos(\varphi)}{\sqrt{3}(3-\sin(\varphi))} \tag{40}$$

where I_1 is the first invariant of the Cauchy stress tensor and J_2 is the second invariant of the stress deviator, α_{DP} is a plastic flow parameter, l_{DP} and λ_{DP} are material constants derived from the friction angle φ and cohesion c according to eq. (40).

The permeability depends on the dilatancy to reproduce the appearance of micro fractures in the COx, described as follows:

$$\mathbf{K}^{\mathrm{sat}} = f(\Delta\varepsilon_{\mathrm{v}}) \exp\left(b_1 \Delta\bar{\varepsilon}^{p}\right) \mathbf{K}_0^{\mathrm{sat}},\ \mathbf{K}^{\mathrm{dry}} = f(\Delta\varepsilon_{\mathrm{v}}) \exp\left(b_1 \Delta\bar{\varepsilon}^{p}\right) \mathbf{K}_0^{\mathrm{dry}} \tag{41}$$

with

$$f(\Delta\varepsilon_{\mathrm{v}}) = \begin{cases} -10^{b_2 \Delta\varepsilon_{\mathrm{v}}} & \text{compaction} \\ 10^{b_3 \Delta\varepsilon_{\mathrm{v}}} & \text{extensiton} \end{cases} \tag{42}$$

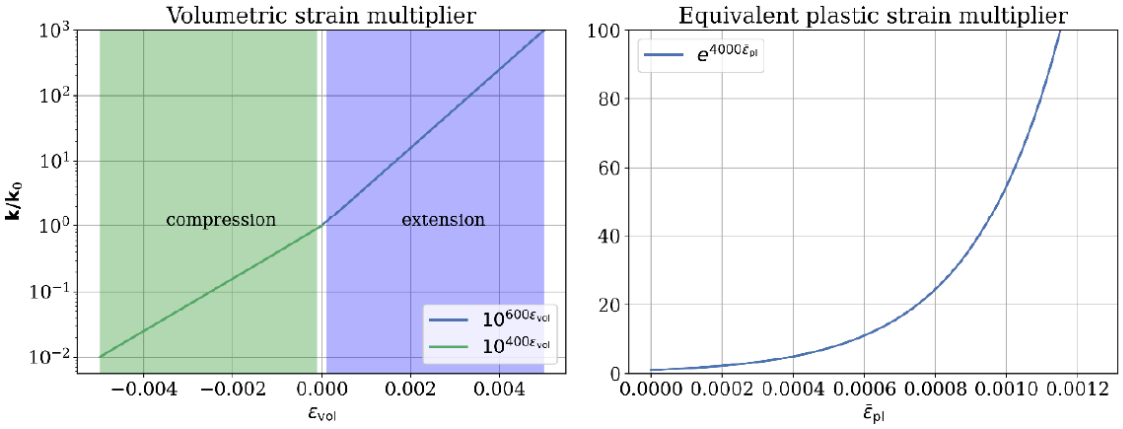

Figure 10. Dilatancy dependent permeability model with calibrated values.

The excavation-induced fracture network around boreholes is reproduced by using the Failure index permeability developed by Wang et al., (2021). Then, the permeability evolves as a function of the strain dependent permeability model presented above. Additional information of the combination of these two models can be found in.

3.7 LBNL

LBNL employs the Anisotropy Ubiquitous joint model (Sainsbury and Sainsbury, 2017) implemented in the TOUGH-FLAC simulator (Rinaldi et al., 2022; Rutqvist, 2011) that couples the mechanical part (FLAC3D) with the thermo-hydraulic part (TOUGH3). This model assumes that each element consists of a matrix and a joint, representing the orientation of weak planes (e.g., bedding orientation).

The behavior of both COx matrix and weak planes are governed by a non-associative Mohr-Coulomb model with tension cutoff. The yield condition for the COx matrix is expressed as follows:

$$f^s = \sigma_1 + \sigma_3 N_\varphi - 2c\sqrt{N_\varphi} \tag{43}$$

$$f^t = \sigma_3 + \sigma^t \tag{44}$$

where superscripts s and t indicate respectively shear and tension, φ is the friction angle, c is the cohesion, σ^t is the tensile strength, and

$$N_\varphi = \frac{1+\sin(\varphi)}{1-\sin(\varphi)} \tag{45}$$

The maximum tensile strength is specified by the following equation:

$$\sigma^t_{\max} = \frac{c}{\tan\phi} \tag{46}$$

The cohesion and tensile strength of the COx matrix were assumed to follow the softening rule shown in the equation below

$$y = (y_{peak} - y_{post})\exp(-b_{post}\epsilon^{p,eq}) + y_{post}\exp(-b_{res}\epsilon^{p,eq}) \tag{47}$$

where y is the cohesion/tensile strength, y_{peak} is the peak cohesion/tensile strength, y_{post} is the post-rupture cohesion/tensile strength, which is distinguished from the residual cohesion/tensile strength (Burland, 1990; Gens, 2013), b_{post} and b_{res} are the softening parameters, and $\Delta\epsilon^{p,eq}$ is the equivalent plastic strain.

4 Step A1 – Heat fracturing

4.1 Step A1.1 – Laboratory tests

4.1.1 Modelling specifications

Three COx samples submitted to thermal extension loading were reproduced by the research teams. The cylindrical specimens had a diameter of D = 20 mm and height of L = 38 mm, 35 mm and 34 mm for EXT1, EXT2 and EXT3, respectively. The bedding plane was oriented horizontally with respect to the axial loading.

First, the samples were loaded up to different levels of confining pressure, σ_0. Then, they were saturated with a fluid pressure of $p_{\mathrm{atm}} = 100$ kPa; swelling strains stabilized after about two days. After hydration, various initial conditions were set before heating, (Table 4).

Table 4. Initial conditions for the thermal extension tests.

Sample	σ_0 [MPa]	σ_{a0} [MPa]	σ_{r0} [MPa]	p_{w0} [MPa]	T_0 [°C]
EXT1	-8.0	-12.6	-11.8	4.9	25.0
EXT2	-5.0	-4.8	-5.6	2.1	24.0
EXT3	-12.0	-7.2	-12.4	4.0	35.0

During the thermal loading, the drainage valve was closed and the servo-control of confining pressure was switched on, to maintain radial strains to zero, while the axial total stress was kept constant on the top of the sample. Heating rates were set to 10.0°C/h for EXT1 and EXT3, and to 5.0°C/h for EXT2, respectively. The heating system stopped working for a few minutes during EXT1 and EXT2 as shown in Figure 11.

The induced pore pressure measured in the experiment can be different from the induced pore pressure obtained in perfectly undrained conditions as specified above. Volume changes in the drainage system due to the compressibility and thermal expansion of its elements and of the fluid it contains allow fluid exchange between the system and the sample, changing the specimen fluid mass. A correction of this effect is theoretically possible, but sensitive to uncertainties of both the testing device properties and the material properties (Ghabezloo and Sulem, 2010).

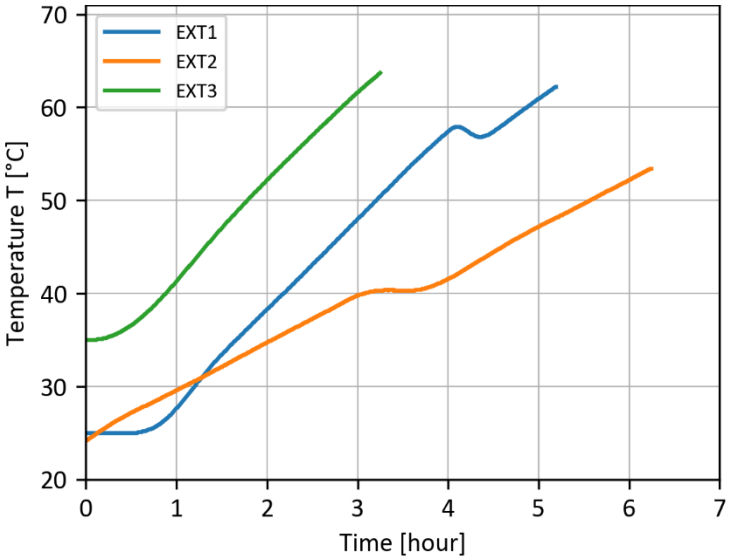

Figure 11. Temperature evolution applied during the thermal extension tests.

The teams were asked to calibrate their models against the experimental data by adjusting the different THM parameters from the reference values given in Appendix A.

The drainage system properties listed in Table 5 were calibrated by Braun et al. (2019).

Table 5. Drainage system properties (Braun et al., 2019).

Parameters	Unit	Notation	Mean	Standard deviation
Volume	mm^3	V_L	3500	100
Compressibility due to fluid pressure changes	10^{-9} 1/Pa	c_L	1.33	0.48
Compressibility due to radial confining pressure changes	10^{-9} 1/Pa	κ_L	0.44	0.14
Bulk thermal expansion coefficient	10^{-4} 1/K	β_L	0.79	0.24

4.1.2 Results and discussion

The experimental data showed that the tests were not performed in ideal conditions. For this reason, part of Step A1.1 was dedicated to evaluating the influence of the boundary conditions (i.e. draining conditions and non-constant axial stress). In addition, parameter analyses of the THM parameters of the COx were performed.

Case 1. Reference case

The reference case showed that it was not possible to reproduce the laboratory tests with one single set of parameters. On the one hand, the pore pressure build-up is slightly underestimated in EXT1 and overestimated in EXT2 and EXT3 (Figure 12). On the other hand, the effective radial stress is overestimated in all 3 tests. This could be related to a different behavior for each sample since their initial conditions were different (confinement pressure, initial pore pressure, initial temperature), the existence of small heterogeneities in the samples, and/or the conditions in which they were performed (i.e., draining conditions, constant total axial stress, null radial displacements, temperature rate, etc.). These hypotheses are evaluated in the next paragraph.

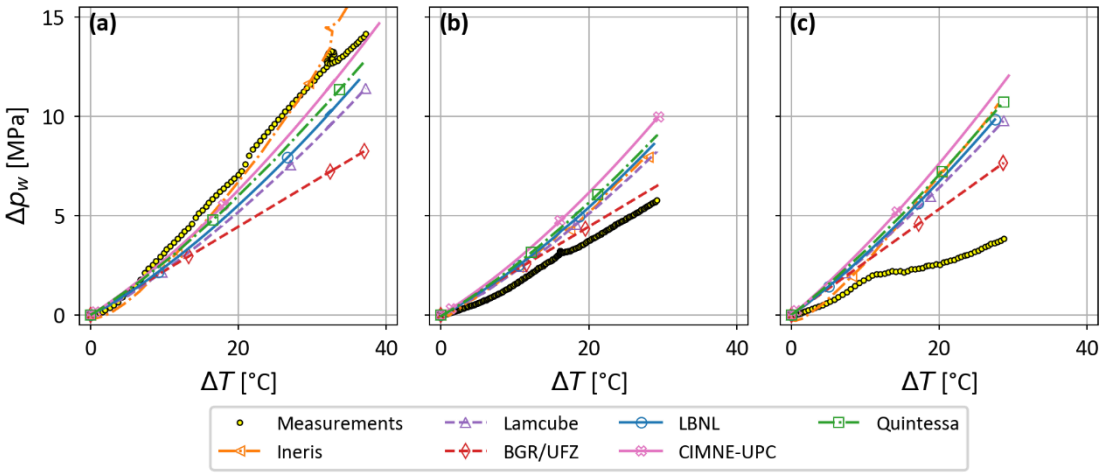

Figure 12. Pore pressure increment vs temperature increment for Case 1: (a) EXT1, (b) EXT2, and (c) EXT3.

The coefficient $\Delta p_w/\Delta T$ calculated for EXT2 and EXT3 are lower than those values reported by (Conil et al., 2020) in similar conditions (i.e. $\Delta T/\Delta p_w$ > 0.25 MPa/°C) which may indicate that EXT2 and EXT3 were not performed in fully undrained conditions as explained in Case 2. In addition, the fact that EXT2 was heated more slowly (5 °C/h) than the other two tests (15 °C/h) may have resulted in a higher fluid exchange between the drainage system and the sample. Consequently, the effective radial stress measurements are also impacted by the draining conditions leading to lower stresses than those obtained by the numerical results. This may also explain why the numerical results show a trend of the effective radial stress similar to EXT1 (increase) but not to EXT2 and EXT3 (decrease).

Case 2. Influence of draining conditions

The numerical results assuming quasi-undrained conditions improve the results of pore pressure in EXT2 and EXT3 but not in EXT1 which is consistent with the results for the reference case; the drainage system is having a higher impact on EXT2 and EXT3. This can be also observed in Figure 13, in which the effective radial stress matches better the data because of a lower pore pressure. Another hypothesis is that the calibrated drainage system parameters fit better these two tests (its parameters' uncertainty is high - see Table 5). We recall that there is a high uncertainty in these values.

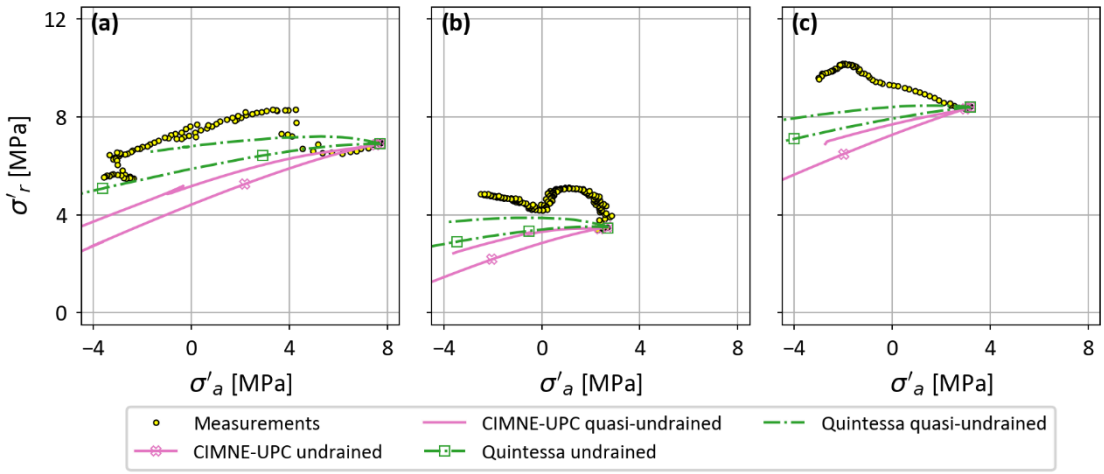

Figure 13. Effective stress path for Case 1 and 2: (a) EXT1, (b) EXT2, and (c) EXT3.

Case 3. Non-constant axial stress

Quintessa and Ineris investigated this case. The overall numerical results are slightly affected by the application of a non-constant axial stress. As expected, the effective stress path gets closer to the data for EXT1 since this is the test in which a higher variation of the axial stress was measured. In the other cases, a small variation of the axial stress has a negligible impact in the numerical results. Unlike Ineris, the results obtained by Quintessa were performed using quasi-undrained conditions. The results obtained for this case are not shown since the difference from the reference case is minimal.

Case 4. Parameter analysis

Regarding the parameter analyses, CIMNE-UPC reported that the most sensitive parameters among those tested are: E_{v}, b and α_{s}. Higher values of E_{v} and α_{s} improve

the results in terms of radial stress; lower values of E_v can improve the pore pressure of EXT2 and EXT3; and a value of $b = 0.6$ perfectly matches EXT1 but worsens EXT2 and EXT3.

The parameter analysis performed by Quintessa (Figure 14) showed the difficulty in finding a single set of parameters that fit the experimental data from the 3 tests.

This case indicates that the difference response between the samples is not explained by possible property heterogeneities, but probably by the conditions in which they were tested.

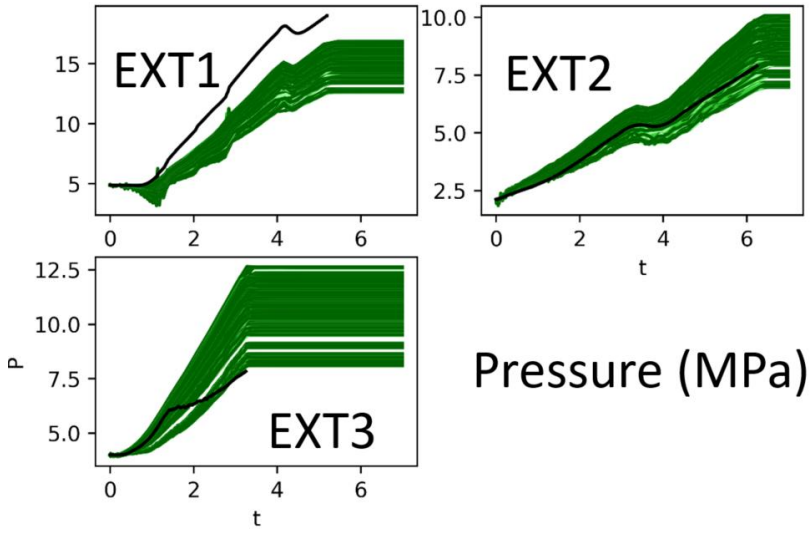

Figure 14. Evolution of pore pressure increment for Case 4 (by Quintessa).

Case 5. Failure criterion

This case shows the capability of the teams' models to reproduce the fracture occurrence. In general, the teams successfully reproduced the trends of the effective stress path of EXT1 and EXT2 (Figure 15 and Figure 16).

Lamcube used the damage (i.e., damage variable equals to 1) as a criterion to stablish whether a fracture occur or only cracks were developed. Ineris and LBNL stablished that the fracture onset begins when the Terzaghi effective stress reaches the tensile strength of the joint. For BGR/UFZ and CIMNE-UPC, the occurrence of the fracture was determined by the moment at which the yielding criterion was met.

The consideration of inhomogeneous porosity made possible to localize and create a sub-horizontal fracture with the phase field model proposed by Lamcube. This is observed in the evolution of the effective stress path the moment in which the fracture is originated, and it leads to a sudden drop in the numerical reproduction of

the 3 tests. Ineris' model reproduced a similar trend for EXT1 but with a discrete approach. For LBNL, the fracture formed on the top of the sample and the model showed a layered effect in the development of fractures due to the implicit orientation of the joints.

BGR/UFZ's model shows a better agreement with all the quantities measured, including the temperature at failure, which required a calibration step. In this model the plastic strains were localized in the axis of the sample. These results were obtained under the assumption of constant water properties and an additional calibration was needed.

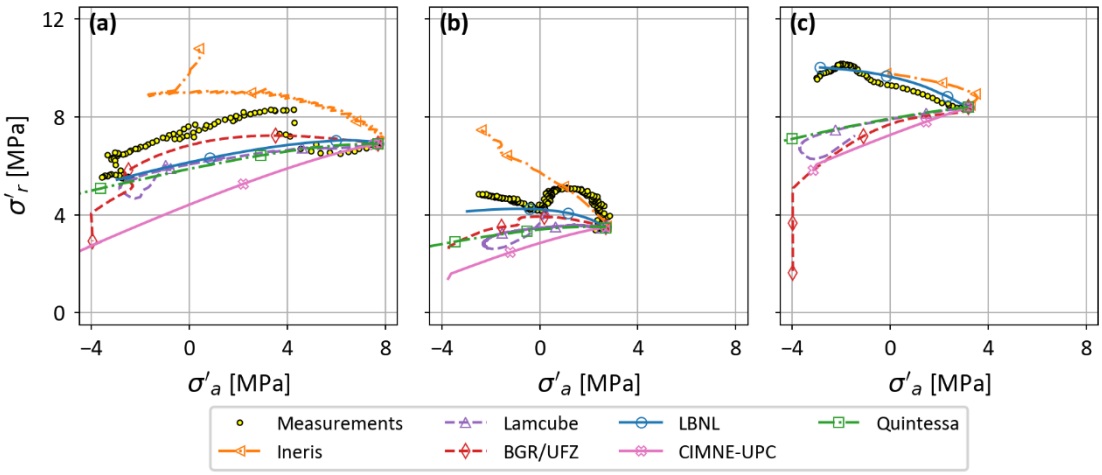

Figure 15. Effective stress path for Case 5: (a) EXT1, (b) EXT2, and (c) EXT3.

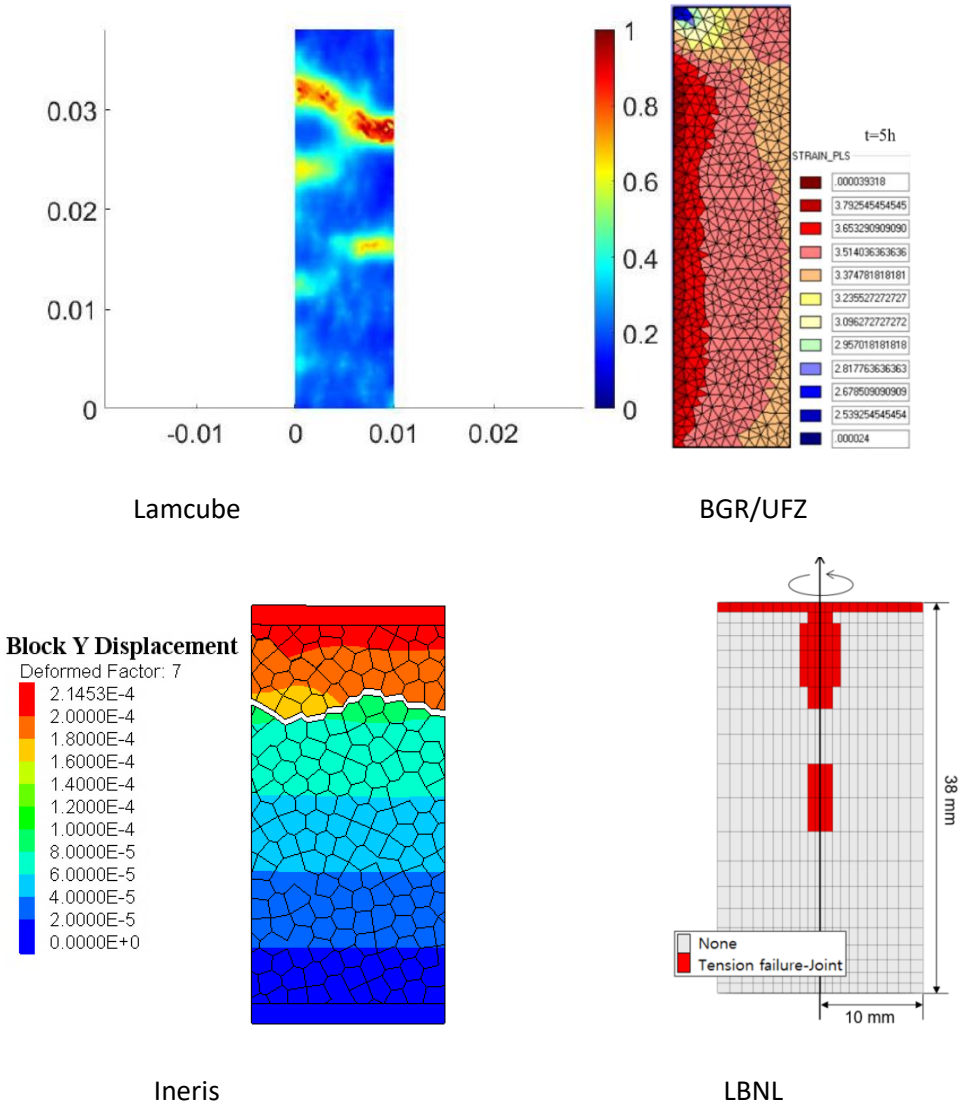

Figure 16. Spatial distribution of (Lamcube) damage obtained, (BGR/UFZ) plastic strain, (Ineris) vertical displacement, and (LBNL) joints at failure.

4.2 Step A1.2 – In-situ experiment

4.2.1 Modelling specifications

The domain for the modelling of the experiment consists of a cube with a side length of 50 m. The origin (0,0,0) of the model domain is located at the mid-distance between the heads of CRQ1720 and CRQ1721, where the boreholes intersect the drift.

The initial stress state of the domain is: a) the minor principal total stress, σ_{h} = 12.4 MPa, parallel to the x-axis, b) the major principal total stress, σ_{H} = 16.1 MPa, parallel to the y-axis, and c) the intermediate principal total stress, σ_{v} = 12.7 MPa, parallel to the z-axis. The initial pore pressure is equal to 4.7 MPa. The temperature field respects the geothermal gradient of 0.04 °C/m with a temperature of 22.0°C at 490 m deep (z = 0 m).

The GCS drift was excavated in two phases. The drift's face passed by the CRQ zone on September 15th, 2010. The GCS drift excavation resulted in a modification of the pore pressure field. There is an increase of pore pressure between 10 and 20 m from the GCS drift wall. This over pressure was not completely stabilized when the heater boreholes were excavated (September 9th, 2018).

Table 6 summarizes the boundary conditions in the far field that are suggested for the modelling. The hydromechanical boundary conditions (BCs) on the heater boreholes walls and the thermal BCs on its non-heated part depend on the modelling strategy adopted by each team. Furthermore, it has been shown that using intermediate draining conditions (i.e., a porous medium inside the boreholes with higher permeability than the surrounding rock) yields a good reproduction of the pore pressure evolution when modelling other in-situ experiments at the MHM URL [9]. It is important to bear in mind that all boreholes were not fully watertight despite of the different sealing systems. Therefore, the modelling teams were free to determine their proper way to model the pore pressure drainage through the drift and the boreholes. The heat power history is provided by Figure 4.

The teams used the THM parameters calibrated in Step A1.1. and their respective constitutive mechanical models to reproduce the thermal-hydro fracture.

Table 6. Boundary conditions in the far field of the CRQ experiment.

Boundary	Thermal	hydraulic	Mechanical
Lateral faces	No heat flux	No fluid flux	Zero normal displacements
Top face	21 °C	4.7 MPa	Pressure: 12.7 MPa
Bottom face	23 °C	4.7 MPa	Zero normal displacements
GCS drift wall	Seasonal temperature	Atmospheric pressure	Free surface

4.2.2 Results and discussion

The 3D geometries used by the research teams are presented in Figure 17. In the case of BGR/UFZ, the geometry did not consider the first 15 m of the domain assuming symmetric conditions at the mid-plane of the heaters.

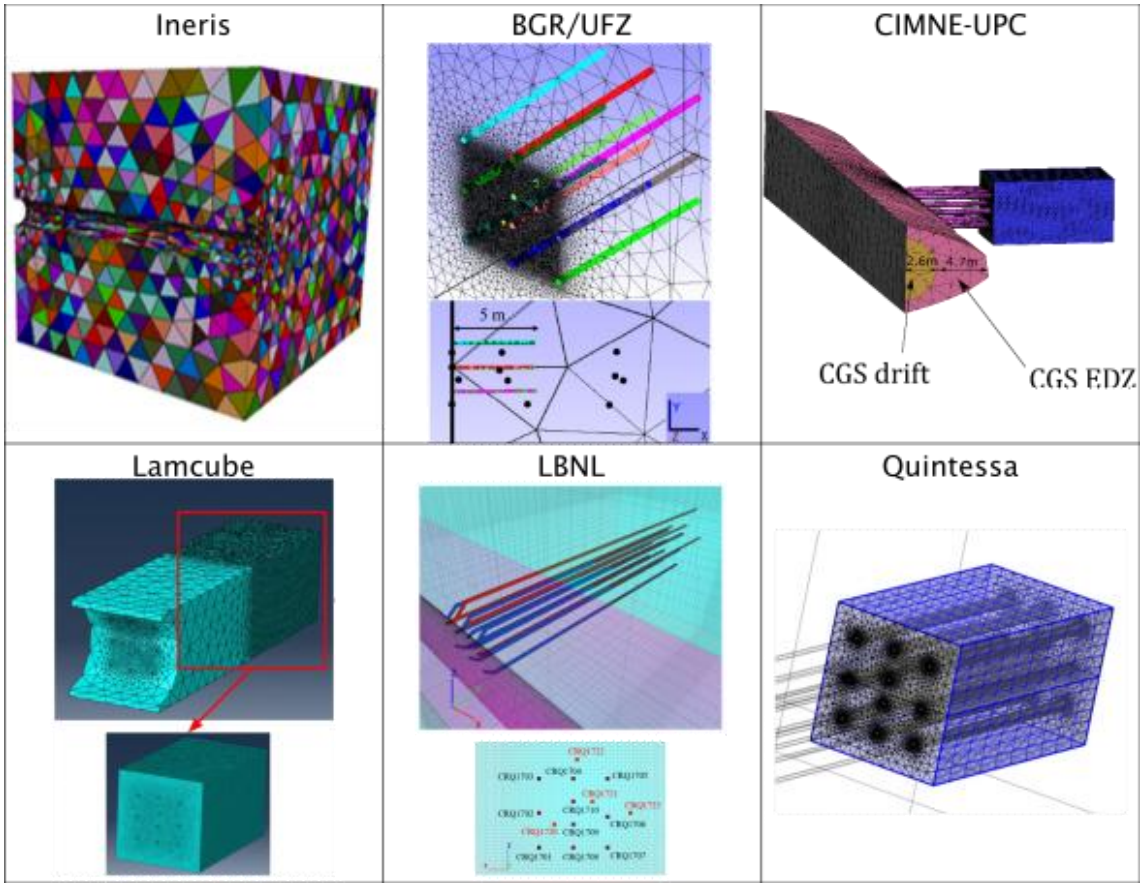

Figure 17. Geometries used by the research teams in Step A1.2.

The numerical results of temperature obtained by the research teams were in a good agreement with the measurements, as shown in Figure 18 for 3 study points: CRQ1720_01 at 25 m, CRQ1720_02 at 18 m, and CRQ1720_03 at 15 m. The maximum temperature reported by research teams was located between CRQ1709 and CRQ1710 in the first heating phase, while it was located around CRQ1709 in the second heating phase due to the damage of the heater in CRQ1704, as also deduced by the measurements.

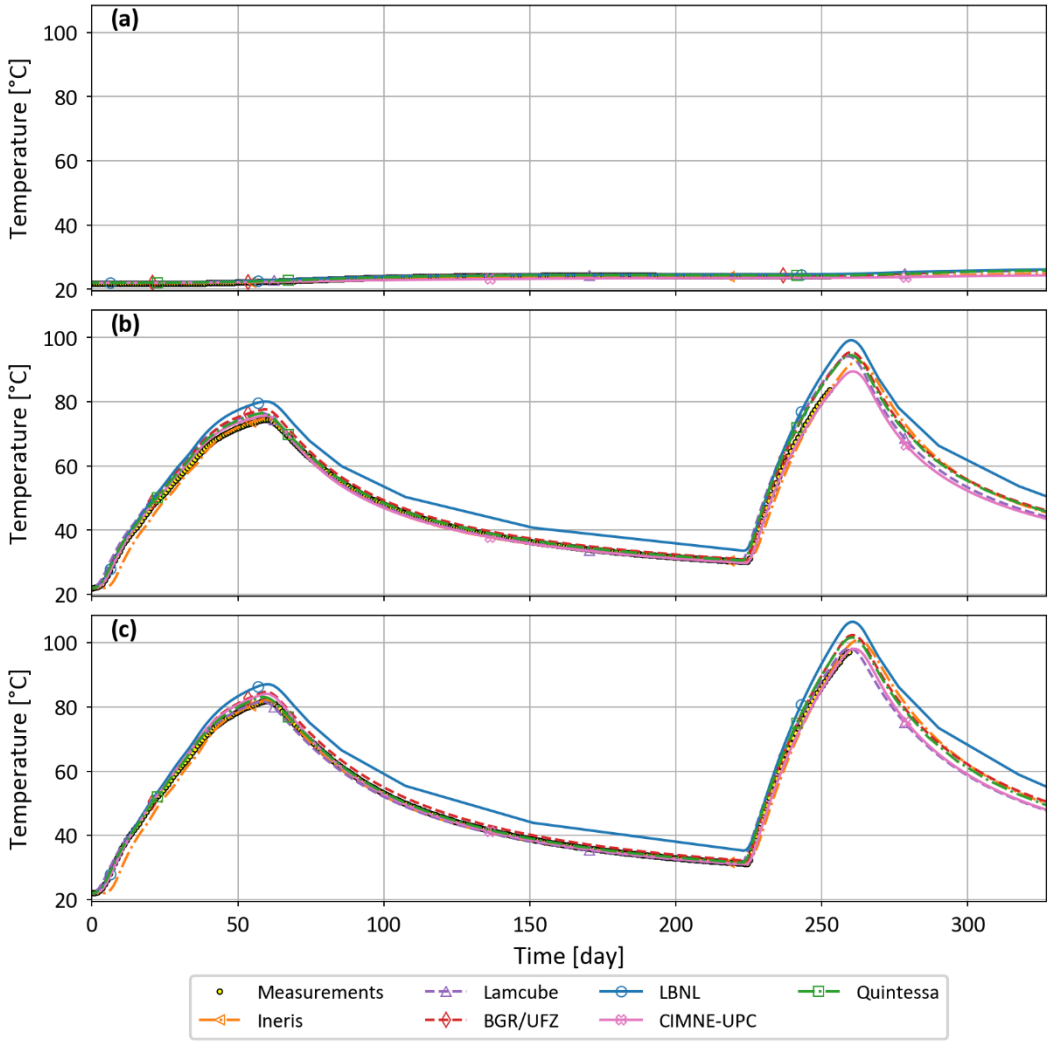

Figure 18. Comparison of numerical results and measurements of temperature: (a) CRQ1720_01, (b) CRQ1720_02, and (c) CRQ1720_03.

Regarding the pore pressures, the research teams investigated different hypotheses related to the elements in the experiment, the BCs, and the COx behavior.

Three teams tested the capabilities of the thermo-poro-elastic approach before using more advance models. Ineris and Lamcube studied respectively the influence of undrained and drained hydraulic BCs on the heater borehole walls, while UPC kept

undrained conditions around the borehole with higher permeability in the sound rock. The numerical results obtained for 3 study points are presented in Figure 19.

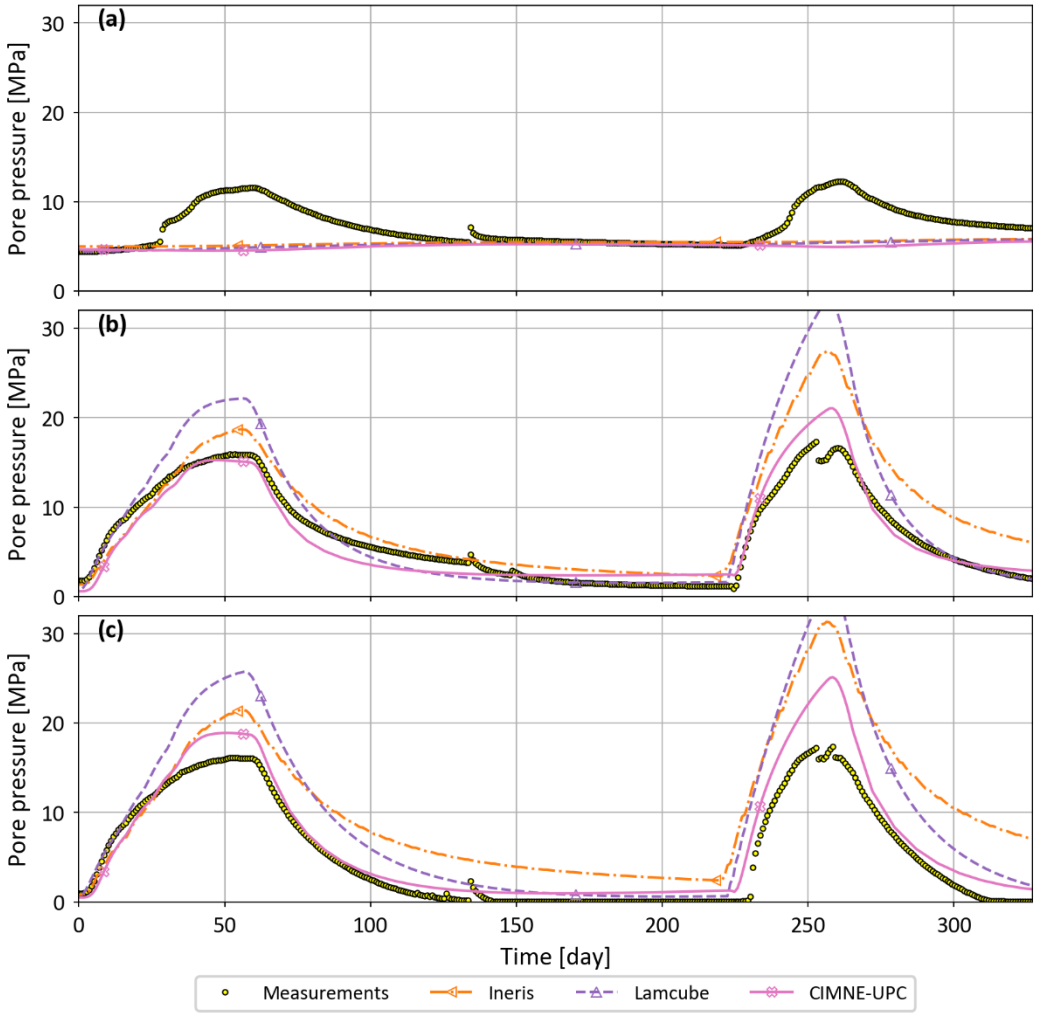

Figure 19. Comparison of numerical results obtained with thermo-poro-elasticity and measurements of pore pressure: (a) CRQ1720_01, (b) CRQ1720_02, and (c) CRQ1720_03.

The assumption of fully undrained conditions on the heater boreholes walls yielded pore pressures above 30 MPa, while pore pressures were reduced under the assumption of drained conditions as tested by Ineris. By increasing the permeability, CIMNE-UPC obtained lower pressures. However, the numerical results overpredicted the measurements in all cases, except for the study points located outside the heated zone, as for example CRQ1720_01 located at 25 m. At this location, the tested assumptions had a negligible impact. Furthermore, the fact that the research teams did not reproduce the measured overpressure confirmed that this overpressure is not related to the heating as the temperature barely increased at this zone. As explained in Plúa et al. (2023), this overpressure is related to a longitudinal laminar flow between

chambers due to the high pore pressure in the rock. The packers were not able to completely isolate such high pressures, and some of it was released towards zones less heated. This may have implied that the pore pressure measured in the heated zone was higher in the field.

Nevertheless, it was necessary to better reproduce the pore pressure as it was strongly overestimated, mainly under the assumption of undrained conditions. CIMNE-UPC and Quintessa considered an explicit excavation-induced fracture network around the heater boreholes by increasing the permeability a few orders of magnitude: 10^{-17} m^2 for CIMNE-UPC and 10^{-18} m^2 for Quintessa. This hypothesis allows longitudinal hydraulic flow towards the drift, thus reducing the modelled pore pressures and giving a better agreement with the measurements, mainly in the first heating phase (Figure 20). To get a better match with the experimental data, CIMNE-UPC and Quintessa increased the permeability of the sound rock by a factor of two. CIMNE-UPC also reduced the permeability anisotropy ratio from 3 to 2, changed the Poisson's ratio v_{vh} from 0.3 to 0.2, and increased the permeability in the excavation-induced fracture network around the GCS drift (10^{-17} m^2); however, the latter had no impact on the pore pressure evolutions in the heated zone, due to the far distance from the main gallery to this zone.

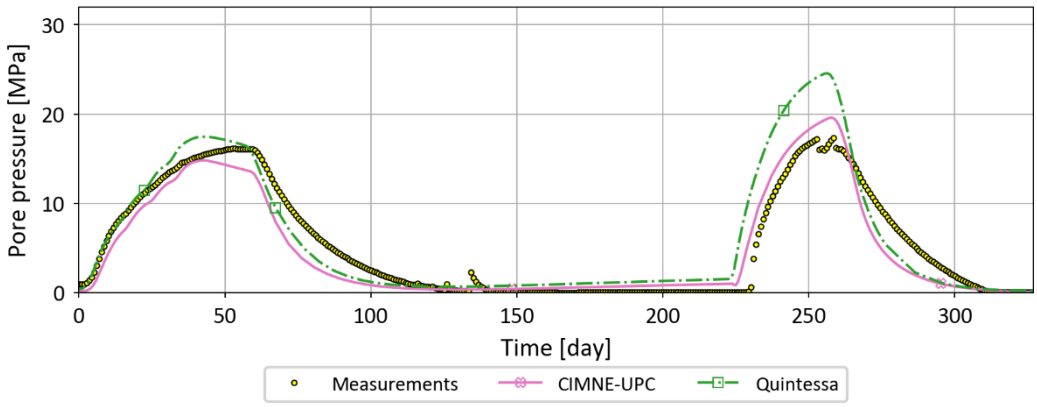

Figure 20. Comparison of numerical results obtained with thermo-poro-elasticity and excavation-induced fracture network around the heater boreholes and measurements of pore pressure in the chamber CRQ1720_03 at 15 m.

To investigate the potential fracture and its location, Quintessa used a 2D geometry to evaluate the influence of the mechanical BCs around the heater boreholes - see Figure 21. Under the assumption of undrained conditions, the effective stress analysis showed that failure initiates from the boreholes for different effective stiffness cases. The stiffnesses aimed at reproducing: free surface, null radial displacements, and intermediate cases reflecting potential uncertainties in the mechanical behavior of the

borehole. In contrast, failure was initiated from the sound rock under fully drained conditions, as this prevents high pore pressures around the heater boreholes.

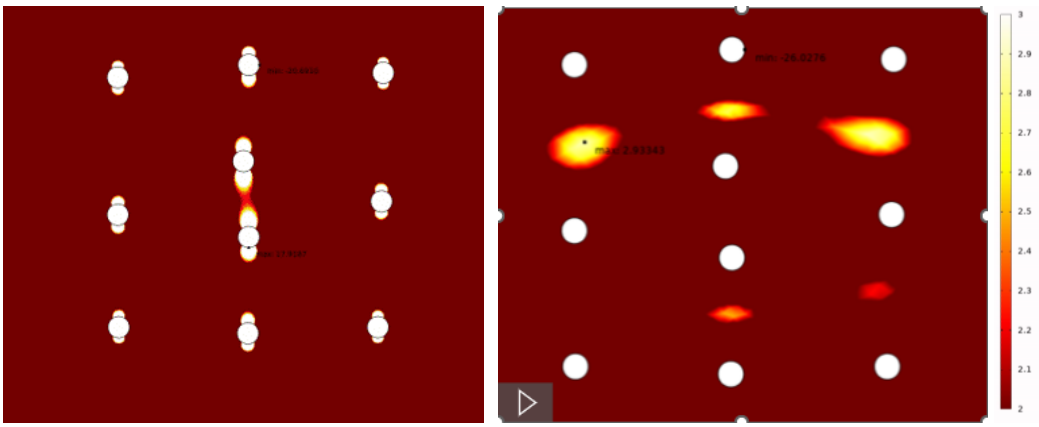

Figure 21. Terzaghi effective stresses in the vertical direction obtained by Quintessa in plane strain conditions. Zones approaching to tensile failure stresses in yellow. (Left) Undrained conditions. (Right) Drained conditions.

BGR/UFZ also tested 2D geometries under different hydraulic BCs. In this case, the heater boreholes at the corners were set at atmospheric pressure leading to a potential fracture zone originated by the boreholes under undrained conditions (Figure 22).

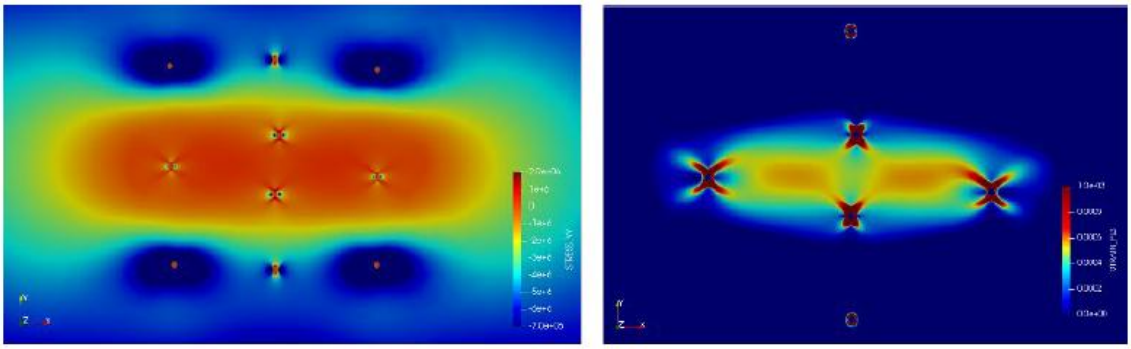

Figure 22. (Right) Vertical effective stress and (Left) peak plastic strain obtained by BGR/UFZ in plane strain conditions.

To further investigate the stress state generated by the two heating phases, BGR/UFZ and CIMNE-UPC used elastoplastic models based respectively on a Drucker Prager and a hyperbolically modified Mohr-Coulomb criterion.

The plastic strains distribution obtained by BGR/UFZ in 3D geometries showed similar patterns as those obtained in their 2D model highlighting the role of the undrained BCs around the heater boreholes. In this case, the potential fracture could appear at both sides of the central boreholes and at depth between 15 m and 16.4.

CIMNE-UPC reported no differences in the sound rock between elastic (Models 2A_09 and 2A_10) and plastic (Models 2D_14 and 2D_17) results mainly due to the limited plastic deformations developed in the plastic models (Figure 23). When introducing the explicit excavation-induced fracture network (Models 2A_10 and 2D_17), numerical predictions of pore pressure can better represent the experimental observations; however, the tensile stress state cannot be reached.

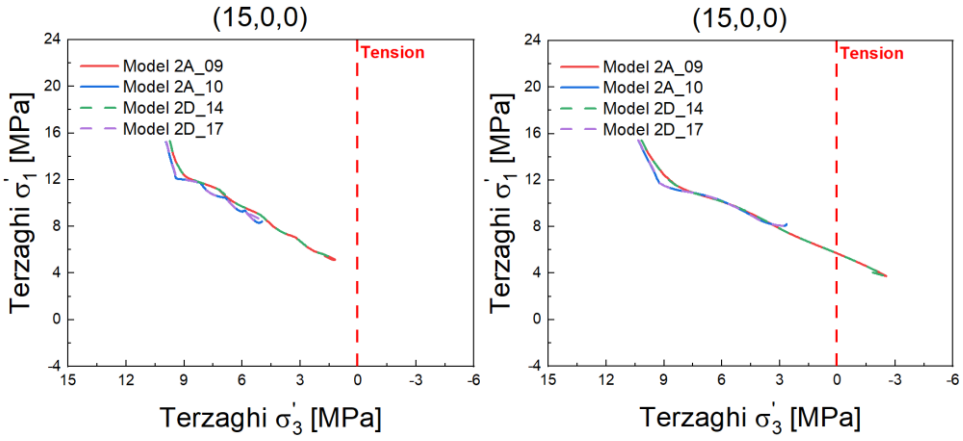

Figure 23. Terzaghi's effective stress path at study point (15, 0, 0) for different simulations. (Left) first and (Right) second heating phases.

Lamcube investigated the effect of damage. During the borehole excavation, the maximum value of the shear damage variable *ds* was about 0.23, which indicates that only micro-cracking occurs around the boreholes, and not macro-cracking. These micro cracks lead to increase in permeability, and the numerical simulation results for pore pressure were improved. The damage around the heater borehole did not increase during the first heating phase. On the contrary, the second heating induced additional damage of approximately 0.3. The damaged zone is mainly located around the two central boreholes. Lamcube also investigated the influence of material heterogeneity at the micro-scale on the fracturing. The material heterogeneity was defined by a random distribution of porosity and volumetric fraction of inclusions. The numerical results reported minor differences, indicating that the fracture location is more influenced by the BCs than the assumed heterogeneities related to porosity and volumetric fraction of inclusions.

LBNL examined the effect of the weak planes on the fracture development. Figure 43 shows a comparison of the fracture development between two cases: model with weak planes and model without weak planes. In addition, the results are presented for 3 softening rates. No shear fractures and only few tensile fractures were created in the matrix-only case. This could be because of overestimated strength properties of the COx matrix. While greater plastic shear and tensile strains developed with at higher

softening rate. It was found that reduced matrix cohesion helped to generate some shear fractures within the matrix only when the steepest softening rate was employed. According to the model with weak planes the fracture is likely to occur during the second heating phase.

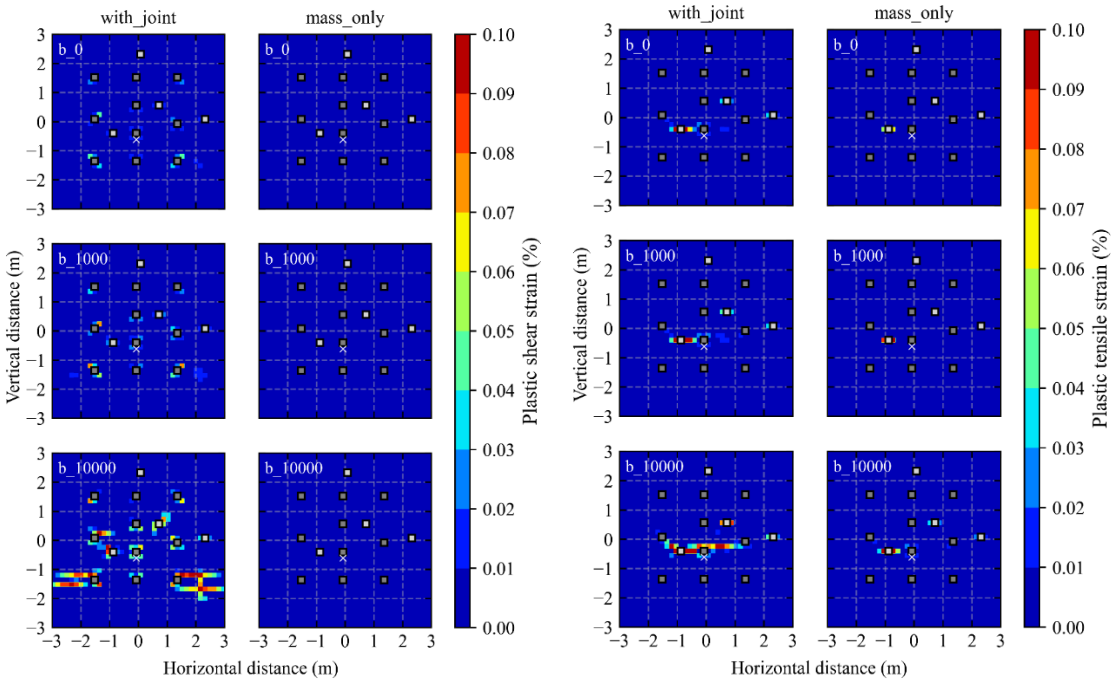

Figure 24. Spatial distributions of plastic strains at y = 15.6 m from the drift for different softening rates. (Left) Plastic shear strains and (Right) plastic tensile strains.

The final results are presented in terms of pore pressures in Figure 25. In all cases, the results overpredicted the pressure measurements in the second heating phase. All the teams concluded that higher pressures than those measured in the field were needed to obtain either a tensile stress state or meet the failure conditions. On one side, the desaturation in the heated zone made difficult to reproduce the second heating phase since the THM formulation used by the research teams assumed a saturated porous medium. On the other side, the packers were not able to completely isolate pressures above 15 MPa, implying that the pore pressure in the heated zone could have been higher that those measured by the sensors.

Regarding the fracturing mode, some research teams reported either shear or tensile fracturing, while others reported a combination of the two modes. The cores extracted in the dismantling operations only showed shear fractures.

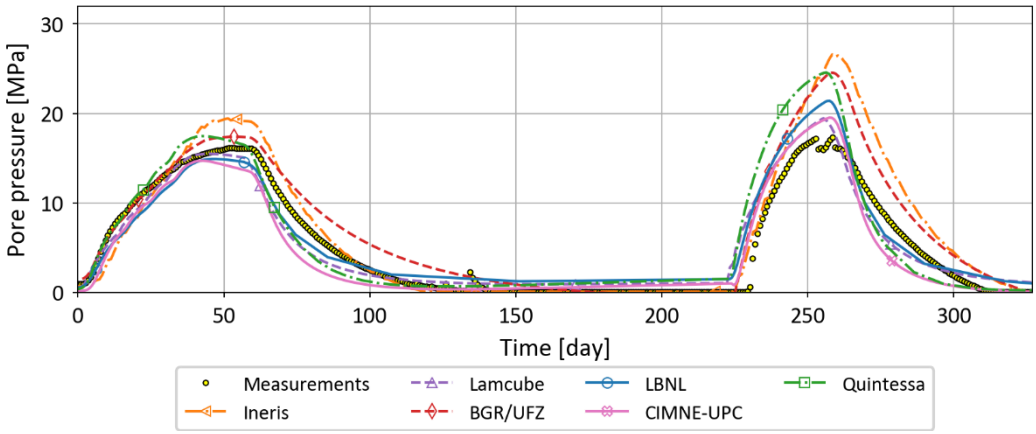

Figure 25. Final results obtained by the research teams for pore pressure at 15 m from the drift wall (CRQ1720_03).

4.3 Step A1.3 – High-Level Waste repository

4.3.1 Modelling specifications

The main objective of Step 1.3 is to investigate the initiation of thermal hydraulic fracturing at the repository scale and its location. This step is based on Step 4 of D2019 Task-E in which the research teams investigated how to make reliable numerical modelling at the repository scale.

The domain consists in a vertical cross-section of the repository at the mid-plane of the HLW disposal cells. The domain is assumed to lie in the 2D xy-plane; strains perpendicular to the plane are assumed to be zero. The assumption of plane strain conditions is reasonable for 150 m long micro-tunnels compared to their excavated diameter: 0.8 m. The micro-tunnel is equipped with a 2.5 cm thick steel liner.

The HLW repository is located within the COx formation at a depth of 560 m (Figure 26). The distance between two parallel cells is 26.0 m. This distance was considered narrow enough to generate Terzaghi effective tensile stresses and create a fracture.

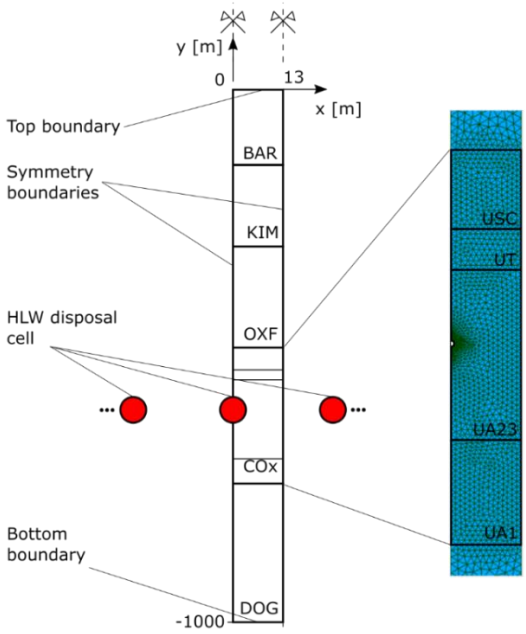

Figure 26. Model domain for the HLW repository of Step A1.3.

The initial conditions are given in Figure 27. The temperature field is defined by the geothermal gradients of each layer. The initial pore pressure corresponds to a hydrostatic state with an additional overpressure in the COx layer that increases linearly up to 0.5 MPa at the cell depth (6.1 MPa) and then decreases to recover the hydrostatic pressure in the Dogger layer. A lithostatic stress state is prescribed for the initial stress state, being isotropic in the Barrois limestone and Kimmeridgian layers and anisotropic for the rest of layers. The at-rest coefficient of lateral earth pressure varies from 1.0 to 1.3 with depth in the carbonated Oxfordian layer and then it remains constant; the largest stress is parallel to the z-direction.

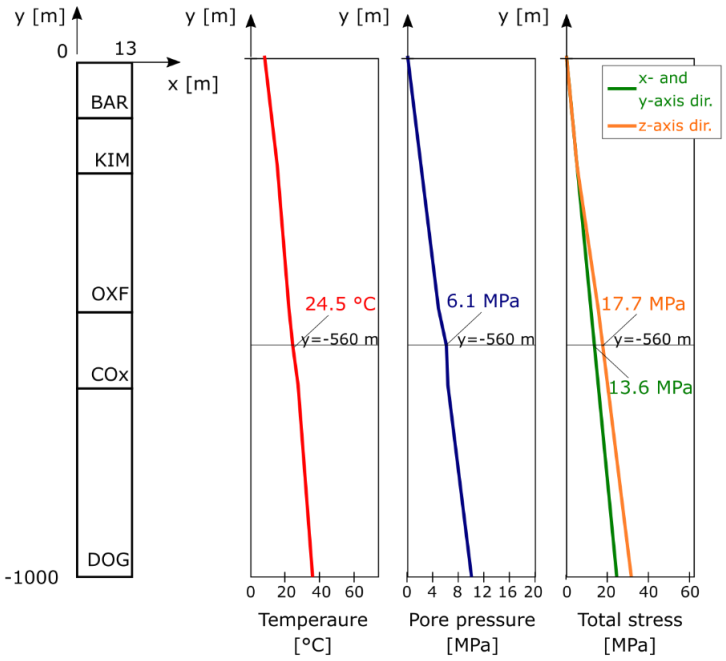

Figure 27. Initial conditions of the HLW repository of Step1.3.

The BCs on the vertical boundaries are symmetric, while the BCs on the top and bottom remain constant and equal to the initial conditions. The waste emplacement is simulated by applying the average power per unit length of the HLW packages (Figure 28).

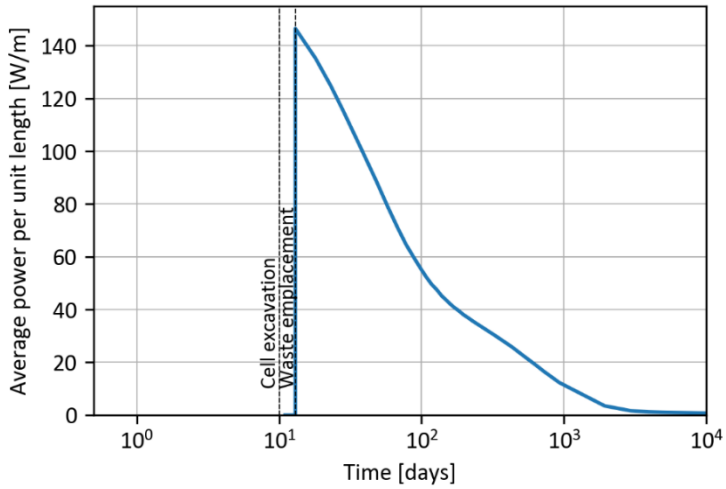

Figure 28. Average power history per unit length of the HLW packages.

The parameters for each geological layer are provided in Appendix A.

4.3.2 Results and discussion

The teams first simulated the HLW repository with the thermo-poro-elastic approach. Then, they continued with their models used in Step A1.2. The results are compared at 3 study points at the level of the HLW disposal cell with the following horizontal coordinates: P1 = 1.2 m, P2 = 6.5 m, and P3 = 13.0 m. These points are considered as far-field with respect to the HLW disposal cell as they are outside the influence of its excavation-induced fracture network. Point P3 is located at the mid-distance between two parallel HLW disposal cells.

The temperature obtained by the research teams were similar for the two approaches. Figure 29 shows the results obtained with the thermo-poro-elasticity with slight differences between teams.

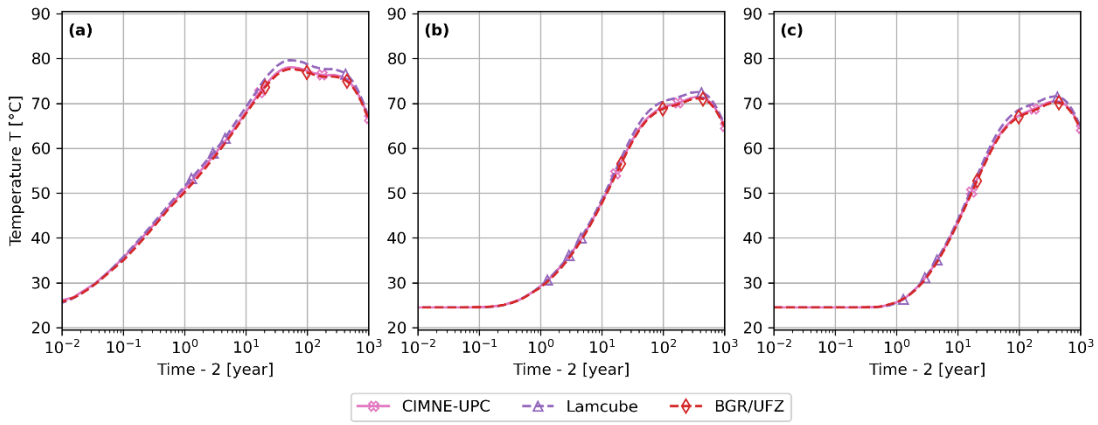

Figure 29. Temperature evolution: (a) P1, (b) P2, and (c) P3.

The pore pressure obtained with thermo-poro-elasticity by CIMNE-UPC and Lamcube were similar (Figure 30). In the case of BGR/UFZ, a slightly higher specific storage may be the reason of higher pore pressures than the other teams. Although the results between teams may vary, the peak for the 3 points is reached at the same time for each team (approximately 200 years) and at a similar magnitude. This means that the pore pressure field in the far-field is homogeneous when it reaches its peak mainly due to the narrow distance between two parallel cells.

The differences in pore pressure obtained between the research teams led to different Terzaghi effective stresses in the vertical direction (Figure 31). Nevertheless, the pore pressure was high enough to reach effective tensile stresses in the sound rock. Unlike the pore pressures, the minimum effective tensile stress is reached few years earlier at the mid-distance between two parallel HLW disposal cells than those located closer to the cells.

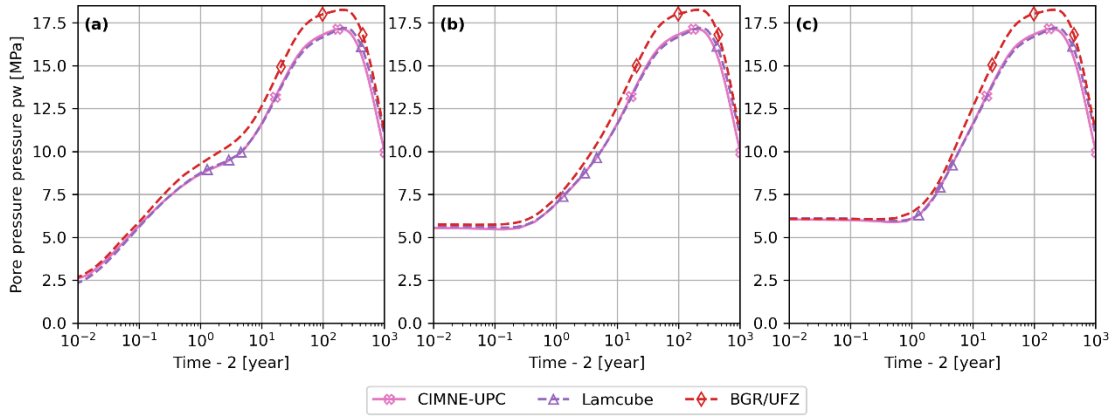

Figure 30. Pore pressure evolution for the elasticity case: (a) P1, (b) P2, and (c) P3.

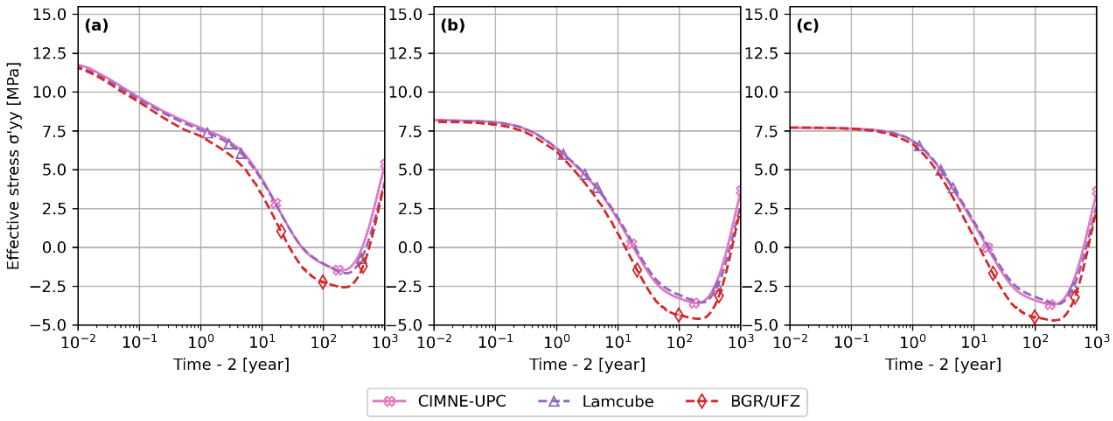

Figure 31. Vertical effective stress evolution for the elasticity case: (a) P1, (b) P2, and (c) P3.

CIMNE-UPC and Lamcube obtained pore pressures lower than those obtained with the thermo-poro-elastic approach, while BGR/UFZ obtained similar results using both approaches. The modification of the hydraulic permeability due to hydro-mechanical coupling allowed lower pore pressures in the numerical results obtained by CIMNE-UPC and Lamcube. The peak occurrence was also delayed due to the faster dissipation, although they were reached at the same time for the 3 study points as for the case of the thermo-poro-elastic approach.

BGR/UFZ developed plasticity, as their model met their failure criterion. In this case, their elastoplastic model is not coupled with permeability; therefore, pore pressures were not impacted by changes in the mechanical part.

All the research teams reached Terzaghi effective tensile stresses for the three study points, as shown in Figure 33.

The Terzaghi effective stresses obtained by CIMNE-UPC and Lamcube with their respective elastoplastic and damage models were less in tension than the equivalent models with only elasticity due to the coupling between the hydraulic and mechanical part that led to lower pressures.

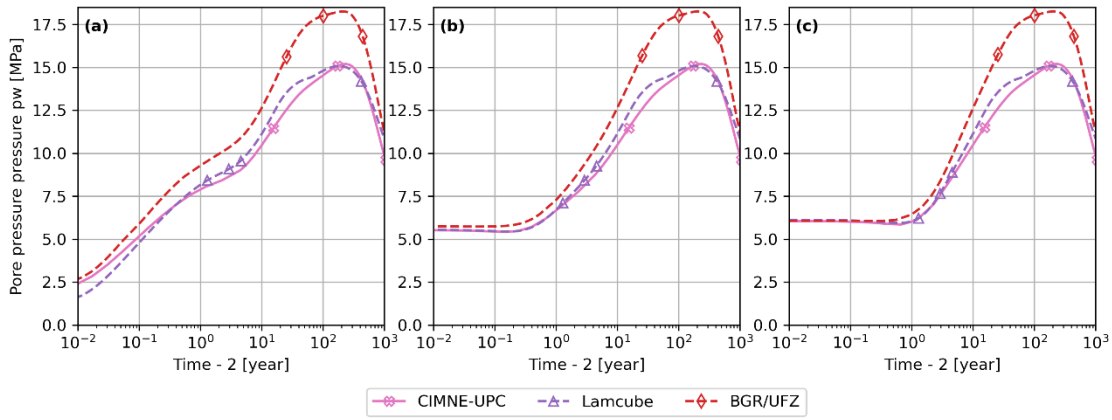

Figure 32. Pore pressure evolution for the elastoplastic/damage case: (a) P1, (b) P2, and (c) P3.

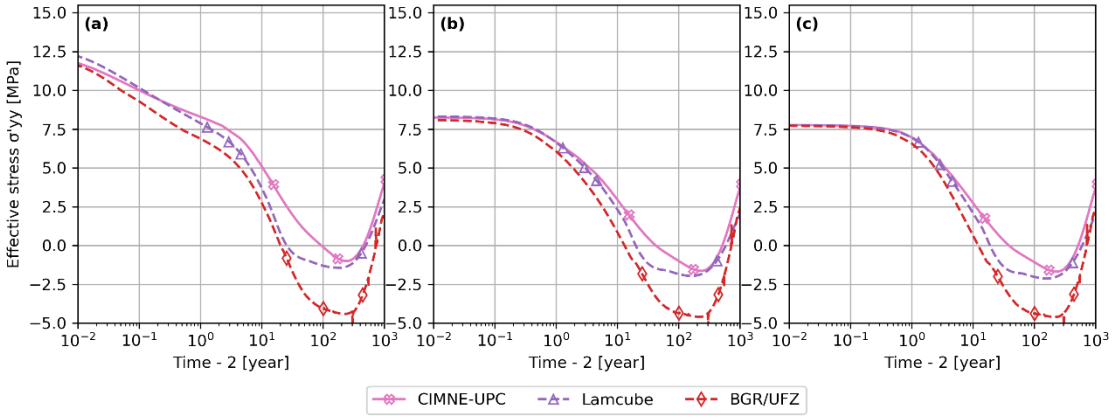

Figure 33. Vertical effective stress evolution for the elastoplastic/damage case: (a) P1, (b) P2, and (c) P3.

Figure 34 shows indicators of fracturing defined by each research team. The three research teams' results show the development of the higher effective tensile stresses from the HLW disposal cell towards the far-field by forming two diagonal bands. This agreement indicates that the fracture development is strongly influenced by the BCs, as the distance between two HLW disposal cells is small. The thermally induced fracture originates from the excavation-induced fracture network around the cell, and then propagates towards the far-field. Therefore, the tunnel separation used in this application exercise does not meet the thermal design of the French HLW repository, that requires an effective compression stress state in the far-field without any fracture development.

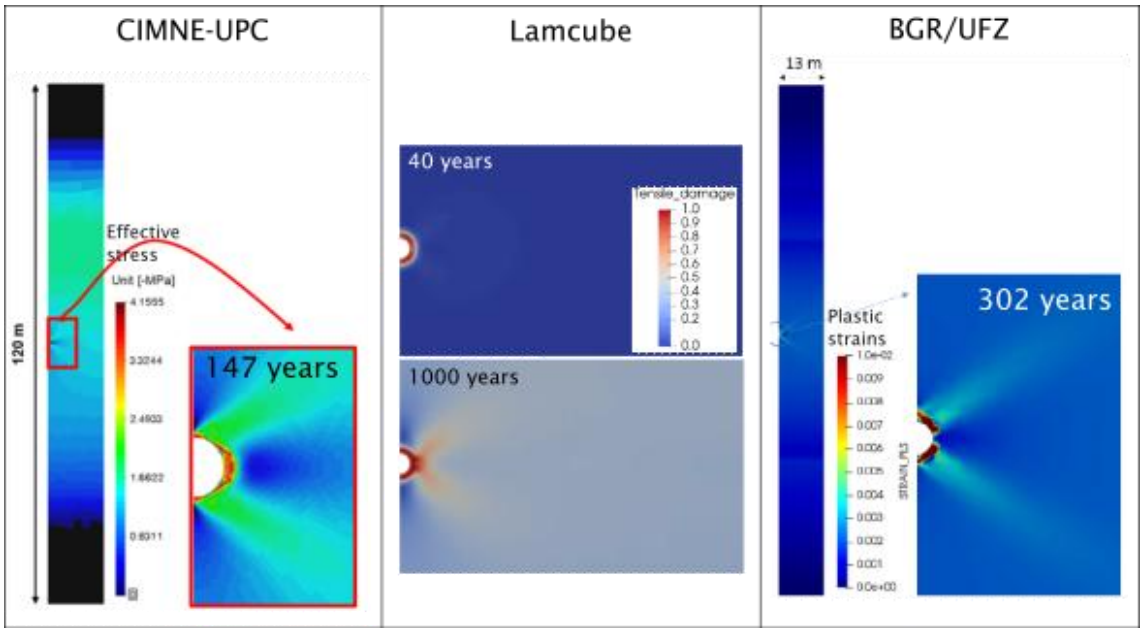

Figure 34. Indicators of failure/damage obtained by the different teams.

5 Step A2 – Gas fracturing

5.1 Step A2.1 – Benchmark exercises

5.1.1 Modelling specifications

The objective of Step A2.1 was to define conceptual models to understand the main processes in gas fracturing in the COx and study the influence of the elements composing the gas injection tests. . To this end, several benchmark exercises were performed in 2D under different conditions as follows (Table 7):

- The initial isotropic stress for B1, B2, B5 and B6, and anisotropic for B3 and B4.
- The COx was assumed to be isotropic for B1 – B4 and transversely anisotropic for B5 and B6. This anisotropy concerns the elastic properties and the intrinsic permeability.
- The mechanical constitutive model was linear elastic for B1, B3 and B5, while a model with a failure criterion was required for B2, B4 and B6.

The objective of benchmark exercises B1, B3 and B5 was not to reproduce the fracture initiation due to gas overpressure, but capture the processes related to gas diffusion.

Table 7. Description of the benchmark exercises for Step A2.1.

Benchmark exercise	Material	Initial stress state	Failure criterion
B1	Isotropic	Isotropic $\sigma_x = \sigma_y$	No
B2	Isotropic	Isotropic $\sigma_x = \sigma_y$	Yes
B3	Isotropic	Anisotropic $\sigma_x = \sigma_{\mathrm{H}}, \sigma_y = \sigma_{\mathrm{v}}$	No
B4	Isotropic	Anisotropic $\sigma_x = \sigma_{\mathrm{H}}, \sigma_y = \sigma_{\mathrm{v}}$	Yes
B5	Transversely isotropic	Isotropic $\sigma_x = \sigma_y$	No
B6	Transversely isotropic	Isotropic $\sigma_x = \sigma_y$	Yes

The simulations for the six benchmark exercises were divided into 3 stages: S1, S2 and S3. A preliminary stage, S0, is used for the generation of the initial conditions. S1 starts with the drilling of the borehole, S2 with the installation of the test interval, and S3, the main stage (t > 0), with the gas injection test.

The domain represents a cross-section at the longitudinal mid-plane of the test interval where the gas is injected into the COx (Figure 35). The COx is represented by a square of length L = 10.0 m; the borehole has a radius of R_{b} = 0.04 m; and the test interval has an outer radius equals to the borehole radius, and an inner radius of R_{i} = 0.03 m. The length in the z-axis (out-of-plane) direction is set to 1.0 m. The bedding plane is oriented parallel to the x-direction.

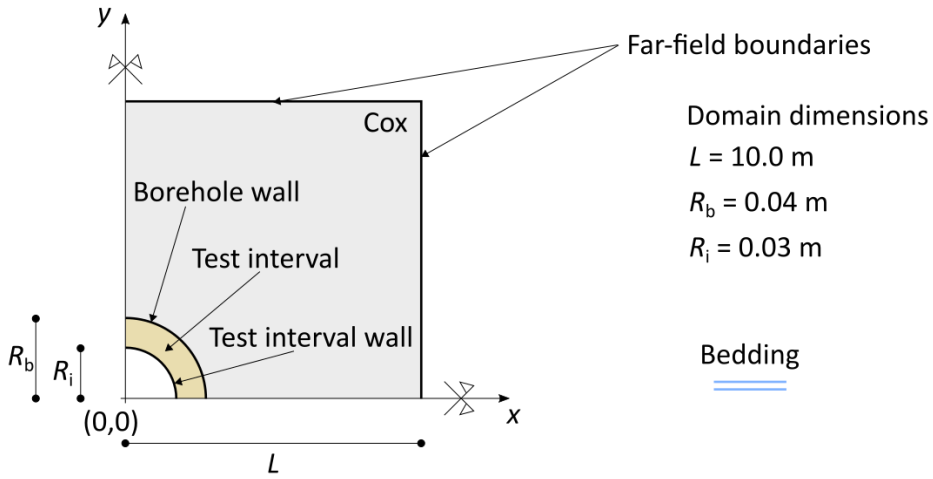

Figure 35. Model domain dimensions of the benchmark exercises for Step A2.1.

The parameters for the COx and the injection interval are provided in Appendix B.

Stage S0 corresponds to the generation of the initial conditions prior to the drilling of the borehole. The initial stress state is assumed isotropic: $\sigma_{0\mathrm{x}}$ = $\sigma_{0\mathrm{y}}$ = $\sigma_{0\mathrm{z}}$ = 12.0 MPa for B1, B2, B5 and B6; and anisotropic: $\sigma_{0\mathrm{x}}$ = 16.0 MPa, $\sigma_{0\mathrm{y}}$ = $\sigma_{0\mathrm{z}}$ = 12.0 MPa, for B3 and B4. The initial liquid pressure is p_{l0} = 4.5 MPa; and the porous medium is quasi-fully saturated (initial degree of liquid saturation is S_{l0} = 0.99).

Drilling of the borehole (S1)

The BCs on the far-field boundaries do not vary with respect to the initial conditions. The boundary conditions on the borehole wall are free surface, atmospheric pressure, and fully saturated. The duration of this stage is 30 days.

Installation of the test interval (S2)

Stage S2 requires the generation of the initial state of the test interval domain; this initialization represents the installation of the test interval. The test interval domain

has initial zero stress, the initial water pressure is a function of the initial degree of liquid saturation in the test interval (S_{l0} = 0.22) and can be obtained by finding the corresponding capillary pressure and keeping the initial gas pressure in the COx. The capillary pressure is expressed as follows:

$$p_c = p_g - p_l \tag{48}$$

The boundary conditions on the far-field boundaries do not vary with respect to the initial conditions. The boundary conditions on the test interval wall are: zero normal displacements, no water flow and no gas flow. The duration of this stage is 1 day.

Gas injection (S3)

Stage S3 starts with the injection of nitrogen gas into the COx at the specified flow rate. The boundary conditions on the far-field boundaries do not vary with respect to the initial conditions. The boundary conditions on the test interval wall are: zero normal displacements, zero water flow, and the gas flow rate is q_g = 500 mLn/min and is applied with a ramp that increases from 0 to 500 mLn/min in one hour and then it remains constant. Since only a quarter of the total domain is studied, a quarter of flow rate is applied on the test interval wall:

$$q_g = 500 \cdot 2.2 \cdot 10^{-8} \cdot 0.25 = 2.75 \cdot 10^{-6} \ [\mathrm{kg/s}] \tag{49}$$

5.1.2 Results and discussion

Benchmark exercises B1, B3 and B5

These benchmark exercises allowed the evaluation of the capabilities and limitations of each code to reproduce the conditions in which the injections tests are performed and take them into account for the specifications of the in-situ experiment. We recall that the use of a linear elastic model led to pressures that are not representative of the observations in-situ.

The comparison of the numerical results of gas pressure obtained by each team are presented for the cases with a linear elastic model: B1 in Figure 36, B3 in Figure 37, and B5 in Figure 38 and Figure 39. An important aspect in reproducing the gas injection tests is the residual gas pressure ($S_{l0} = S_{l,max} = 0.99$) provided in the specifications as the initial condition. This choice was made to avoid numerical instabilities and allow a continuous gas phase with $K_{g,r} = 10^{-6}$. This was not the case for CIMNE-UPC who did not report any numerical problems and decided to work with $S_{l0} = 1.00$. The

assumption of a residual gas pressure results in gas flux driven by advection whereas the diffusive flux is the predominant flux during the first days of injection when initial fully saturated conditions are assumed. The differences between these two assumptions are highlighted at Point PD in all 3 benchmark exercises.

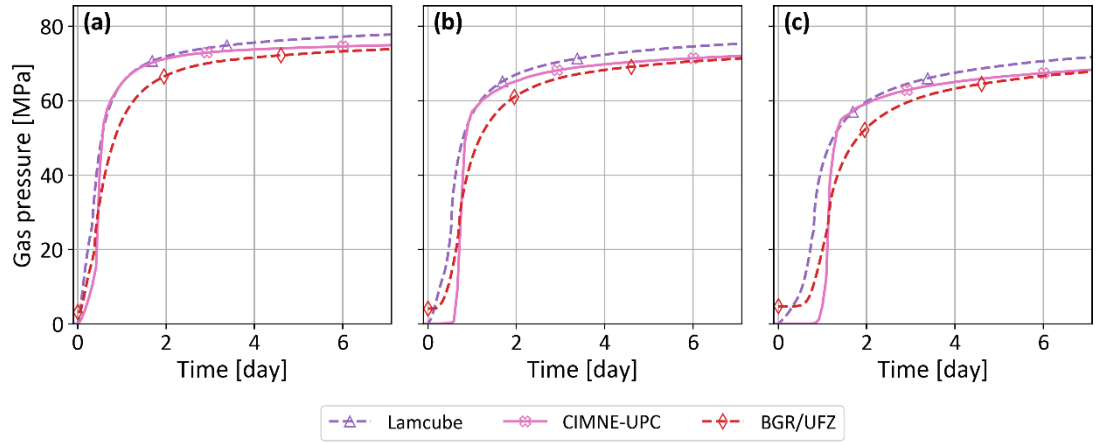

Figure 36. Evolution of gas pressure for B1: (a) PB, (b) PC, and (c) PD.

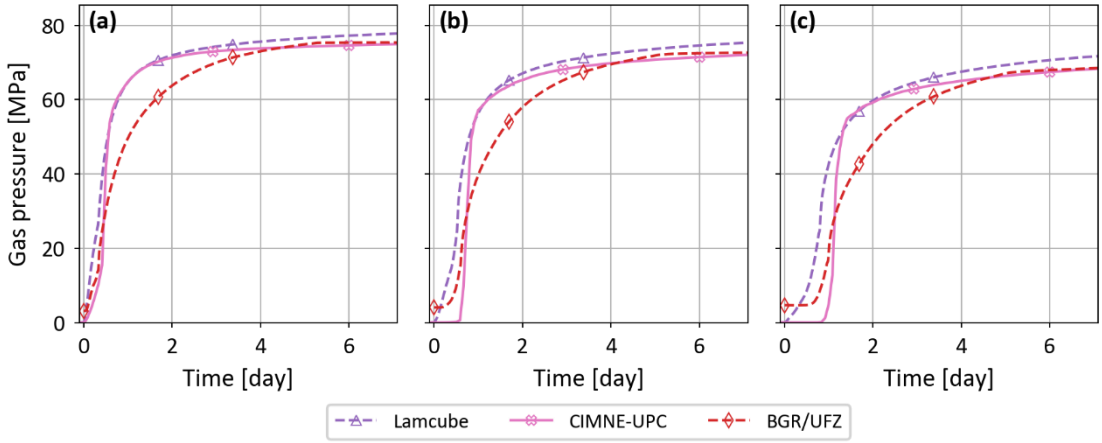

Figure 37. Evolution of gas pressure for B3: (a) PBx, (b) PCx, and (c) PDx.

For BGR/UFZ, the specified initial liquid saturation is fixed to $S_{l,0} = 0.98$ which leads to an initial capillary pressure of $p_c = 2.5$ MPa in the COx. It is an open question whether this change in the initial conditions with respect to the other teams explains the differences in the long-term response.

As general conclusions, the initial anisotropic stress state does not influence the hydro-mechanical response with respect to an initial isotropic state (similar gas pressure in both horizontal and vertical directions). On the other hand, the material anisotropy of the COx leads to a non-symmetric response with higher gas pressures in the horizontal direction.

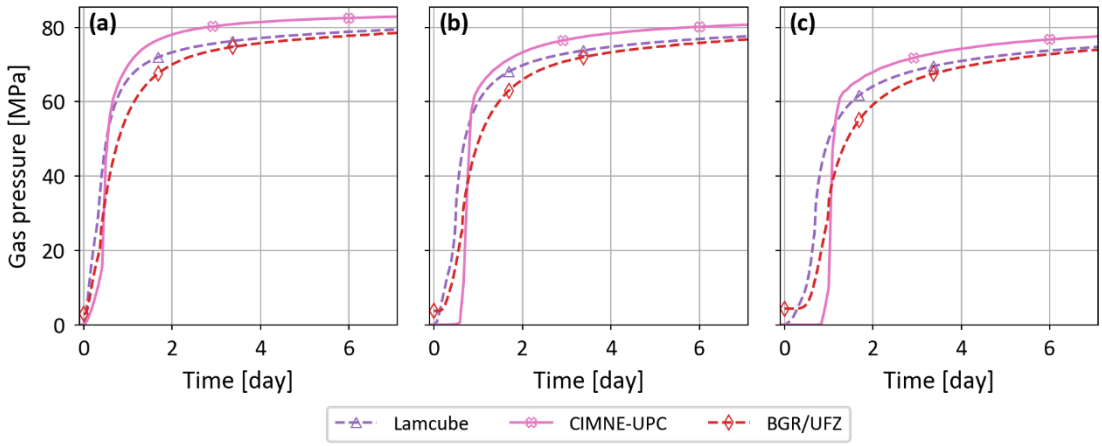

Figure 38. Evolution of gas pressure for B5: (a) PBx, (b) PCx, and (c) PDx.

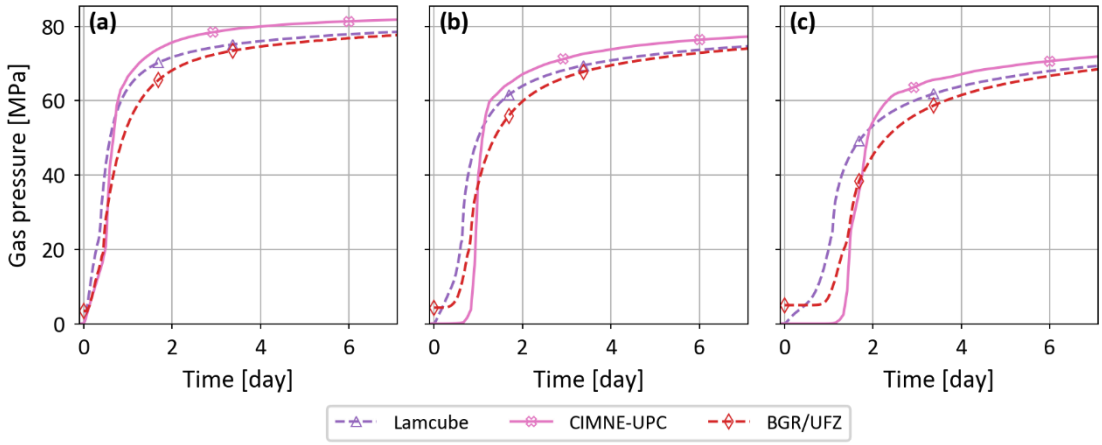

Figure 39. Evolution of gas pressure for B5: (a) PBy, (b) PCy, and (c) PDy.

Benchmark exercises B2, B4 and B6

These benchmark exercises had the objective to evaluate the capabilities of reproducing the BDZ by coupling the mechanical constitutive variables to the hydraulic properties. In this way, these exercises were useful for the assessment of the impact of the hydraulic property modifications on the gas pressure. In general, all teams obtained lower pressures than their counterpart under the hypothesis of linear elasticity. The comparison between the teams' results are given in Figure 40, Figure 41, Figure 42, and Figure 43. An important contribution of the gas pressure decrease is related to the permeability modification in the BDZ which has been taken into account by each team with different approaches.

Furthermore, the reduction of the entry gas pressure plays an important role in the response of the gas pressure and the fracture initiation; this feature was taken into

account in CIMNE-UPC's model. This can be observed in Figure 44, which show the gas pressure spatial distribution. CIMNE-UPC obtained a similar fracture orientation for B2 and B6 (approximately 45°), whereas the fracture develops horizontally for B4. Contrary to the elastic case (B3), the anisotropic stress state has a strong influence on the orientation of the fracture development. In addition, the fact that B2 and B6 show a similar response indicates that the reduction of the entry gas pressure, which is an isotropic parameter, has a stronger influence than the anisotropy considers for the elastic properties and the intrinsic permeability.

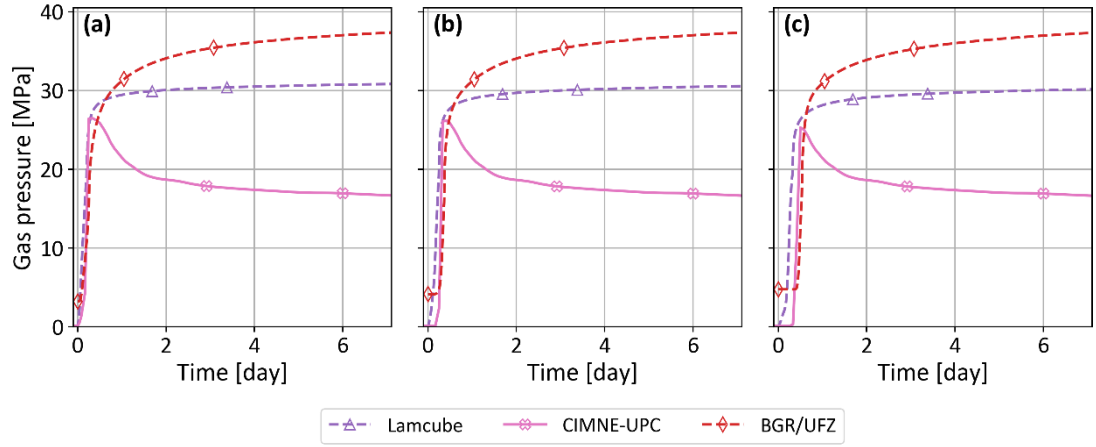

Figure 40. Evolution of gas pressure for B2: (a) PB, (b) PC, and (c) PD.

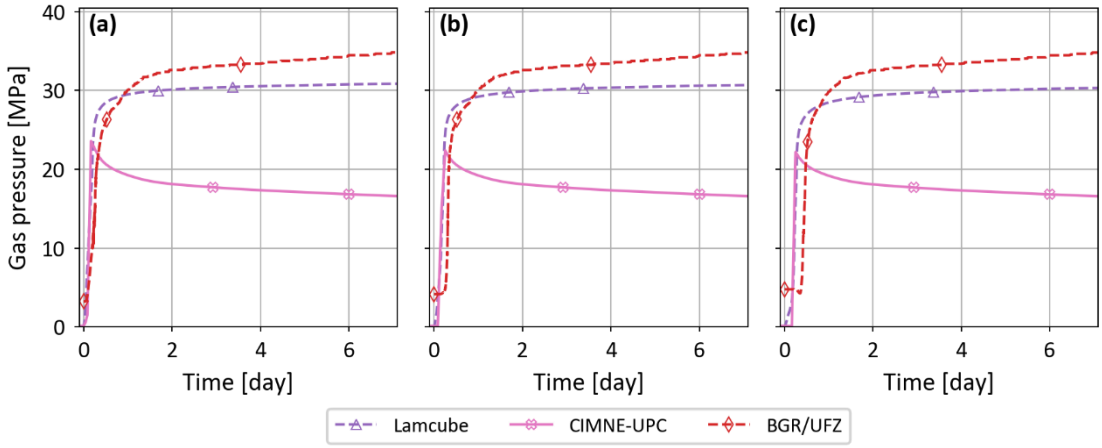

Figure 41. Evolution of gas pressure for B4: (a) PBx, (b) PCx, and (c) PDx.

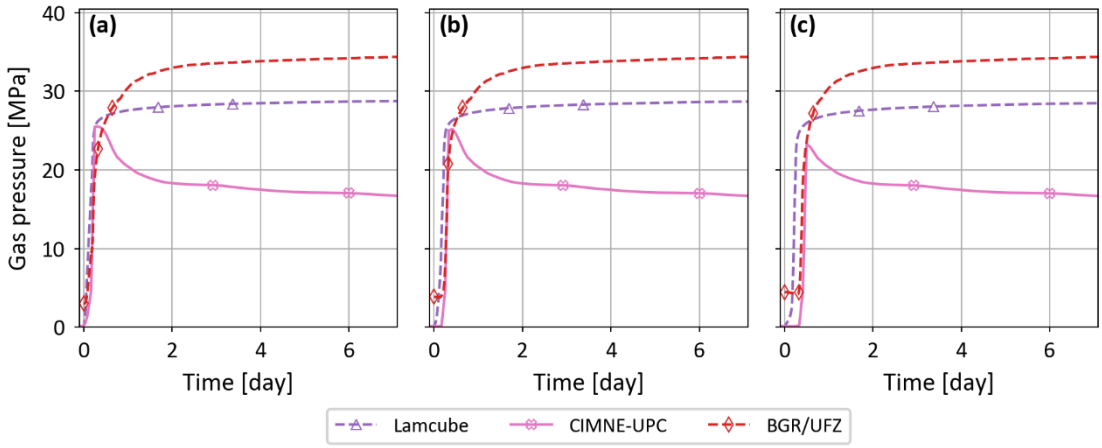

Figure 42. Evolution of gas pressure for B6: (a) PBx, (b) PCx, and (c) PDx.

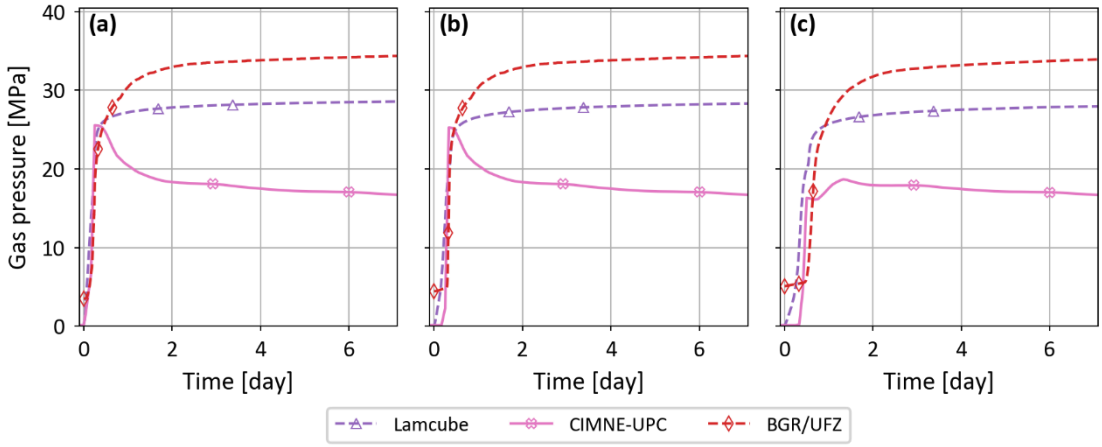

Figure 43. Evolution of gas pressure for B6: (a) PBy, (b) PCy, and (c) PDy.

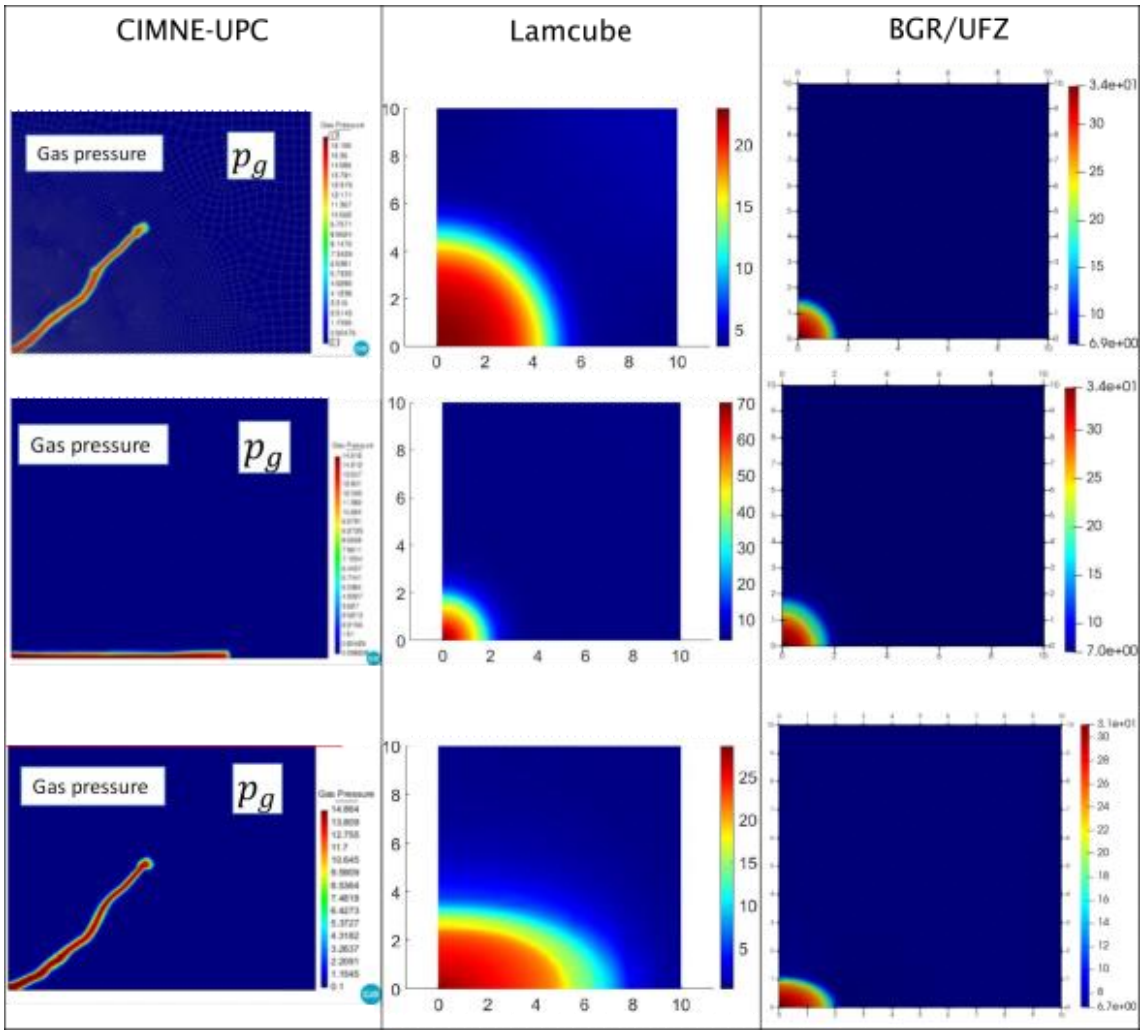

Figure 44. Gas pressure distribution: (top) B2, (middle) B4, and (bottom) B6.

5.2 Step A2.2 – In-situ experiment

5.2.1 Modelling specifications

Only one quarter of the domain was considered in the modelling of the in-situ test. It consisted of a rectangular prism with dimensions 10 m x 5 m x 5 m. The borehole axis was parallel to the x-axis, with a diameter of r_b = 0.038 m. The injection interval had a diameter of r_i = 0.033 m. The origin (0,0,0) of the domain was located at the mid-section of the injection interval. The injection test performed on the PGZ1003 borehole was used as interpretative modelling, whereas PGZ1002 was used for blind prediction.

The initial pore pressure was assumed to be uniform and equals to 4.7 MPa and fully saturated. The temperature in the domain was 20°C. The initial stress state for

PGZ1003 was 16.1 MPa parallel to the x-axis, 12.4 MPa parallel to the y-axis and 12.7 MPa in the vertical direction, with quasi-isotropic conditions in the transversal section of the borehole. The initial stress state for PGZ1002 was anisotropic in the transversal section of the borehole, being perpendicular to PGZ1003.

The simulation considered five stages: (S0) generation of the initial state, (S1) drilling of the borehole, (S2) installation of the test interval, (S3) water/gas exchange, (S4) gas injection test with a duration of 30 days that included a part of the recovery phase.

The BCs in the far field are listed in Table 8. These conditions remained unchanged for all stages. The gas injection rate applied to each test is presented in Figure 45.

Table 8. Boundary conditions in the far field for the PGZ experiment.

Boundary	Thermal	hydraulic	Mechanical
Lateral faces	No fluid flux	No fluid flux	Zero normal displacements
Top face	4.7 MPa	0.1 MPa or S_{w0} = 1	Pressure: 12.7 MPa
Bottom face	4.7 MPa	0.1 MPa or S_{w0} = 1	Zero normal displacements

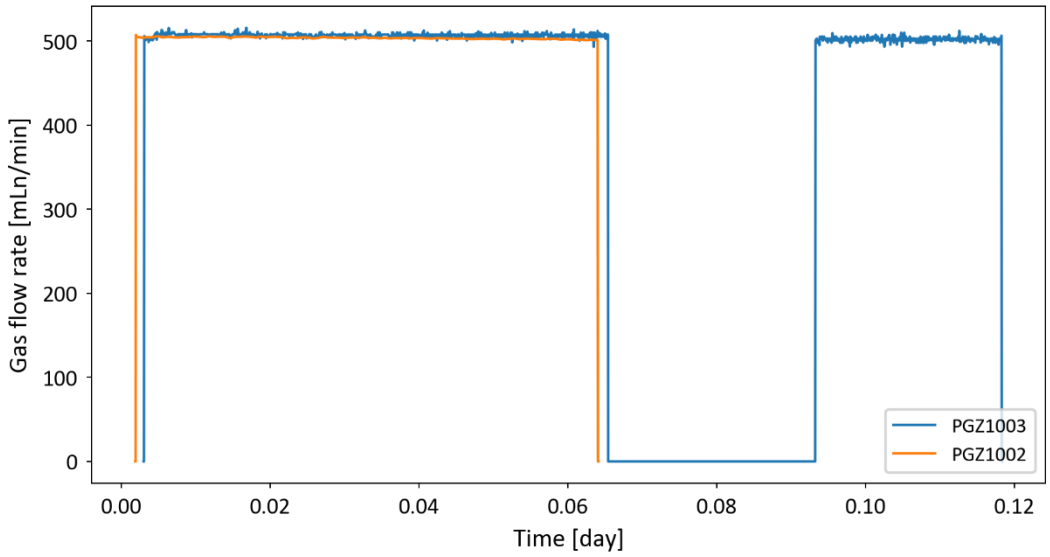

Figure 45. Gas flow rate injected in PGZ1002 and PGZ1003.

The BCs on the borehole wall for the preliminary stages are given in Figure 46 for PGZ1003. Stage S1 sets the stress state around the borehole and the modification of its hydraulic properties. In this task, the excavation-induced fracture network is referred to as BDZ, and the teams were free to model it explicitly or implicitly, being the latter obtained by their mechanical constitutive models coupled with the hydraulic representation.

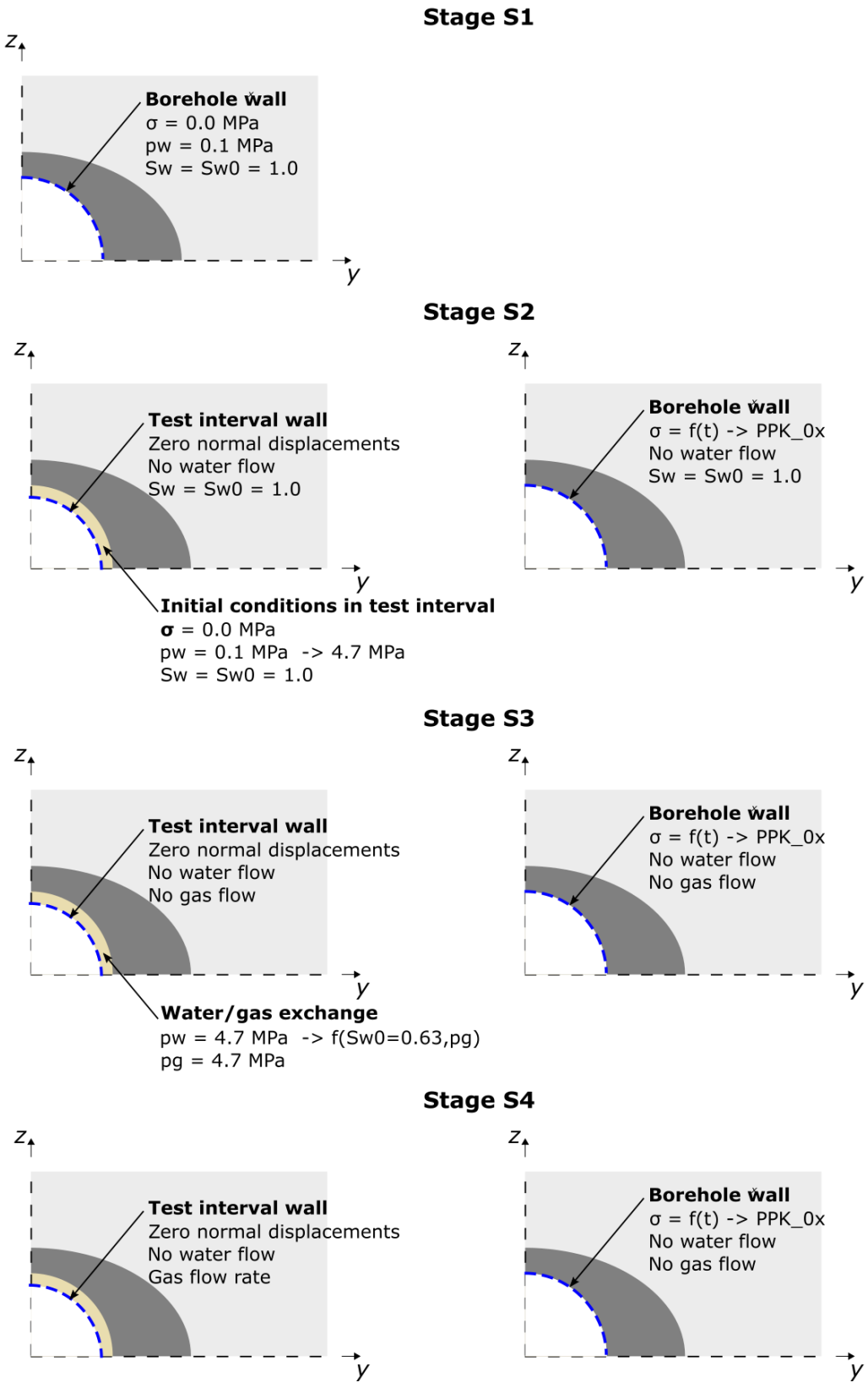

Figure 46. Boundary conditions for Stages S1 – S4 of PGZ1003.

5.2.2 Results and discussion

The model domains used for the modelling of PGZ1003 are presented in Figure 47. CIMNE-UPC and Lamcube reproduced one quarter of the model, whereas BGR/UFZ consider one eighth by assuming a symmetric plane at the mid-plane of the test interval. The research teams compared the difference between in the gas pressure response with elasticity and elastoplastic/damage models. An additional case consisted in including an explicit or ad-hoc BDZ as shown in Figure 47 for CIMNE-UPC and BGR/UFZ. As for the modelling of the CRQ experiment, Lamcube used the Weibull distribution to consider the effect of material heterogeneity. The material heterogeneity was only considered in the elements near the borehole, as shown for the spatial distribution of the Reuss equivalent bulk modulus in Figure 47.

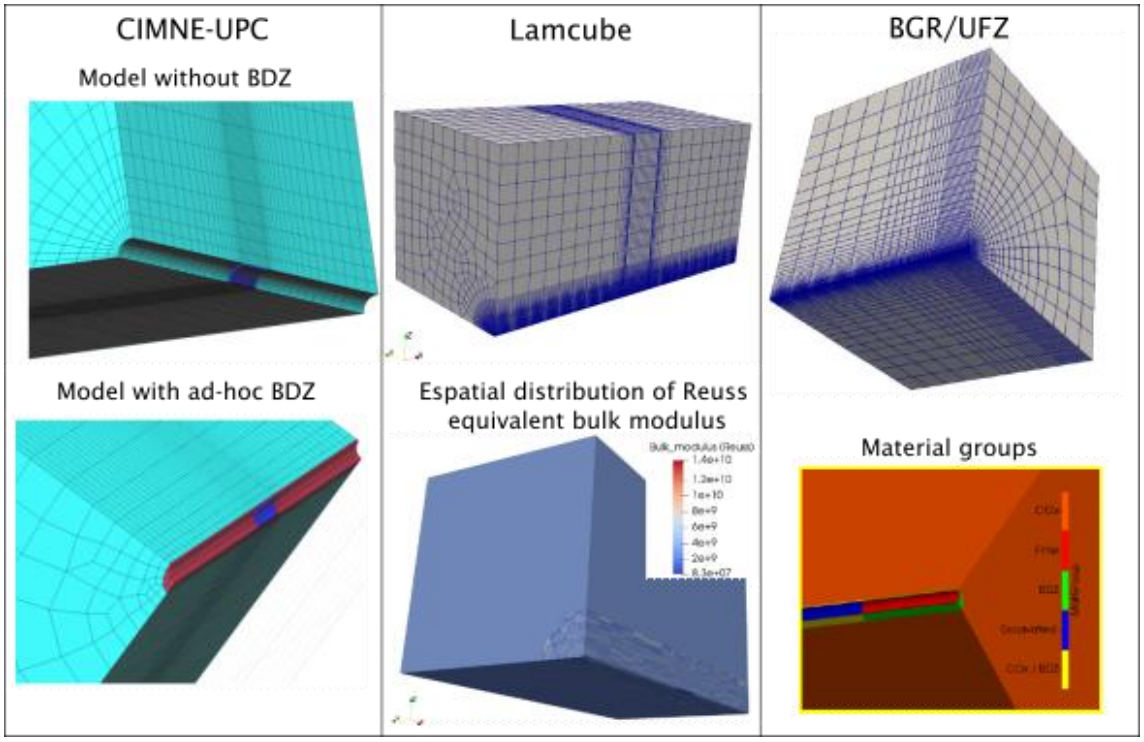

Figure 47. Geometries and meshes used for PGZ1003.

CIMNE-UPC showed that the gas pressure was highly overpredicted with an isotropic elastic model with and without considering the BDZ as defined in the specifications but by keeping equal permeabilities (Figure 48). Their model included the Kozeny equation, to link permeability to porosity, that was not able to reproduce the large permeability variations expected to be consistent with lower gas pressure variations. Their numerical results improved after calibrating the permeability in the BDZ by a factor of 10^3, increasing the porosity to 0.9 in the injection interval, and taking into

account anisotropy. These results were considered as their final results, despite the fact they carried out additional analyses.

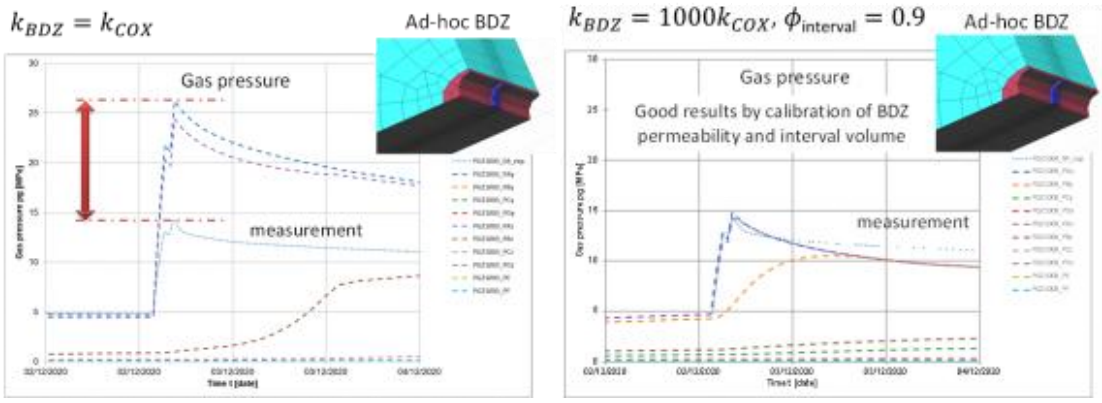

Figure 48. Gas pressure evolution for PGZ1003. (Left) Comparison between elasticity without and with BDZ with equal permeabilities. (Right) Elasticity with BDZ including higher permeability and porosity.

In the BGR/UFZ's model, the failure index permeability model was only applied in the excavation phase to consider changes in the permeability within the BDZ, while the strain dependent permeability (SDP) model was applied in the gas injection phase. The rest of parameters are those given for the sound rock. Figure 49 shows the sensitivity analysis of b_3, a parameter of the SDP expression given in eq. (41).

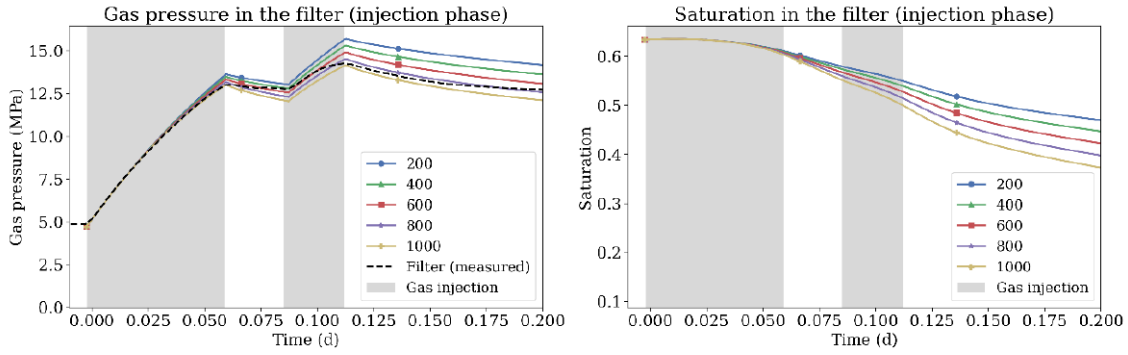

Figure 49. Gas pressure and saturation evolution in the filter for different strain-dependent permeability parameter values.

CIMNE-UPC and BGR/UFZ reported no preferential path with their elastoplastic models. Both teams concluded that the gas penetration into the sound rock was low. CIMNE-UPC tested the embedded permeability model used in Step A1.1 (Section 5.1) in a 3D geometry and in axisymmetric conditions to evaluate the possibility of flow in the direction parallel to the borehole and specifically towards the packers and neighbor intervals. Figure 50 shows the various contour plots obtained by these two teams. CIMNE-UPC showed that advection penetrates in the rock and gas tends to flow

towards the neighbor intervals, while BGR/UFZ showed that gas pressure developed in the long term mainly along the borehole axis through its BDZ.

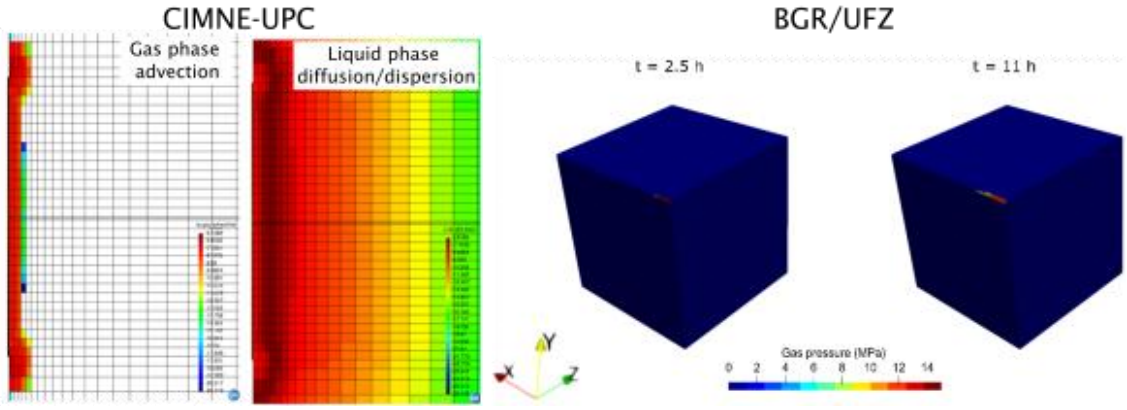

Figure 50. (Left) 5 Advective gas flux and diffusive gas flux during gas injection computed by CIMNE/UPC. (Right) Gas pressure distribution computed by BGR/UFZ.

Lamcube generated the BDZ during the borehole excavation. The damage inside the BDZ is characterized by shearing and larger extension in the horizontal direction. The numerical results showed a faster dissipation after injection compared to the experimental data. They attributed this discrepancy to the longitudinal gas flow towards the gallery. To improve the post-peak phase, Lamcube performed sensitivity analyses on two damage parameters (Figure 51): toughness parameter for shear damage, g_c^s, and β_d that controls the permeability evolution (see eq. (33)). The numerical results showed that small values of g_c^s yield more damage, leading to lower pressure build-up and faster dissipation. On the other hand, large values of β_d had similar effects on the results.

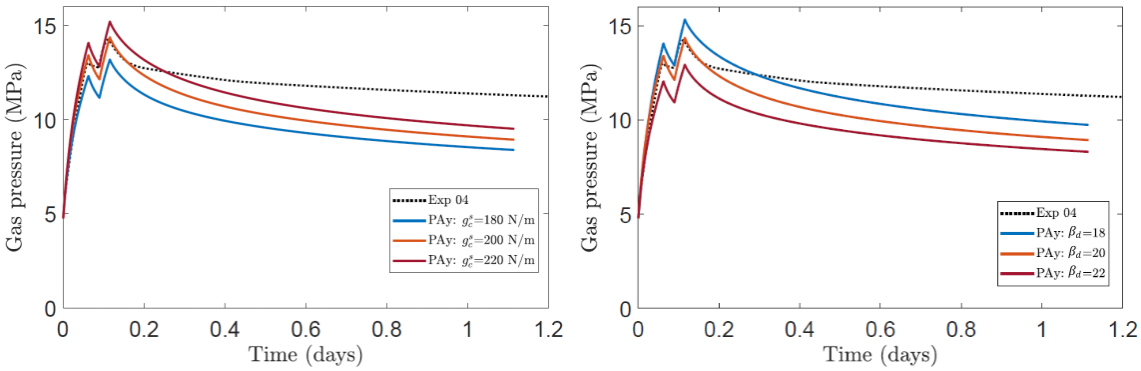

Figure 51. Evolution of gas pressure for two damage parameters.

Figure 52 shows the spatial distribution of damage after the gas injection. The shear damage created at the borehole excavation did not change. On the contrary, the gas injection induces mainly tensile damage, leading to larger displacement in the vertical direction. However, shear damage is larger than the tensile damage keeping the larger extension in the horizontal direction.

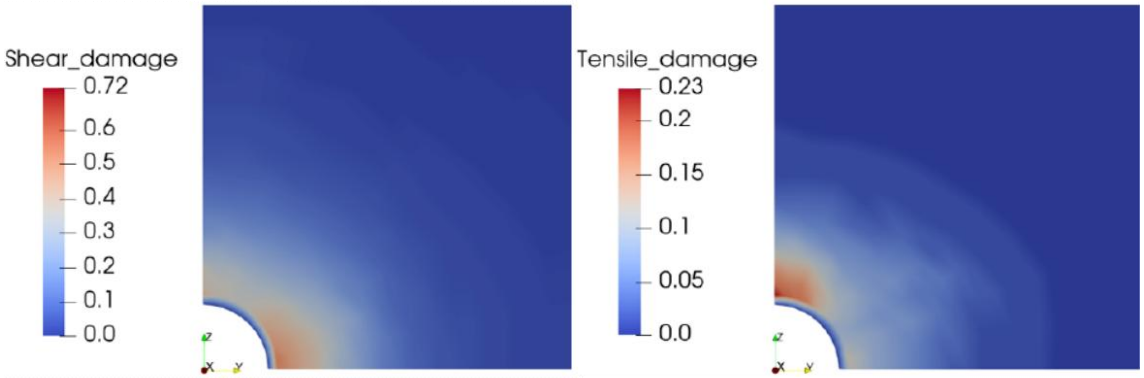

Figure 52. (Left) Distribution of tensile and (Right) shear damage after gas injection.

The final results of the interpretative modelling of PGZ1003 are presented in Figure 53. The results are presented for 3 study points in the horizontal direction: PAy = 0.033 m, PBy = 0.076 m, and PCy = 0.114 m. Gas pressure evolution curve at the injection interval (PAy) show a peak slightly higher than the measurements, while the dissipation phase is faster for the results of CIMNE-UPC and Lamcube. The gas pressure evolution whitin the BDZ (PBy) are different as a result of the different approaches used by the research teams to reproduce it. In BGR/UFZ's model, the gas takes longer to penetrate in the BDZ than while in UPC's models shows higher gas pressure in the sound rock (PCy) as a lower gas entry pressure is considered. A negligible pore pressure increase is observed for Lamcube and BGR/UFZ due to the fact that the gas entry pressure is assumed to be that of the sound rock.

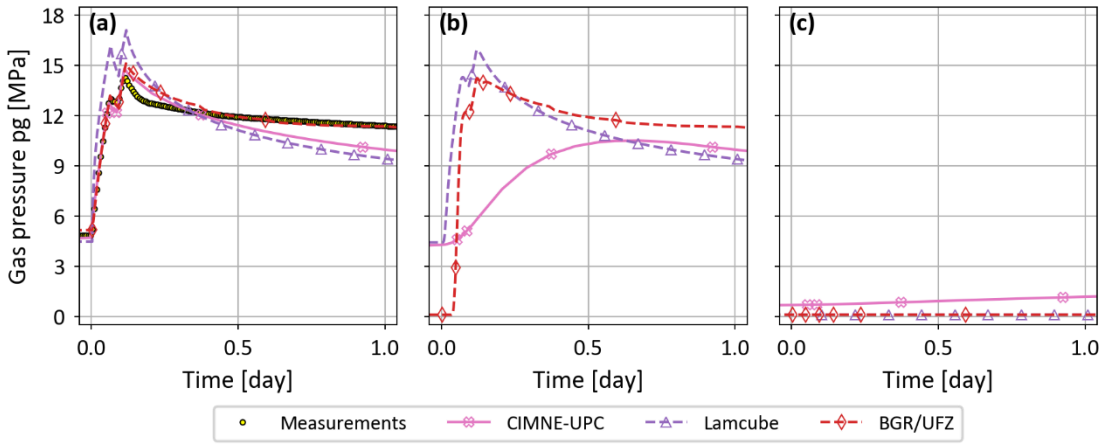

Figure 53. Gas pressure evolution for PGZ1003: (a) PAy, (b) PBy, and (c) PCy.

The research teams did not report any fracture development in the radial direction. One of the reasons is the fact that part of the gas percolated in the direction parallel to the borehole axis through the BDZ. The in-situ observations confirmed this point as one of the neighbouring intervals (PGZ1003_05) experienced an increase in pore pressure after the gas injection. It is not discarded that the gas percolated through a horizontal, longitudinal fracture was created from the injection interval towards PGZ1003_05. This potential gas preferential path formation was out of the scope of the objectives of the task and required to take into account in detail additional elements of the instrumentation and finer meshes.

The research teams applied their respective approaches to the blind prediction of PGZ1002, characterized by an anisotropic stress state on transversal section of the borehole. This anisotropic stress state leads to a lager extension in the vertical direction after the borehole excavation. Figure 54 shows the results in three study points located in the vertical direction: PAz = 0.033 m, PBz = 0.075 m, and PCz = 0.114 m. In all cases the numerical results overpredicted the gas pressure injected into the interval. The post injection phase resulted in faster dissipation for three numerical approaches. PBz was located within the explicit BDZ that allowed a gas pressure build-up in the case of CIMNE-UPC and BGR/UFZ, while the Lamcube's model reproduced a smaller extension of the BDZ that yielded a negligible gas pressure.

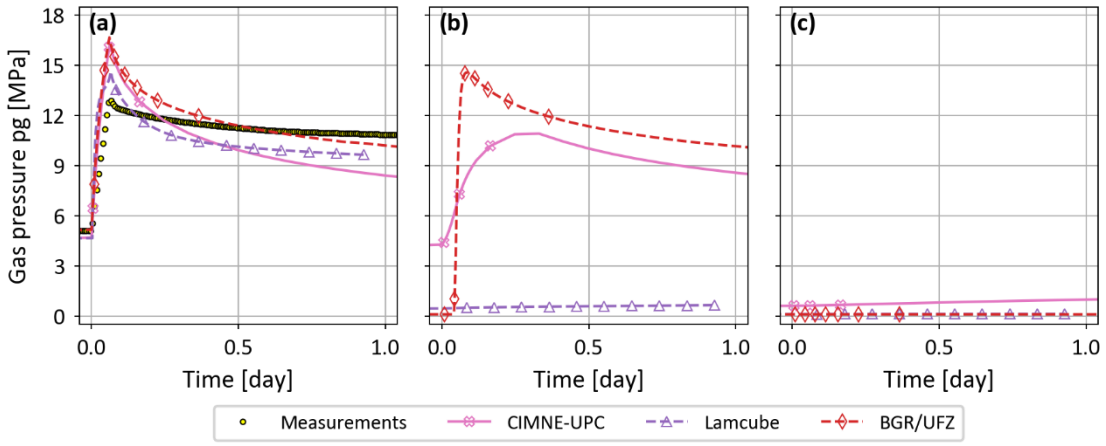

Figure 54. Gas pressure evolution for PGZ1002: (a) PAz, (b) PBz, and (c) PCz.

BGR/UFZ further improved their results at the peak pressure by calibrating the initial saturation in the interval as well as the parameter of their SDP model. However, the dissipation phase was faster than the measurements, indicating that additional calibration of the BDZ permeability was required.

The gas pressure field after the gas injection obtained by Lamcube and BGR/UFZ are presented in Figure 55. As for PGZ1003, a similar response was obtained except for the shape of the BDZ that was larger in the vertical direction. In both cases, the gas pressure was limited to the BDZ. Furthermore, BGR/UFZ reported that the gas percolates in the longitudinal direction as it was the case of PGZ1003.

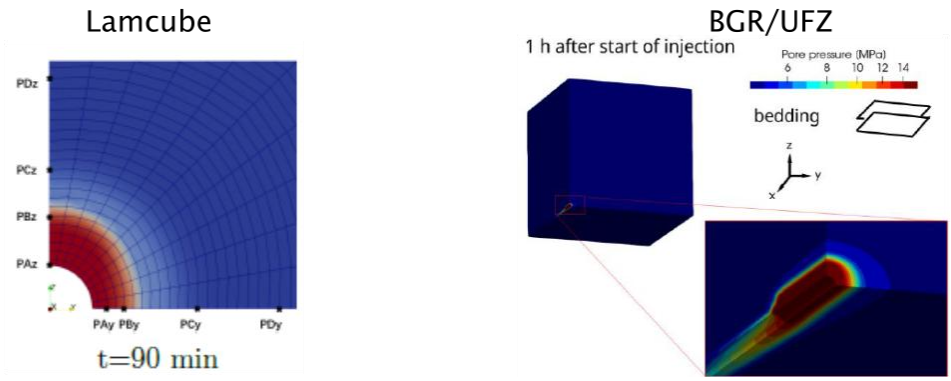

Figure 55. Gas pressure field after the gas injection in PGZ1002.

6 General conclusions

The fracturing process in the COx claystone is studied in Task A. Specifically, this task aimed to enhance the understanding of thermal and gas fracturing within the context of the high level and intermediate-level long-lived radioactive waste repository in France. Each process is addressed in a separate subtask: A1 for heat fracturing and A2 for gas fracturing.

The research teams participating in Subtask A1 defined the failure criteria for their respective thermo-hydro-mechanical models through thermal extension tests conducted on COx samples. Additionally, the teams carried out several sensitivity analyses due to the difficulties in calibrating measurements with a single set of model parameters. The modelling of the in-situ heater experiment produced satisfactory results in terms of temperature, allowing the teams to focus on modelling of the thermally induced pore pressure and conducting effective stress analyses. The research teams concluded that a higher pore pressure than the measured values was necessary to reach a tensile stress state or meet a failure criterion. These results support the idea that the packers did not fully isolate the measuring chamber once the pore pressure exceeded 15 MPa. While the measured value of the pore pressure breakdown was 17 MPa, numerical results reported values above 20 MPa. The stress analyses indicated that fracture occurrence strongly depends on the hydraulic BCs. Fully undrained conditions led to fracture development from the induced-excavation fracture network of the heater boreholes to the sound rock. Conversely, fully drained conditions allowed the fracture to be initiate in the sound rock. Depending on these assumptions, the research teams identified the origin of the fracture at different locations, although all reported zones around the central heater boreholes (CRQ1709). The pore pressure breakdown observed in the measurements was not captured by the research teams, which could be an area for future work in discrete medium approaches. Furthermore, there was a disagreement between the mode of fracture, which, according to the cores extracted in the heated zone, was only in shear mode. The application case involved the numerical reproduction of a HLW repository with a short distance between HLW disposal cells to facilitate fracture initiation. This constrained configuration allowed the fracture to be developed through diagonal bands from the HLW disposal cells towards the sound rock.

On the other hand, Subtask A2 began with the modelling of six benchmark exercises of gas injection tests to explore the influence of the COx property anisotropy and stress state anisotropy on fracture occurrence. Three exercises assumed a porous elastic

material, while the rest used a mechanical constitutive model incorporating a failure criterion or damage. These exercises took longer than expected, as each research team employed different formulations (e.g., diffusion process) or transitions from fully saturate to partially saturated conditions (e.g., residual degree of saturation). Despite these differences, results showed a certain level of agreement among teams. For these benchmark exercises, injection was extended until fracture creation and development, with fracture orientation strongly dependent on the stress conditions. However, the in-situ test had a shorter injection protocol, preventing fracture propagation. Numerical results yielded limited gas pressure within the BDZ with no fracture initiation, partially due to longitudinal gas percolation within the BDZ, also observed in the measurements. A challenge faced by the teams was dealing with a single study point per injection test, complicating the study of responses in the BDZ and sound rock near the injection interval. Different approaches resulted in different responses in these zones, contributing to the difficulty of well reproducing the dissipation process after the injection test, which relies on BDZ and the sound rock responses. Unlike Subtask A1, there was not an application case in Subtask A2. The decision was made to invest more time in several benchmark exercises, and then focus on the modelling of the in-situ experiments.

In both subtasks, the poro-elastic approach was tested, providing acceptable results under certain assumptions. However, the teams emphasized the need for advanced models to better understand specific processes observed in the field. Their approaches facilitated the study of processes in zones with no measurements, and in-situ observations were validated by the numerical results. Among the various features of the approaches, the coupling between the mechanical and hydraulic properties played a crucial role in the in-situ tests. The various approaches developed in Task A showed promising results as they were able to reproduce fracture development under certain conditions. However, additional data must be provided for a better representation of fracture propagation, which fell outside the scope of this work.

7 Planned and Completed Publications

Table 9 gives the planned and completed publications under this task.

Table 9. Planned and completed journal and conference papers for Task A.

Author(s)	Title	Journal/ Conference	Status
Mo, Y., Rodriguez-Dono, A., Olivella, S.	Hydro-Mechanical coupled analysis of gas injection in clay-based materials using different element types.	Geomech. Energy Environ.	Submitted
Mo, Y., Rodriguez-Dono, A., Olivella, S.	Exploring different FEM strategies for hydro-mechanical coupled gas injection simulation in clay materials.	Fluids	Submitted
Ouraga, Z., et al.	Thermo-hydro-mechanical coupling in a discrete medium with UDEC.	Geomech. Energy Environ.	In preparation
Plúa, C., et al.	TBD - Synthesis of heat fracturing in the COx (Task A1)	Geomech. Energy Environ.	In preparation
Plúa, C., et al.	TBD - Synthesis of heat fracturing in the COx (Task A2)	Geomech. Energy Environ.	In preparation
Radeisen, E., Shao, H., Pitz, M., Hesser, J., Kolditz, O., Wang, W.	Combination of a failure index and a dilatancy dependent permeability model in hydro-mechanically coupled numerical simulations of argillaceous rock formations of the Callovo-Oxfordian (COx)	Rock Mech. Rock Eng.	Submitted
Rodriguez-Dono, A., Zhou, Y., Olivella, S.	A new approach to model geomaterials with heterogeneous properties in thermo-hydro-mechanical coupled problems.	Computers and Geotechnics, 2023	Published
Rodriguez-Dono, A., Zhou, Y., Olivella, S., Gens, A.	Modelling a gas injection experiment incorporating embedded fractures and heterogeneous material properties.	Geomech. Energy Environ.	Submitted
Sasaki, T., Yoon, S., Rutqvist, J.	Modelling of failure and fracture development of the Callovo-Oxfordian claystone during an in-situ heating experiment associated with geological disposal of high-level radioactive waste.	Geomech. Energy Environ.	Submitted
Song, F. et al.	Numerical studies of THM behaviour of nuclear waste disposal at the repository scale.	Geomech. Energy Environ.	In preparation
Song, F. et al.	Analysis of thermally-induced fracture of Callovo-Oxfordian claystone: from lab test to field scale.	Geomech. Energy Environ.	In preparation

Author(s)	Title	Journal/ Conference	Status
Yu, Z., Shao, J., Sun, Y., Vu, M.-N., Plua, C., Armand, G.	Three-dimensional Modeling of Cracking with Thermo-hydromechanical Process by Considering Rock Heterogeneity	Rock Mech. Rock Eng., 2023	Published
Yu, Z., Shao, J., Sun, Y., Wang, M.-N., Vu, M., Plúa, C.	Numerical analysis of hydro-thermal fracturing in saturated rocks by considering material anisotropy and micro-structural heterogeneity	Int. J. Rock Mech. Min. Sci., 2023	Published
Yu, Z., Shao, J.-F., Yue, S., Vu, M.-N., Plúa, C., Armand, G.	Numerical modeling of gas injection induced cracking with unsaturated hydromechanical process in the context of radioactive waste disposal	Tunn. Undergr. Space Technol.	Accepted
Yu, Z. et al.	Numerical analysis of thermo-hydromechanical response considering induced damage and application to deep geological radioactive repository	Computers and Geotechnics	Submitted

8 Acknowledgements

DECOVALEX is an international research project comprising participants from industry, government and academia, focusing on development of understanding, models and codes in complex coupled problems in sub-surface geological and engineering applications; DECOVALEX-2023 is the current phase of the project. The authors appreciate and thank the DECOVALEX-2023 Funding Organisations Andra, BASE, BGE, BGR, CAS, CNSC, COVRA, US DOE, ENRESA, ENSI, JAEA, KAERI, NWMO, NWS, SÚRAO, SSM and Taipower for their financial and technical support of the work described in this paper. The statements made in the paper are, however, solely those of the authors and do not necessarily reflect those of the Funding Organisations.

9 References

Armand, G., Bumbieler, F., Conil, N., de La Vaissière, R., Bosgiraud, J.-M., Vu, M.-N., 2017. Main outcomes from in situ thermo-hydro-mechanical experiments programme to demonstrate feasibility of radioactive high-level waste disposal in the Callovo-Oxfordian claystone. J. Rock Mech. Geotech. Eng. 9, 415–427. https://doi.org/10.1016/j.jrmge.2017.03.004

Armand, G., Leveau, F., Nussbaum, C., de La Vaissiere, R., Noiret, A., Jaeggi, D., Landrein, P., Righini, C., 2014. Geometry and Properties of the Excavation-Induced Fractures at the Meuse/Haute-Marne URL Drifts. Rock Mech Rock Eng 47, 21–41. https://doi.org/10.1007/s00603-012-0339-6

Bishop, A., 1959. The Principle of Effective Stress. undefined.

Braun, P., Ghabezloo, S., Delage, P., Sulem, J., Conil, N., 2019. Determination of Multiple Thermo-Hydro-Mechanical Rock Properties in a Single Transient Experiment: Application to Shales. Rock Mech Rock Eng 52, 2023–2038. https://doi.org/10.1007/s00603-018-1692-x

Bumbieler, F., Plúa, C., Tourchi, S., Vu, M.-N., Vaunat, J., Gens, A., Armand, G., 2021. Feasibility of constructing a full-scale radioactive high-level waste disposal cell and characterization of its thermo-hydro-mechanical behavior. Int. J. Rock Mech. Min. Sci. 137, 104555. https://doi.org/10.1016/j.ijrmms.2020.104555

Burland, J.B., 1990. On the compressibility and shear strength of natural clays. Géotechnique 40, 329–378. https://doi.org/10.1680/geot.1990.40.3.329

Conil, N., Vitel, M., Plúa, C., Vu, M.N., Seyedi, D., Armand, G., 2020. In Situ Investigation of the THM Behavior of the Callovo-Oxfordian Claystone. Rock Mech Rock Eng 53, 2747–2769. https://doi.org/10.1007/s00603-020-02073-8

Cundall, P., 1971. A computer model for simulating progressive, large-scale movements in blocky rock systems. undefined.

de La Vaissière, R., Armand, G., Vu, M.N., Talandier, J., Cornet, F.H., 2020. Effect of gas flow rate on gas fracturing in Callovo-Oxfordian claystone. Presented at the 14th International Congress on Rock Mechanics and Rock Engineering (ISRM 2019), Rock Mechanics for Natural Resources and Infrastructure Development, Foz do Iguaçu, Brazil, pp. 939–946.

de La Vaissière, R., Gerard, P., Radu, J.-P., Charlier, R., Collin, F., Granet, S., Talandier, J., Piedevache, M., Helmlinger, B., 2014. Gas injection test in the Callovo-Oxfordian claystone: data analysis and numerical modelling. Geol. Soc. Spec. Publ. 400, 427–441. https://doi.org/10.1144/SP400.10

de La Vaissière, R., Talandier, J., Armand, G., Vu, M.-N., Cornet, F.H., 2019. From Two-Phase Flow to Gas Fracturing into Callovo-Oxfordian Claystone. Presented at the 53rd U.S. Rock Mechanics/Geomechanics Symposium, 23-26 June, American Rock Mechanics Association, New York City, New York.

Delay, J., Rebours, H., Vinsot, A., Robin, P., 2007. Scientific investigation in deep wells for nuclear waste disposal studies at the Meuse/Haute Marne underground research laboratory, Northeastern France. Physics and Chemistry of the Earth, Parts A/B/C, Clay in natural and engineered barriers for radioactive waste confinement - Part 1 32, 42–57. https://doi.org/10.1016/j.pce.2005.11.004

Dormieux, L., 2008. Une approche micromécanique de la notion de contrainte effective en mécanique des milieux poreux. Rev. Fr. Geotech. 55–66. https://doi.org/10.1051/geotech/2008122055

Francfort, G.A., Marigo, J.-J., 1998. Revisiting brittle fracture as an energy minimization problem. Journal of the Mechanics and Physics of Solids 46, 1319–1342. https://doi.org/10.1016/S0022-5096(98)00034-9

Garg, S.K., Nur, A., 1973. Effective stress laws for fluid-saturated porous rocks. J. Geophys. Res. 78, 5911–5921. https://doi.org/10.1029/JB078i026p05911

Gens, A., 2013. On the hydromechanical behaviour of argillaceous hard soils-weak rocks. Proceedings of the 15th European conference on soil mechanics and geotechnical engineering 71–118.

Gens, A., Carol, I., Alonso, E.E., 1990. A constitutive model for rock joints formulation and numerical implementation. Computers and Geotechnics, Special Issue on Soil-Structure Interaction 9, 3–20. https://doi.org/10.1016/0266-352X(90)90026-R

Ghabezloo, S., Sulem, J., 2010. Effect of the volume of the drainage system on the measurement of undrained thermo-poro-elastic parameters. Int. J. Rock Mech. Min. Sci. 47, 60–68. https://doi.org/10.1016/j.ijrmms.2009.03.001

Heusermann, S., Rolfs, O., Schmidt, U., 2003. Nonlinear finite-element analysis of solution mined storage caverns in rock salt using the LUBBY2 constitutive model. Computers and Structures 8–11, 629–638. https://doi.org/10.1016/S0045-7949(02)00415-7

Kolditz, O. (Ed.), 2012. Thermo-Hydro-Mechanical-Chemical Processes in Fractured Porous Media: Benchmarks and Examples, Lecture Notes in Computational Science and Engineering. Springer, Heidelberg.

Mánica, M.A., Gens, A., Vaunat, J., Armand, G., Vu, M.-N., 2021. Numerical simulation of underground excavations in an indurated clay using non-local regularisation. Part 1: formulation and base case. Géotechnique 1–21. https://doi.org/10.1680/jgeot.20.P.246

Mánica, M.A., Gens, A., Vaunat, J., Ruiz, D.F., 2018. Nonlocal plasticity modelling of strain localisation in stiff clays. Comput. Geotech. 103, 138–150. https://doi.org/10.1016/j.compgeo.2018.07.008

McCutcheon, S.C., Martin, J.L., Barnwell, T.O., 1993. Water Quality, in: Handbook of Hydrology. McGraw-Hill, New York, NY.

Miehe, C., Hofacker, M., Welschinger, F., 2010. A phase field model for rate-independent crack propagation: Robust algorithmic implementation based on

operator splits. Computer Methods in Applied Mechanics and Engineering 199, 2765–2778. https://doi.org/10.1016/j.cma.2010.04.011

Millard, A., Durin, M., Stietel, A., Thoraval, A., Vuillod, E., Baroudi, H., Plas, F., Bougnoux, A., Vouille, G., Kobayashi, A., Hara, K., Fujita, T., Ohnishi, Y., 1995. Discrete and continuum approaches to simulate the thermo-hydro-mechanical couplings in a large, fractured rock mass. International Journal of Rock Mechanics and Mining Sciences & Geomechanics Abstracts, Thermo-Hydro-Mechanical Coupling in Rock Mechanics 32, 409–434. https://doi.org/10.1016/0148-9062(95)00033-D

M'Jahad, S., Davy, C.A., Skoczylas, F., Talandier, J., 2017. Characterization of transport and water retention properties of damaged Callovo-Oxfordian claystone. The Geology Society of London, Special Publications 443, 159–177. https://doi.org/10.1144/SP443.23

Murakami, S., 2014. Continuum Damage Mechanics: A Continuum Mechanics Approach to the Analysis of Damage and Fracture. Springer, Dordrecht Heidelberg.

Olivella, S., Carrera, J., Gens, A., Alonso, E.E., 1994. Nonisothermal multiphase flow of brine and gas through saline media. Transp Porous Med 15, 271–293. https://doi.org/10.1007/BF00613282

Plúa, C., Vu, M.N., Armand, G., Rutqvist, J., Birkholzer, J., Xu, H., Guo, R., Thatcher, K.E., Bond, A.E., Wang, W., Nagel, T., Shao, H., Kolditz, O., 2021. A reliable numerical analysis for large-scale modelling of a high-level radioactive waste repository in the Callovo-Oxfordian claystone. Int. J. Rock Mech. Min. Sci. 140, 104574. https://doi.org/10.1016/j.ijrmms.2020.104574

Plúa, C., Vu, M.N., de La Vaissière, R., Armand, G., 2023. In Situ Thermal Hydrofracturing Behavior of the Callovo-Oxfordian Claystone within the Context of the Deep Geological Disposal of Radioactive Waste in France. Rock Mech Rock Eng. https://doi.org/10.1007/s00603-023-03618-3

Rinaldi, A.P., Rutqvist, J., Luu, K., Blanco-Martín, L., Hu, M., Sentís, M.L., Eberle, L., Kaestli, P., 2022. TOUGH3-FLAC3D: a modeling approach for parallel computing of fluid flow and geomechanics. Comput Geosci 26, 1563–1580. https://doi.org/10.1007/s10596-022-10176-0

Rowe, A.M., Chou, J.C.S., 1970. Pressure-volume-temperature-concentration relation of aqueous sodium chloride solutions. J. Chem. Eng. Data 15, 61–66. https://doi.org/10.1021/je60044a016

Rutqvist, J., 2011. Status of the TOUGH-FLAC simulator and recent applications related to coupled fluid flow and crustal deformations. Computers & Geosciences, 2009 Transport of Unsaturated Groundwater and Heat Symposium 37, 739–750. https://doi.org/10.1016/j.cageo.2010.08.006

Sainsbury, B.L., Sainsbury, D.P., 2017. Practical Use of the Ubiquitous-Joint Constitutive Model for the Simulation of Anisotropic Rock Masses. Rock Mech Rock Eng 50, 1507–1528. https://doi.org/10.1007/s00603-017-1177-3

Seyedi, D.M., Plúa, C., Vitel, M., Armand, G., Rutqvist, J., Birkholzer, J., Xu, H., Guo, R., Thatcher, K.E., Bond, A.E., Wang, W., Nagel, T., Shao, H., Kolditz, O., 2021. Upscaling THM modeling from small-scale to full-scale in-situ experiments in the Callovo-Oxfordian claystone. Int. J. Rock Mech. Min. Sci. 144, 104582. https://doi.org/10.1016/j.ijrmms.2020.104582

Sharqawy, M.H., Lienhard, J.H., Zubair, S.M., 2010. Thermophysical properties of seawater: a review of existing correlations and data. Desalination water treat 16, 354–380.

Thatcher, K.E., Bond, A.E., Norris, S., 2020. Pore pressure response to disposal of heat generating radioactive waste in a low permeability host rock. Int. J. Rock Mech. Min. Sci. 135, 104456. https://doi.org/10.1016/j.ijrmms.2020.104456

Wang, W., Shao, H., Rink, K., Fischer, T., Kolditz, O., Nagel, T., 2021. Analysis of coupled thermal-hydro-mechanical processes in Callovo-Oxfordian clay rock: From full-scale experiments to the repository scale. Engineering Geology 293, 106265. https://doi.org/10.1016/j.enggeo.2021.106265

Wileveau, Y., Cornet, F.H., Desroches, J., Blumling, P., 2007. Complete in situ stress determination in an argillite sedimentary formation. Physics and Chemistry of the Earth, Parts A/B/C 32, 866–878. https://doi.org/10.1016/j.pce.2006.03.018

Yu, Z., Shao, J.-F., Vu, M.-N., Armand, G., 2021. Numerical study of thermo-hydro-mechanical responses of in situ heating test with phase-field model. Int. J. Rock Mech. Min. Sci. 138, 104542. https://doi.org/10.1016/j.ijrmms.2020.104542

Zhang, C., Rothfuchs, T., 2004. Experimental study of the hydro-mechanical behaviour of the Callovo-Oxfordian argillite. Applied Clay Science, Clays in Natural and Engineered Barriers for Radioactive Waste Confinement 26, 325–336. https://doi.org/10.1016/j.clay.2003.12.025

Appendix A: Model parameters for Subtask A1

A.1 Water properties – Steps A1.1, A1.2 and A1.3

Lamcube

The linear thermal dilation coefficient of water is given by:

$$\alpha_{\mathrm{w}} = 10^{6}\,(-6\cdot 10^{-6}T^{4} + 1.66\cdot 10^{-3}T^{3} - 0.197796T^{2} + 16.862446\,T - 64.319951)/3$$

LBNL

The description of water properties is provided by the IAPWS-IF97.

BGR/UFZ

Step A1.1:

$$\alpha_{\mathrm{w}} = 1.0\cdot 10^{-4}\ 1/\mathrm{K}$$

$$\mu_{w} = 10^{-3}\ \mathrm{Pa}\cdot\mathrm{s}$$

The description of water properties is provided by the IAPWS-IF97 for Steps A1.2 and A1.3.

CIMNE-UPC

The water density variation employed within the Code Bright software is given by (McCutcheon et al., 1993) :

$$\rho_{\mathrm{w}} = \rho_{\mathrm{w0}}\exp[\beta_{\mathrm{w}}(p_{\mathrm{w}} - p_{\mathrm{w0}}) + A(T)]$$

$$A(T) = -(T + 288.9414)(T - 3.9863)^{2}/(508929.2\,(T + 68.12963))$$

The dynamic viscosity of water is expressed as follows:

$$\mu_{\mathrm{w}} = A\exp\left(\frac{B}{273.15 + T}\right)$$

with A = 2.1·10^{-12} and B = 1808.5.

Quintessa

The water density is given by (Rowe and Chou, 1970):

$$\rho_{\mathrm{w}} = \frac{1}{A(T) - PB(T) - P^{2}C(T)}$$

$$A(T) = 5.916365 - 0.01035794T + 9.270048 \times 10^{-6}T^2 - 1127.522T^{-1} + 100674.1T^{-2}$$

$$B(T) = (5.204914 \times 10^{-3} - 1.0482101 \times 10^{-5}T + 8.328532 \times 10^{-9}T^2 - 1.1702939T^{-1} + 102.2783T^{-2}) \times 1\left[\frac{cm^2}{kg}\right]$$

$$C(T) = (1.18547 \times 10^{-8} - 6.599143 \times 10^{-11}T) \times 1\left[\frac{cm^2}{kg}\right] \times 1\left[\frac{cm^2}{kg}\right]$$

$$P = p_{\mathrm{w}}/g$$

The dynamic viscosity of water is given by (Sharqawy et al., 2010):

$$\mu_w = 4.2844\mathrm{x}10^{-5} + (0.157(\mathrm{T}_c + 64.993)^2 - 91.296)^{-1}$$

A.2 COx parameters – Steps A1.1 and A1.2

Parameters	Unit	Notation	Value
Young's modulus normal to the bedding	10^9 Pa	E_{h}	6.0
Young's modulus parallel to the bedding	10^9 Pa	E_{v}	4.0
Poisson's ratio in the plane normal to the bedding	-	v_{hh}	0.3
Poisson's ratio in the plane parallel to the bedding	-	v_{vh}	0.3
Shear modulus in the plane normal to the bedding	10^9 Pa	G_{vh}	1.7
Density of solid grains	Kg/m^3	ρ_{s}	2770
Biot coefficient	-	b	0.8
Porosity	-	n	0.18
Intrinsic permeability normal to the bedding	10^{-20} m^2	K_{v}	1.33
Intrinsic permeability parallel to the bedding	10^{-20} m^2	K_{h}	4.0
Equivalent thermal conductivity normal to the bedding	W/m/K	λ_{v}	1.95
Equivalent thermal conductivity parallel to the bedding	W/m/K	λ_{h}	1.33
Heat capacity of solid particles	J/kg/K	C_{ps}	800
Volumetric thermal expansion of solid grains	10^{-5} 1/K	β_{s}	4.5

A.3 Geological layer parameters for the HLW repository – Step A1.3

Layer	E_v	v_{hv}	b	ϕ	K_v	ρ_s	λ_v	α_s	$C_{p,s}$
	10^9 Pa	-	-	-	10^{-20} m^2	10^3 kg/m^3	W/m/°C	10^{-5} $°C^{-1}$	10^2 J/kg/°C
BAR	3.60	0.3	0.8	0.13	10.0	2.67	1.10	2.20	8.48
KIM	3.60	0.3	0.8	0.13	10.0	2.67	1.10	2.20	8.48
OXF	30.00	0.3	0.8	0.13	10^4	2.69	2.30	0.45	7.45
USC	12.80	0.3	0.8	0.15	1.87	2.74	1.79	1.75	7.72
UT	8.50	0.3	0.8	0.173	1.87	2.75	1.47	1.75	7.35
UA23	4.00	0.3	0.8	0.18	1.33	2.77	1.28	1.50	8.00
UA1	12.5	0.3	0.8	0.164	1.87	2.75	1.63	1.75	7.50
DOG	30.00	0.3	0.8	0.10	100.0	2.63	2.30	0.45	7.88

A.4 Anisotropy ratio of geological layers for the HLW repository – Step A1.3

Layer	E_h/E_v	v_{hv}/v_{hH}	K_h/K_v	λ_h/λ_v
BAR	1.00	1.00	1.00	1.40
KIM	1.00	1.00	1.00	1.40
OXF	1.00	1.00	1.00	1.00
USC	1.50	1.50	3.00	1.00
UT	1.50	1.50	3.00	1.50
UA23	1.50	1.50	3.00	1.50
UA1	1.50	1.50	3.00	1.50

Layer	E_h/E_v	v_{hv}/v_{hH}	K_h/K_v	λ_h/λ_v
DOG	1.00	1.00	1.00	1.00

Appendix B: Benchmark model parameters for Subtask A2

B.1Water properties – Steps A2.1 and A2.2

Parameters	Unit	Notation	Value
Water compressibility	10^{-10} 1/Pa	C_{l}	4.5
Water density	10^{3} kg/m^3	ρ_l^{w}	1.0
Water dynamic viscosity	10^{-3} Pa·s	$\mu_{\mathrm{l}}^{\mathrm{w}}$	1.0
Water vapor dynamic viscosity	10^{-5} Pa·s	$\mu_{\mathrm{g}}^{\mathrm{w}}$	1.0
Water molar mass	kg/mol	M_{w}	0.018

B.2 Nitrogen properties – Steps A2.1 and A2.2

Parameters	Unit	Notation	Value
Nitrogen density	10^{3} kg/m^3	$\rho_{\mathrm{g}}^{\mathrm{N_2}}$	1.25
Nitrogen dynamic viscosity	10^{-3} Pa·s	$\mu_{\mathrm{g}}^{\mathrm{N_2}}$	1.79
Nitrogen molar mass	kg/mol	$M_{\mathrm{g}}^{\mathrm{N_2}}$	0.028

B.3 COx parameters – Step A2.1 (B1 to B4)

Parameters	Unit	Notation	COx	Interval
Young's modulus	10^{9} Pa	E_{iso}	5.24	0.001
Poisson ratio	-	v_{iso}	0.3	0.3
Density of solid grains	kg/m^3	ρ_{s}	2770	1631
Biot coefficient	-	b	0.8	1.0
Porosity	-	ϕ	0.18	0.3
Tortuosity	-	τ	0.25	1.0
Water permeability	10^{-20} m^2	$K_{\mathrm{w,iso}}^{\mathrm{sat}}$	2.77	10^{8}
Gas permeability	10^{-18} m^2	$K_{g,\mathrm{iso}}^{\mathrm{dry}}$	2.77	10^{6}

Parameters	Unit	Notation	COx	Interval
Van Genuchten gas entry pressure	10^6 Pa	p_r	15.0	0.05
Van Genuchten parameter	-	n	1.49	1.60
Residual degree of water saturation	-	S_{res}	0.01	0.01
Maximum degree of water saturation	-	$S_{\max}$	0.99	0.99

B.4 COx parameters – Step A2.1 (B5 and B6)

Parameters	Unit	Notation	COx	Interval
Young's modulus (parallel to bedding)	10^9 Pa	E_{h}	6.0	0.001
Young's modulus (perpendicular to bedding)	10^9 Pa	E_{v}	4.0	
Poisson ratio (Parallel to bedding)	-	v_{hh}	0.3	0.3
Poisson ratio (Perpendicular to bedding)	-	v_{vh}	0.3	
Shear modulus (Perpendicular to bedding)	10^9 Pa	G_{vh}	1.7	-
Uniaxial compression strength	10^6 Pa	σ_c	-21	-
Uniaxial tensile strength	10^6 Pa	σ_t	3	-
Density of solid grains	kg/m^3	ρ_{s}	2770	1631
Biot coefficient	-	b	0.8	1.0
Porosity	-	ϕ	0.18	0.3
Tortuosity	-	τ	0.25	1.0
Water permeability (parallel to bedding)	10^{-20} m^2	$K_{w,\mathrm{h}}^{\mathrm{sat}}$	4.0	10^8
Water permeability (perpendicular to bedding)	10^{-20} m^2	$K_{w,\mathrm{v}}^{\mathrm{sat}}$	1.33	10^8
Gas permeability (parallel to bedding)	10^{-18} m^2	$K_{g,\mathrm{h}}^{\mathrm{dry}}$	4.0	10^6
Gas permeability (perpendicular to bedding)	10^{-18} m^2	$K_{g,\mathrm{v}}^{\mathrm{dry}}$	1.33	10^6
Van Genuchten gas entry pressure	10^6 Pa	p_r	15.0	0.05
Van Genuchten parameter	-	n	1.49	1.60
Residual degree of saturation	-	S_{res}	0.01	0.01
Maximum degree of saturation	-	$S_{\max}$	0.99	0.99

B.5 COx parameters – Step A2.2

Parameters	Unit	Notation	COx	BDZ	Interval
Young's modulus (parallel to bedding)	10^9 Pa	E_{h}	6.0	6.0	0.1
Young's modulus (perpendicular to bedding)	10^9 Pa	E_{v}	4.0	4.0	
Poisson ratio (Parallel to bedding)	-	v_{hh}	0.3	0.3	0.3
Poisson ratio (Perpendicular to bedding)	-	v_{vh}	0.2	0.2	
Shear modulus (Perpendicular to bedding)	10^9 Pa	G_{vh}	1.7	1.7	-
Uniaxial compression strength	10^6 Pa	σ_c	21	21	-
Uniaxial tensile strength	10^6 Pa	σ_t	3	3	-
Density of solid grains	kg/m^3	ρ_{s}	2770	2770	1631
Biot coefficient	-	b	0.8	1.0	1.0
Porosity	-	ϕ	0.18	0.18	0.3
Tortuosity	-	τ	0.25	0.25	1.0
Water permeability (parallel to bedding)	10^{-20} m^2	$K_{w,\mathrm{h}}^{\mathrm{sat}}$	4.0	400	10^8
Water permeability (perpendicular to bedding)	10^{-20} m^2	$K_{w,\mathrm{v}}^{\mathrm{sat}}$	1.33	133	10^8
Gas permeability (parallel to bedding)	10^{-18} m^2	$K_{g,\mathrm{h}}^{\mathrm{dry}}$	4.0	400	10^6
Gas permeability (perpendicular to bedding)	10^{-18} m^2	$K_{g,\mathrm{v}}^{\mathrm{dry}}$	1.33	133	10^6
Van Genuchten gas entry pressure	10^6 Pa	p_r	15.0	4.5	0.05
Van Genuchten parameter	-	n	1.49	1.6	1.60
Residual degree of saturation	-	S_{res}	0.01	0.01	0.01
Maximum degree of saturation	-	S_{max}	1.00	1.00	1.00